

NUMERICAL SIMULATION OF BLOOD FLOW IN ARTERIAL STENOSIS UNDER
STEADY AND PULSATILE FLOW CONDITIONS

A Thesis by

Parth Pranavbhai Dave

Bachelor of Engineering, Gujarat University, 2007

Submitted to the Department of Aerospace Engineering
and the faculty of the Graduate School of
Wichita State University
in partial fulfillment of
the requirements for the degree of
Master of Science

May 2011

© Copyright 2011 by Parth Pranavbhai Dave

All Rights Reserved

NUMERICAL SIMULATION OF BLOOD FLOW IN ARTERIAL STENOSIS UNDER
STEADY AND PULSATILE FLOW CONDITIONS

The following faculty members have examined the final copy of this dissertation for form and content, and recommend that it be accepted in partial fulfillment of the requirement for the degree of Master of Science with a major in Aerospace Engineering.

Klaus A. Hoffmann, Committee Chair

Walter J. Horn, Committee Member

Hamid M. Lankarani, Committee Member

DEDICATION

To my parents, family members, teachers, and friends

ACKNOWLEDGEMENT

I would like to express my sincere gratitude to my advisor and professor, Dr. Klaus Hoffmann, for his many years of inspirational support, continuous guidance, encouragement, and patience throughout my graduate studies at Wichita State University and for helping me to overcome the obstacles in achieving my thesis.

I would like to thank the members of my thesis defense committee, Dr. Walter Horn and Dr. Hamid Lanakarani, for providing me with constructive suggestions and guidance.

I am grateful to Ms. Kristie Bixby for her careful reading of my thesis manuscript and for her constructive suggestions that enabled me to complete it. I greatly benefitted from her suggestions and advice. I would like to express my thanks to John Matrow, Director of the High Performance Computing Center (HiPecc) at Wichita State University, for his technical support.

I also thank my colleagues—Chiragkumar Tala, Ovais U. Khan, Sandeep Kumar Gadiparthi, Chinmay Shah and Srinivasa Velu—for their support. My sincere gratitude is extended to Asha Zaveri for her unconditional love and support.

Last but not least, I thank my family—my parents and grandparents—for their unconditional love and support in providing me with the best possible education throughout my life and for guiding me during the tumultuous times. I especially thank my mother, for without her, this achievement would not have been possible; therefore, I dedicate my thesis to her.

ABSTRACT

Cardiovascular diseases (CVDs) are among the leading causes of death in the world. In this study, an attempt was made to model the flow dynamics of blood in abnormally narrowed artery. Finite volume solver FLUENT was used for the analysis with the aim of understanding the consequences of increasing the degree of stenosis using a two-equation turbulence model. The compliant nature of the artery was neglected, and Newtonian behavior of the blood flow was assumed for the larger arteries. Steady-flow simulations with 75% area reductions were used to establish the validity of the current models by employing the standard and transitional variant of the $k-\omega$ turbulence models. Subsequently, it was found that transitional $k-\omega$ model was suitable for the low Reynolds number internal flows associated with the transition to turbulence, although only a minor departure in terms of the turbulence intensity peak was observed.

Unsteady blood flow was introduced by employing a sinusoidal pulsatile waveform at the inlet. The pulsatile nature of the blood flow was investigated in the range of the constriction ratio from 60% to 90%, with an inlet-specified pulse. It was hypothesized that the severity of the stenosis played a major role in the initiation of the turbulence, since no major turbulence was reported for the 60% and 75% area reductions, while increasing the constriction ratio of 90% significantly altered the flow dynamics and triggered the transition to turbulence much earlier than anticipated. The outcome of current numerical efforts was expressed in terms of wall shear stress, a hemodynamically relevant parameter.

TABLE OF CONTENTS

Chapter	Page
1. INTRODUCTION	1
1.1 Motivation and Challenges	1
1.2 Etiology of Blood Vessels	2
1.3 Atherosclerosis.....	4
1.4 Pathogenesis of Atherosclerosis	6
1.5 Hemodynamics of Arterial Stenosis	7
1.6 Wall Shear Stress Hypothesis	9
1.7 Objective of Current Numerical Efforts	10
2. LITERATURE REVIEW	12
2.1 Introduction.....	12
2.2 Experimental Investigations.....	13
2.3 Computational Investigations	16
3. MODEL GEOMETRY AND GRID GENERATION	23
3.1 Introduction.....	23
3.2 Geometry Description.....	23
3.3 Severity of Stenosis.....	24
3.3.1 Percentage Reduction in Cross-Sectional Area	25
3.3.2 Percentage Reduction in Diameter.....	25
3.4 Grid Generation Considerations	26
3.5 Grid Generation Approach.....	27
3.6 Parameters of Grid Quality Test	29
3.6.1 Equiangle Skew	29
3.6.2 Aspect Ratio.....	33
3.6.3 Size Change	35
4. NUMERICAL FORMULATION.....	36
4.1 Introduction.....	36
4.2 Governing Equations	36
4.3 Standard $k - \omega$ Turbulence Model.....	36
4.4 Assumptions.....	41
4.5 Boundary Conditions	41
4.5.1 Velocity Inlet	41
4.5.2 Outlet.....	42
4.5.3 Wall.....	42

TABLE OF CONTENTS (continued)

Chapter	Page
4.6	Turbulence Boundary Conditions43
4.6.1	Turbulence Intensity44
4.6.2	Length Scale.....44
4.7	Numerical Discretization45
5.	STEADY-STATE SIMULATIONS47
5.1	Introduction.....47
5.2	Non-Dimensionalization47
5.3	Assessment of Standard $k - \omega$ Turbulence Model.....48
5.3.1	Non-Dimensional Axial Velocity Profile of Standard $k - \omega$ Turbulence Model48
5.3.2	Turbulence Intensity of Standard $k - \omega$ Turbulence Model52
5.4	Assessment of Transitional $k - \omega$ Turbulence Model.....53
5.4.1	Non-Dimensional Axial Velocity Profile of Transitional $k - \omega$ Turbulence Model53
5.4.2	Turbulence Intensity of Transitional $k - \omega$ Turbulence Model58
5.5	Validation Studies59
5.5.1	Grid Independence59
5.5.2	Steady-State Simulation vs Transient-State Simulation63
5.5.3	Effect of Time-Step Size.....66
5.5.4	Effect of Flow Cycle on the Solution67
5.5.5	Influence of Inlet and Outlet Lengths69
5.6	Contour Plots70
6.	PULSATILE-FLOW SIMULATIONS73
6.1	Introduction.....73
6.2	Non-Dimensionalization75
6.3	Axial Velocity Profile75
6.4	Centerline Velocity Comparisons80
6.5	Wall Shear Stress Comparisons83
6.6	Axial Turbulence Intensity88
6.7	Convection of Turbulence.....92
7.	CONCLUSIONS95
7.1	Conclusions.....95
	REFERENCES97
	APPENDIX.....102

LIST OF TABLES

Table	Page
3.1. Reduction of Stenotic Vessels by Area and their Equivalent Reduction by Diameter against Non-Dimensional $\frac{h}{R}$ Ratio	26
3.2. Mesh Quality Based on Equiangle Skewness Criteria.....	30
3.3. Range of Equiangle Skewness for Grid G3	31
4.1. Model Constant for Transitional $k - \omega$ Model	40
5.1. Grid Configuration for Grid Independence Study	60
5.2. Recirculation Length for Grids G1, G2, and G3	62
5.3. Effect of Inlet and Outlet Lengths on Recirculation Length.....	70

LIST OF FIGURES

Figure	Page
1.1 Categorization of mortality due to CVDs	2
1.2 Etiology of blood vessels	3
1.3 Plaque buildup in a healthy artery	5
1.4 Hemodynamics of arterial stenosis	8
3.1 Schematic representation of stenotic vessel.....	24
3.2 Front view of unstructured grid for 75% area reduction.....	28
3.3 Front view of multi-block structured grid for 75% area reduction.....	28
3.4 Isometric view of grid for mesh quality test along the constant X	32
3.5 Grid quality test based on equiangle skew criteria (wireframe option enabled).....	32
3.6 Grid quality test based on equiangle skew criteria (wireframe option disabled).....	33
3.7 Four different views of worst element located in geometry	34
5.1 Non-dimensional velocity profile at axial location $\bar{X} = 0$	49
5.2 Non-dimensional velocity profile at axial location $\bar{X} = 1$	49
5.3 Non-dimensional velocity profile at axial location $\bar{X} = 2.5$	50
5.4 Non-dimensional velocity profile at axial location $\bar{X} = 4$	50
5.5 Non-dimensional velocity profile at axial location $\bar{X} = 5$	51
5.6 Non-dimensional velocity profile at axial location $\bar{X} = 6$	51
5.7 Variation of centerline axial velocity for standard $k - \omega$ turbulence model under inlet-specified turbulence intensity	52
5.8 Variation of turbulence intensity for standard $k - \omega$ turbulence model under inlet-specified turbulence intensity	53

LIST OF FIGURES (continued)

Figure	Page
5.9 Non-dimensional velocity profile at axial location $\bar{X} = 0$	55
5.10 Non-dimensional velocity profile at axial location $\bar{X} = 1$	55
5.11 Non-dimensional velocity profile at axial location $\bar{X} = 2.5$	56
5.12 Non-dimensional velocity profile at axial location $\bar{X} = 4$	56
5.13 Non-dimensional velocity profile at axial location $\bar{X} = 5$	57
5.14 Non-dimensional velocity profile at axial location $\bar{X} = 6$	57
5.15 Variation of centerline axial velocity for transitional $k - \omega$ turbulence model under inlet-specified turbulence intensity	58
5.16 Variation of the turbulence intensity for transitional $k - \omega$ turbulence model under inlet-specified turbulence intensity	59
5.17 Non-dimensional wall shear stress value for grids G1, G2, and G3.....	61
5.18 Zoom-in regions for grids G1, G2, and G3 for flow reattachment study	62
5.19 Wall $y+$ comparisons for grid G1, G2, and G3.....	63
5.20 Axial variation of centerline velocity for 75% area reduction at $Re = 1000$	65
5.21 Variation of turbulence intensity (I) along centerline velocity for 75% area reduction at $Re = 1000$	65
5.22 Comparison of wall shear stress using time-step sizes 0.01 and 0.001	66
5.23 Comparison of turbulence intensity along the centerline of the vessel at time step sizes 0.01 and 0.001	67
5.24 Distribution of wall shear stress corresponding to 20-second, 40-second, and 60-second time cycles	68
5.25 Maximum wall shear stress distributions near throat of stenosis corresponding to 20-second, 40-second, and 60-second time cycles	68

LIST OF FIGURES (continued)

Figure	Page
5.26 Axial velocity profiles at $\bar{X} = 0$	69
5.27 Axial velocity profiles at $\bar{X} = 2.5$	69
5.28 Contours of streamlines for transitional $k-\omega$ turbulence model with turbulence intensities of (a) 0.1% , (b) 1% , (c) 2% , (d) 3% , and (e) 5% at Re = 1000 for 75% area reduction.....	71
5.29 Contours of turbulence kinetic energy for transitional $k-\omega$ turbulence model with turbulence intensities of (a) 0.1% , (b) 1% , (c) 2% , (d) 3% , and (e) 5% at Re = 1000 for 75% area reduction	72
6.1 Inlet pulsatile waveform plotted against non-dimensional time $\frac{t}{T}$	74
6.2 Non-dimensional velocity profiles at axial location $\bar{X} = -1$	76
6.3 Non-dimensional velocity profiles at axial location $\bar{X} = 0$	77
6.4 Non-dimensional velocity profiles at axial location $\bar{X} = 1$	77
6.5 Non-dimensional velocity profiles at axial location $\bar{X} = 2$	78
6.6 Non-dimensional velocity profiles at axial location $\bar{X} = 4$	78
6.7 Non-dimensional velocity profiles at axial location $\bar{X} = 6$	79
6.8 Variations of axial centerline velocity for 60%, 75%, and 90% area reductions corresponding to $\frac{t}{T} = 0$	81
6.9 Variations of axial centerline velocity for 60%, 75%, and 90% area reductions corresponding to $\frac{t}{T} = 0.25$	81
6.10 Variations of axial centerline velocity for 60%, 75% and 90% area reductions corresponding to $\frac{t}{T} = 0.50$	82
6.11 Variations of axial centerline velocity for 60%, 75%, and 90% area reductions corresponding to $\frac{t}{T} = 0.75$	82

LIST OF FIGURES (continued)

Figure	Page
6.12 Comparisons of wall shear stress at non-dimensional time $\frac{t}{T} = 0.0$	84
6.13 Comparisons of wall shear stress at non-dimensional time $\frac{t}{T} = 0.25$	84
6.14 Comparisons of wall shear stress at non-dimensional time $\frac{t}{T} = 0.50$	85
6.15 Comparisons of wall shear stress at non-dimensional time $\frac{t}{T} = 0.75$	85
6.16 Variation of wall shear stress during different time levels for 75% area reduction	87
6.17 Variation of wall shear stress over non-dimensional time $\frac{t}{T}$ near throat of stenosis for 90% area reduction.....	88
6.18 Comparisons of variation of turbulence intensity along centerline of vessel for 60%, 75%, and 90% area reductions corresponding to non-dimensional time $\frac{t}{T} = 0$	89
6.19 Comparisons of variation of turbulence intensity along centerline of vessel for 60%, 75%, and 90% area reductions corresponding to non-dimensional time $\frac{t}{T} = 0.25$	89
6.20 Comparisons of variation of turbulence intensity along centerline of vessel for 60%, 75%, and 90% area reductions corresponding to non-dimensional time $\frac{t}{T} = 0.50$	90
6.21 Comparisons of variation of of turbulence intensity along centerline of vessel for 60%, 75%, and 90% area reductions corresponding to non-dimensional time $\frac{t}{T} = 0.75$	90
6.22 Convection of turbulence along axial location during peak systole	93
6.23 Convection of turbulence along axial location during mid-deceleration.....	93
6.24 Convection of turbulence along axial location during end-deceleration	94

LIST OF ABBREVIATIONS

3-D	Three-Dimensional
AR	Aspect Ratio
CFD	Computational Fluid Dynamics
CHD	Coronary Heart Disease
CVD	Cardiovascular Disease
D	Diameter of Unoccluded Vessel
DNS	Direct Numerical Simulation
EAS	Equiangle Skew
h	Maximum Height of Stenosis
$\frac{h}{R}$	Non-Dimensional Ratio
L	Length of Vessel
LES	Large Eddy Simulation
PISO	Pressure Implicit Splitting of Operator
R	Radius
RANS	Reynolds Average Navier Stokes Equation
Re	Reynolds Number
SC	Size Change
SIMPLEC	Semi-Implicit Method for Pressure-Linked Equations-Consistent
SKW	Standard $k - \omega$ Model
TI	Turbulence Intensity
TKW	Transitional $k - \omega$ Model
WSS	Wall Shear Stress

LIST OF ABBREVIATIONS (continued)

Subscripts:

avg	Average
eq	Equilateral
H	Hydraulic
<i>i</i>	Inlet
m	Mean
max	Maximum
<i>o</i>	Outlet
r	Radial
<i>r</i>	Recirculation

LIST OF SYMBOLS

U_θ	Circumferential Component of Velocity
f	Frequency
D_H	Hydraulic Diameter
t	Local Time
\bar{X}	Non-Dimensional Axial Location
$\frac{t}{T}$	Non-Dimensional Time
L_o	Outlet Length
L_r	Recirculation Length
T	Time Period
I	Turbulence Intensity
l	Turbulent Length Scale
x_0	Width of Stenosis
$R(x)$	Gaussian Profile
L_i	Inlet Length
U_r	Radial Component of Velocity
dA	Differential Area
dD	Differential Diameter
N	Number of Time Steps
y^+	Non-Dimensional Wall Distance

LIST OF SYMBOLS (continued)

Greek Symbols:

α	Womersley Parameter
μ	Absolute or Laminar Viscosity
π	Pi Constant
θ	Angle in Degrees
ρ	Density
ω	Angular Frequency
Δt	Time-Step Size
μ_t	Turbulent Viscosity

CHAPTER 1

INTRODUCTION

1.1 Motivation and Challenges

Cardiovascular diseases (CVDs), the largest cause of mortality in modern society, are actually group of diseases associated with the abnormal functioning of the blood vessels. Statistics from world-renowned health-monitoring agencies, such as the World Health Organization, have revealed that in the year 2004, nearly 29% of mortality was attributed to one or other form of cardiovascular diseases, i.e., 17.1 million people died due to CVDs [1]. Low- and middle-income countries were more vulnerable to CVDs, as 82% of global mortality was reported in these countries in the year 2004 [1]. The burden of CVDs continues to increase in terms of mortality, and nearly 23.6 million people are expected to die from these diseases by the year 2030, according to predicted World Health Organization statistics [1]. The majority of deaths from these diseases would occur as the result of heart attack, coronary heart disease (CHD), or stroke, which is a cerebrovascular disease [1]. CHD, myocardial infarction, and stroke have a higher mortality rate than any other type of cardiovascular disease. According to American Heart Association statistics on heart disease and stroke for the year 2006, nearly 81,100,000 Americans have one or other form of CVDs; among those, 831,272 Americans died from CVDs, which constitutes 34.3% of all deaths, making it the leading cause of mortality in the United States [2]. The rate of mortality from coronary heart disease is 425,425 K for myocardial infarction 141.5 K while for stroke 137.1 K and heart failure 282.8 K [2]. Figure 1.1 shows the percentage breakdown of cardiovascular disease, which clearly indicates that nearly two-thirds of mortality from CVDs was attributed to CHD and stroke together in the year 2006 [2].

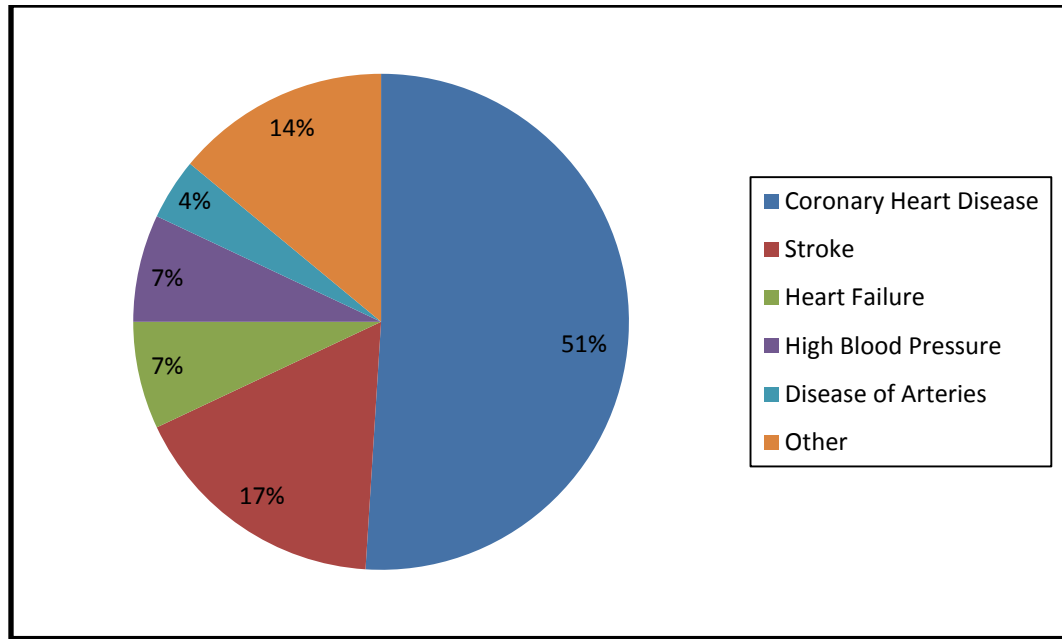


Figure 1.1. Categorization of mortality due to CVDs [2].

1.2 Etiology of Blood Vessels

Blood vessels are broadly classified into three categories: arteries, veins, and capillaries. The function of arteries is to carry oxygenated blood from the heart to different organs of the human body, while the function of veins is to carry deoxygenated blood back to the heart. Capillaries are micro-blood vessels that connect the arteries and veins together to complete a closed loop for circulation.

Tunica Intima: The tunica intima is the layer of smooth endothelium cells located in the innermost layer of an artery. It is mainly composed of endothelium cells, which are one-layer-thick cells that provide the smooth lining. These cells are in direct contact with the blood so they play an important role in blood flow, blood clotting, and leukocyte adhesion [3].

Tunica Externa: The tunica externa, also referred to as the tunica adventitia, is the outermost layer of an artery. It is made up of connective tissues and is composed of much stiffer

collageneous fibers. As a result, it can prevent tearing of the blood vessel wall during body movement [3].

Tunica Media: The middle layer between the tunica intima and tunica externa is known as the tunica media, which is mainly composed of smooth muscle cells and elastic fibers. The tunica media plays an important role in vasoconstriction and vasodilatation. Vasoconstriction is a mechanism by which the diameter of artery is reduced as the result of muscular contraction, while vasodilatation is a mechanism by which the diameter of an artery increases due to relaxation of the smooth muscle cells [3]. Elastic fibers give the tunica media flexibility to expand during the pumping of the blood supply during the systole phase of contraction, and it regains its regular size due to its elastic recoil ability when the pumping action diminishes.

Capillaries are the smallest blood vessels. They consist of only one layer of tunica intima, and tunica media; tunica externa are absent from capillaries. Figure 1.2 shows the etiology of blood vessels.

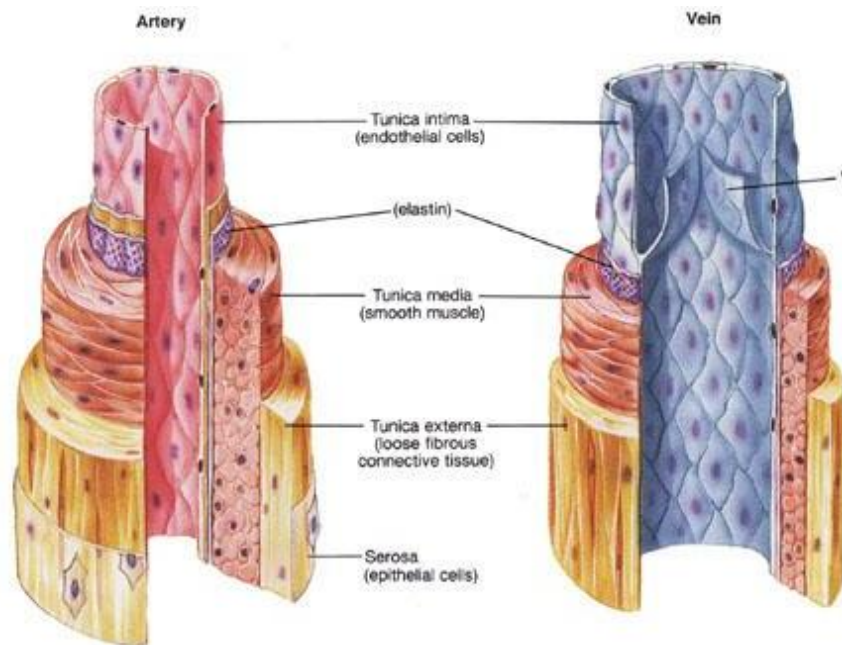


Figure 1.2. Etiology of blood vessels [4].

1.3 Atherosclerosis

The function of arteries is to supply oxygen-rich blood and nutrients to various organs of the human body in order for them to function properly. The condition of atherosclerosis, which is the disease of medium- or large-size arteries [5], develops when fatty substances, cholesterol, calcium, cellular waste products, and other substances accumulate inside the arterial wall [5, 6]. Risk factors that aggravate the process of accumulation are diabetes mellitus, a high-fat diet, high blood cholesterol, high alcohol consumption, smoking, and obesity [5]. This accumulation of substances is referred to as atherosclerosis plaque and impedes the incoming blood supply [5, 6], as shown in Figure 1.3. Furthermore, arteries lose their compliant nature because of the accumulation of calcified products, and therefore, atherosclerosis is also referred to as “hardening of the arteries” [5]. In some cases, increasing age also contributes to hardening of the arteries [5]. The growth of this accumulation continues once it is initiated and eventually restricts the blood supply to the effected vessels; therefore, cardiovascular diseases are classified according to the target vessel affected as the result of atherosclerotic plaque deposition [6].

The function of the coronary artery is to supply oxygenated blood and nutrition to the heart muscles [7]. The underlying cause of any coronary heart disease or any cardiovascular disease in general is atherosclerosis. Clinical implications of this disease vastly depend upon the amount of blockage within the coronary artery. Symptoms of the disease are normally chest pain (also known as angina), shortness of breath, and, in some cases, heart attack, where the oxygenated blood supply to the coronary artery is completely blocked and the entire coronary artery is occluded as a result of plaque formation [8]. Consequently, the heart is deprived of enough blood to function properly.

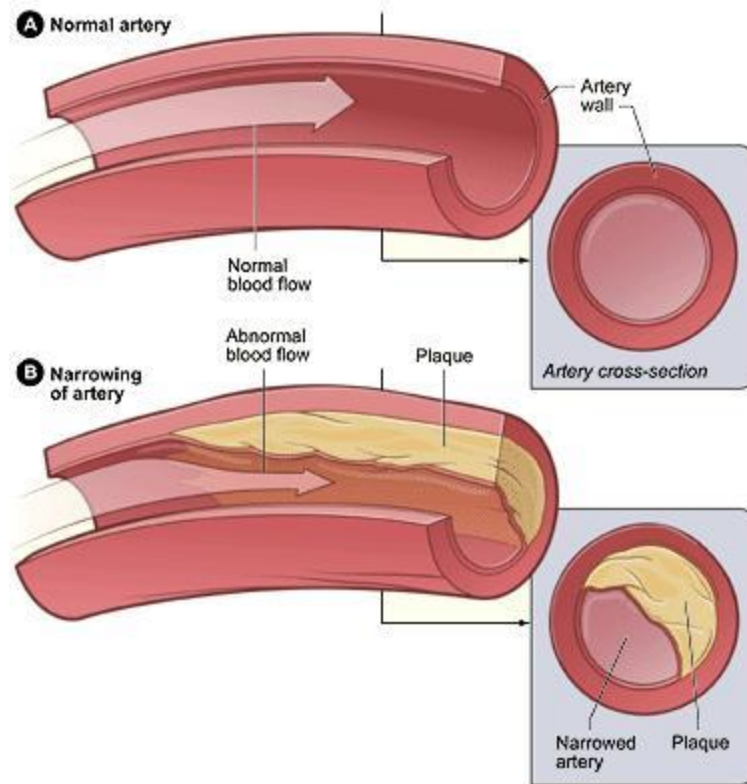


Figure 1.3. Plaque buildup in a healthy artery [6].

The carotid artery is a blood vessel that provides oxygenated blood supply to the brain [6]. When cholesterol, fatty acids, and other cellular waste products accumulate inside the carotid artery and form plaque, this is referred to as carotid artery disease or carotid artery stenosis [6]. The brain needs an uninterrupted blood supply to ensure that it is able to control the proper functioning of various organs that involve thinking, walking, speech, memory, etc. [8, 9]. If the blood supply to the brain is interrupted or blocked due to a blood clot, atherosclerotic plaque, or damage caused to an artery, then the nerve cells are deprived of the essential blood supply needed to sustain proper functioning of the brain [8, 9]. If the condition is severe or persists for a long period of time, then brain cells begin to die [8, 9]. This condition is referred to as stroke. The implications of a stroke depend on the part of the brain affected as the result of the damage,

since the brain controls the functioning of several other areas [9]. Stroke is also referred to as cerebrovascular disease or apoplexy [9].

A condition for peripheral arterial disease develops when narrowing of the blood vessels occurs due to plaque buildup in a normal artery [9]. As a result, the oxygenated blood supply from the heart to the lower extremities is obstructed because of the partially or completely occluded blood vessel. This is also called peripheral vascular disease (PVD). Its clinical implications include gangrene and amputation of the limbs due to the reduced blood supply to the lower extremities such as arms, legs, stomach, and kidneys [9].

1.4 Pathogenesis of Atherosclerosis

Damage to the endothelium cells triggers the development of a lesion, and over time, due to the biological response of cells to injury and growth factors, a condition develops where the lesion reaches an advanced stage and occludes the lumen cross-sectional area significantly and in some severe cases completely. It is implied that the accumulation of lipoproteins in the artery, i.e., oxidized LDL (ox LDL), in addition to the risk factor of an elevated level of low-density lipoproteins from hypercholesterolemia, hypertension, smoking, and diabetes [10] can trigger the development of atherosclerosis. Junctions and branching points are more prone to endothelium cell injury [10]. Once the ox LDL accumulates in the arterial wall, it enhances the permeability of that wall [10, 11]. Meanwhile glycoprotein, which has a specific adherence property, accumulates near the arterial wall, and as a result, monocytes and T lymphocytes also adhere near the arterial wall; together, along with further accumulation of LDL, they infiltrate inside the tunica media [11]. During this time, monocytes are converted into macrophages and, with subsequent accumulation and migration of lipids in smooth muscle cells, convert the macrophages into a foam cell; together with leukocytes, this becomes a fatty streak. The

thickness of the fibrous core continues to increase with the further increase in leukocytes and, together with the proliferation and migration of the lipids inside the smooth muscle layer, becomes known as atherosclerotic plaque. During the early stage of atherosclerotic plaque development, the artery tries to maintain a normal lumen cross-sectional area due to its elastic nature. However, with further thinning of the fibrous core, a condition whereby the fibrous core protrudes into the lumen is reached, and thus stenosis is formed. If a rupture is caused on the plaque surface, it eventually forms a thrombosis, or blood clot. Arteries that are more prone to atherosclerosis are coronary arteries, the common carotid artery, and renal arteries [12].

1.5 Hemodynamics of Arterial Stenosis

Stenosis develops in the artery as a result of the accumulation of cholesterol and other fatty materials. This eventually lessens the lumen cross-sectional area and impedes the incoming upstream flow of blood. Moderate to severe clinical consequences can occur downstream of the stenosis, depending upon the severity of the obstruction and the upstream flow conditions. Stenosis alters the hemodynamics or blood movement. Consider an artery with a 50% reduction in its area, as shown in Figure 1.4. The cross-sectional area of the artery where the diameter of the lumen is minimum is referred to as the throat; upstream of the throat is a converging section (1) of the artery and downstream of the throat is a diverging section (3) of the artery.

The diameter of the artery significantly decreases in the converging section of the artery. Therefore, the local velocity here increases to satisfy the continuity equation for an incompressible flow. Applying the principle of conservation of mass at sections 1 and 2 yields

$$A_1V_1 = A_2V_2 \quad (1.1)$$

The increase in velocity is accompanied by the elevated magnitude of the wall shear stress near the throat. In addition, pressure at the throat of the stenosis decreases substantially in order to

accommodate the increased kinetic energy, thus satisfying the energy conservation principal. Therefore, Bernoulli's principal can be applied at sections 1 and 2:

$$P_1 + \frac{1}{2}(\rho V_1^2) = P_2 + \frac{1}{2}(\rho V_2^2) \quad (1.2)$$

$$P_1 - P_2 = \frac{1}{2} \rho (V_2^2 - V_1^2) \quad (1.3)$$

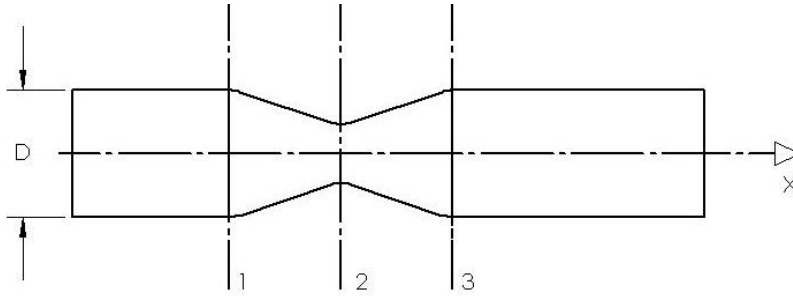


Figure 1.4. Hemodynamics of arterial stenosis.

Equation (1.3) shows the severe consequences of the stenosis. The velocity at the throat of the stenosis increases a few magnitudes, depending upon the severity of the stenosis; therefore, there will be a large pressure drop in order to satisfy Bernoulli's principle. Sometimes in extremely severe cases, local blood pressure drastically falls below the external pressure, resulting in the collapsing of the artery [12]. The collapsing mechanism depends upon the mechanical properties of the arterial wall, severity of reduction of the lumen cross-sectional area, and upstream flow conditions [12]. The collapsing phenomenon appears to be most favorable during the systolic phase of a flow cycle, since the accelerating flow prevails during this phase. Therefore, there will be a huge pressure drop during this phase since relative magnitudes of the velocity are higher compared to the diastolic phase of the flow cycle. Clinical implications are structural damage to the wall, which in turn may cause worsening of the disease, plaque cap rupture, and thrombosis [12].

In order to satisfy the principle of conservation of mass, the area in the diverging part of the artery increases, and therefore, velocity decreases. A decrease in the kinetic energy of the flow is accounted for by the increase in potential energy, which in turn increases pressure in the axial direction, thus causing an adverse pressure gradient, which is responsible for flow separation. The increasing severity of stenosis causes the flow to be separated from the vessel wall, and turbulence may exist downstream of the stenosis, depending upon the degree of occlusion and upstream flow condition. As a result, pressure never fully recovers downstream of the stenosis [12].

From a clinical standpoint, the ramifications of a moderate-to-severe stenosis include the following: reduction of blood to the distal parts of the circulation system; elevated levels of wall shear stress, which has the potential to damage the endothelium cell layer; and if the plaque is broken, then embolization, i.e., migration to the distal site of the circulation system. In all cases, the target vessels may be deprived of getting a sufficient oxygen supply, and even tissue death may occur [12].

1.6 Wall Shear Stress Hypothesis

Wall shear stress is an important fluid dynamics variable in the mapping of atherosclerosis. Two contradicting mechanisms have been found to be responsible for the atherosclerosis: high wall shear stress suggested by Fry [13] and the shear-dependent mass transport mechanism suggested by Caro et al. [14]. In the high wall shear stress theory, it is postulated that elevated values of this stress can cause potential damage to the endothelium cell layer and thus, is responsible for the atherosclerosis [13]. The shear-dependent mass transport hypothesis is based on lipid accumulation in the arterial wall and the mass transport process of biological necessary substances [14]. In a healthy artery, it is necessary to maintain proper

diffusion of biologically necessary substances between the arterial wall and blood, and vice versa [14]. Caro et al. proposed that the shear rate near the arterial wall is the one that influences this process greatly [14]. Diffusional boundary-layer thickness is greater for slow-moving fluid than for fast-moving fluid [14]. Thus, diffusional flux is greater for the higher-velocity fluid compared to the slower-moving fluid; in fact, the faster-moving fluid enhances the mass transfer rate. Therefore, lipid accumulation in the faster-moving fluid is washed away with it, but not so for the slower-moving fluid. On the contrary, mass transport of the biologically necessary substances between the arterial wall and blood is disturbed for the lower-velocity fluid, and therefore, a higher concentration of the lipid accumulation is found to exist near the arterial wall in the low wall shear stress region; thus it is vulnerable to atherosclerosis as a result of increased residence particle time of the lipid accumulation. Furthermore, the effect of atherosclerosis is promoted in the area of low wall shear stress or high oscillatory wall shear stress due to the atherogenic blood particles reported in both areas, and therefore, these areas are more vulnerable to atherosclerosis over time.

1.7 Objective of Current Numerical Efforts

The human circulation system is composed of a large network of arteries, veins, and capillaries; their proper functioning ensures a healthier life. However, once blood is propelled out of the left ventricle, it encounters numerous sites where the local hemodynamics is altered due to the geometric complexity such as bifurcation, curvature, junction, or plaque buildup in a healthy artery [12]. For example, when blood is propelled out of the left ventricle, it immediately encounters the aortic arch, a curved vessel [12]. Another important site from a hemodynamic perspective is the common carotid artery, since it bifurcates into two separate arteries known as the internal carotid artery and external carotid artery [12]. Of interest is one of the features of the

internal carotid artery, a bulge or enlarged portion of the artery, commonly referred to as the “sinus bulge.” The sinus bulge is always present in a healthy artery, which plays an important role in local hemodynamics. Enlargement of the internal carotid artery in the local cross-sectional area is attributed to the sinus bulge and is responsible for the local flow separation. Thus, the artery is constantly exposed to the low value of wall shear stress and therefore, inclined to promote atherosclerosis. In addition, hemodynamics in the vicinity of the stenosed cardiac valve, arterial stenosis, and aneurysm also gained the attention of the investigators due to its moderate-to-severe implications on the local hemodynamics and propagation of the disease. The current numerical work is strictly limited to the hemodynamics of arterial stenosis and the clinical implications in the distal part of the stenosis. The literature review has indicated that the two-equation turbulence models are better able to predict the turbulence at the physiologically relevant low Reynolds (Re) number, and hence different variations of the two turbulence models have been compared against available experimental data.

This thesis is divided into two parts: one is the steady-state flow analysis, which is carried out to validate the current study, and is discussed in Chapter 5; the other involves the modeling of the pulsatile nature of blood flow and the effects of increasing the constriction ratio from 60% to 90%, which is discussed at length in Chapter 6.

CHAPTER 2

LITERATURE REVIEW

2.1 Introduction

Researchers have extensively studied flow in the vicinity of the stenosis because of its interesting features, such as jet formation, flow separation, pressure and velocity fluctuations, wall shear stress, flow disturbances, and the clinical implications from a fluid dynamics point of view. These studies can be classified into two categories: experimental work and computational studies. Much of the experimental studies were carried out in the 70s and 80s by various researchers, notably among them, Cassanova and Giddens [15], Deshpande and Giddens [16], Ahmed and Giddens [17, 18], Khalifa and Giddens [19], Liber and Giddens [21], and Ojha et al. [22], who carried out extensive flow visualizations using the laser Doppler anemometry and photochromic tracer method, which formed the basis for several subsequent studies. With the increase in computational power and advancement of computational algorithms, it became possible to replicate the experimental results using Reynolds-averaged Navier-Stokes (RANS)-based turbulence models and test them against the experimental values. Numerical formulation of the RANS-based turbulence model is inherited from the averaging of the Navier-Stokes equation and fails to predict the correct amount of turbulent statistics. The further increase in computational power allowed efforts in addressing the issue of inefficiency of the conventional two-equation turbulence model to predict the turbulent pulsatile arterial flow by using the higher-order turbulence models such as large eddy simulation (LES) and direct numerical simulation (DNS).

2.2 Experimental Investigations

Giddens and his co-workers [15, 16, 17, 18, 19, 21] have performed extensive flow visualization in the vicinity of stenosis under steady-state and pulsatile-flow conditions. Deshpande and Giddens [16] carried out a study on a stenotic artery with a range of Reynolds numbers up to 15000. However, these results seem to be unrealistic from the flow condition that prevails in the circulatory system, considering the Reynolds numbers in the human circulation system ranges from 1 to 4000 [23], based upon the diameter of the artery. However, their findings are useful [16].

Ahmed and Giddens [17] worked extensively on flow visualization in the vicinity of the stenosis and its effect on the post-stenotic flow field under steady and pulsatile flow conditions. Using axisymmetric model geometries with 25%, 50%, and 75% area reductions, flow visualizations were carried out for the same geometries with the help of laser Doppler anemometry in the range of Reynolds numbers from 500 to 2000, which represents flow in the larger arteries of the human circulatory system, such as the aorta. They found that flow is in the process of transition to turbulence for 75% area reduction. In addition, an increase in the recirculation region was found by increasing the Reynolds number from 500 to 1000; however, a further increase in the Reynolds number up to 2000 decreased the recirculation length significantly, due to fully turbulent flow conditions at Reynolds number 2000.

Ahmed and Giddens [18] carried out an extension of their work by considering the pulsatile flow condition in the circulatory system in the range of Reynolds numbers from 200 to 1000, with the mean Reynolds number value of 600 and an unsteady Womersley parameter of 7.5. For example, during the maximum flow rate corresponding to a Reynolds number of 1000 for 50% area reduction, the flow condition exhibits the same behavior as was found under the

steady-flow conditions, i.e., jet emerging from the throat followed by a thick flow separation region downstream of the stenosis with discrete frequency fluctuations. However, during the minimum flow rate along the centerline, corresponding to a Reynolds number of 200, rather blunt velocity profiles were observed. In addition to this, turbulence was not observed during the entire pulse cycle for 50% area reduction. However, increasing the constriction to 75%, the scenario changed, and turbulent conditions were seen to prevail during the deceleration phase of the pulse cycle downstream of the stenosis.

It is hypothesized [20] that the flow can experience three different types of states during the course of laminar-to-turbulent transition, depending upon the local conditions of the flow: laminar, disturbed viscous, and turbulent. The turbulent state can even be further classified into two categories: permanent and transient. If turbulence diminishes with time or space, it is referred to as transient turbulence; otherwise, it is permanent turbulence. For example, in a wall-bounded viscous flow at a low Reynolds number, the effect of turbulence may decay downstream of the flow due to the dampening effect provided by the wall.

Correlating this observation to Ahmed and Giddens [17] experimental results for a 75% area reduction at a Reynolds number of 1000, it was observed that the flow remains completely laminar upstream of the stenosis. However, due to the introduction of the stenosis in the geometry, which ultimately brings instability to the flow as a result of area reduction, and followed by the adverse pressure gradient, the flow experiences discrete oscillations until $\bar{Z} \leq 4$. Beyond that, the $\bar{Z} \geq 4$ flow undergoes a transient turbulent state as it achieves a laminar state further downstream.

Similar experimental studies were carried out by Yongchareon and Young [20] who carried out experimental work on three different geometries, i.e., smooth contoured stenosis,

plug-like obstruction, and sharp-edge orifice. Of these, the streamline contoured stenosis is more relevant to the current work. They observed that increasing the severity of the stenosis decreases the critical Reynolds number associated with the laminar-to-turbulent transition. Furthermore, they noticed in their experimental work that the magnitude of the disturbance intensity is much higher near the wall than at the core of the vessel for the low Reynolds number flow under investigation. This reflects the fact that instabilities first arise in the shear layer and then propagate to the core of the vessel as the Reynolds number increases. In addition, disturbance first arises downstream of the stenosis and proceeds further upstream when increasing the Reynolds number. Similar findings were reported by Ahmed and Giddens [17] in their experimental work and are consistent with other experimental work and observations.

Liber and Giddens [21] conducted experimental studies for 75% and 90% area stenosis reductions and used the same flow conditions except for a slight variation in the unsteady Womersley parameter of 5.3, compared to 7.5 that was utilized by Ahmed and Giddens [18] using laser velocimetry. They sought the correlations between the core flow and the near-wall flow behavior by comparing the ensemble average centerline velocity and non-dimensional wall shear stress at the different axial locations. They demonstrated that the vortices with discrete frequency exist 2 to 3 diameters downstream of the stenosis; eventually the vortices convected further downstream and broke into random fluctuations. However, at 6 diameters distal to the stenosis for a 90% area reduction, a large drop in the ensemble average velocity was observed during the acceleration phase, and eventually the jet disappeared from the core region. This location is identified as the site of “puff formation,” a fact validated by the large oscillation in the wall shear stress value at the same location. In addition, turbulence was observed during the acceleration and deceleration phases of the flow cycle distal to the stenosis, while for a 75% area

reduction, a discrete velocity fluctuation was observed rather than turbulence flow condition, contradicting Ahmed and Giddens's experimental work as a result of different flow conditions used by Liber and Giddens [21].

2.3 Computational Investigations

Normal blood flow in the human circulatory system is in the range of Reynolds numbers from 1 to 4000 [23]. A mild-to-severe constriction causes transition to the turbulence much earlier than the prescribed range for this transition. Most publications focus on this behavior in the modeling of blood flow using different variants of the two-equation turbulence modeling and verify the efficacy of each turbulence model against the experimentally measured data.

Ghalichi et al. [24] carried out numerical simulations on 50%, 75%, and 86% area reductions under steady flow conditions using the commercial finite element software FIDAP under a physiologically relevant Reynolds number. They found that the Wilcox low Reynolds number $k-\omega$ model is the most suitable for low Reynolds flows dealing with turbulence or transition to turbulence, compared to the $k-\varepsilon$ model. In addition, the low Reynolds number $k-\omega$ model is also capable of dealing with laminar flow studies.

Verghese et al. [25, 26] used a direct numerical simulation study to replicate the benchmark experimental results of Ahmed and Giddens for 75% axi-symmetric stenosis in the range of Reynolds numbers of 500 to 1000, and they extended their work for asymmetric stenosis with the same degree of stenosis under steady and pulsatile flow conditions. However, their results for axisymmetric simulations failed to predict the flow reattachment at the experimentally measured value of $5 \leq \bar{Z} \leq 6$ for 75% area reduction at the $Re = 1000$ under the steady flow condition, since they noticed that flow does not reattach at the outlet, i.e., $\bar{Z} = 16$, in contrast to the experimental measured value of $\bar{Z} = 6$. It was found in the current work that

turbulence intensity plays a major role in reattachment of flow. The current work predicts the same result as was reported by Verghese et al. [25, 26] since flow fails to reattach until $\bar{X} = 14$, contradicting the experimental results. However, better agreement was established with experimental results by changing the turbulence intensity from 0.1% to 2%, since the numerical results replicate the experimentally measured values. Therefore, it is believed that Verghese et al. ignored the effect of turbulence intensity. This phenomenon is discussed at length in Chapter 5. Furthermore, in their pulsatile flow simulations, Verghese et al. used a flat inlet velocity profile rather than the fully developed flow.

Recently, more relevant to the current work, Ryval et al. [27] utilized the commercial finite volume solver FLUENT 6.0 to mimic the experimental work of Ahmed and Giddens under steady [17] and pulsatile [18] flow conditions. They carried out the simulation on different versions of the $k-\omega$ turbulence model and found that the transitional $k-\omega$ model performed relatively better than the standard $k-\omega$ turbulence model for the steady and pulsatile flows. However, excellent agreement was found between Ahmed and Giddens [17, 18] experimental work and their simulation results, since they used a Womersley solution as an inlet boundary condition for the pulsatile flow conditions in terms of axial velocity profiles at different axial locations. Eventually they found that the standard $k-\omega$ model over-predicts the amount of turbulence under pulsatile flow conditions, while the transitional variant of the $k-\omega$ model under-predicts the amount of turbulence under the investigating conditions. Their results are consistent with the current work.

Long et al. [28] used a physiological waveform representation of flow conditions that exists in the common carotid artery using Doppler ultrasound with a mean Reynolds number of 300 and unsteady Womersley parameter of 5.31. They specified an inlet boundary condition for

different degrees of stenosis severity for axisymmetric and asymmetric models. However, the profile used to describe the constriction was slightly different than others such as Liber and Giddens [21] have used. Computational results demonstrate that two different flow-separation regions were found during the period of pulse in the axisymmetric model. The main flow separation region, as a result of area reduction just downstream of the stenosis during the flow acceleration phase, eventually breaks into two flow-separation regions during the flow-deceleration phase. Of these, the main flow-separation region was found to exist during the entire pulse cycle, while the effects of the secondary flow-separation region ceased after a certain period of time, depending upon the complexity of the stenosis.

Long et al. [28] computed the result for the asymmetrical geometrical configurations under similar flow conditions, which they used for axisymmetric stenosis. However, it is clearly evident from their results that eccentricity in the form of the stenosis brings an additional flow separation region compared to its axisymmetric counterpart. Of these, the main flow-separation region exists just downstream of the stenosis in the direction of the eccentricity, followed by a secondary flow-separation region, opposite to the direction of the eccentricity. However, this is the flow-deceleration phase when the primary flow separation zone breaks into two separate flow-separation regions in the direction of the stenosis and forms an additional flow-separation region compared to its axisymmetric counterpart. In addition, they noticed that the effect of axisymmetric stenosis tends to last longer than the asymmetrical counterpart, due to symmetry.

Recently, more relevant to the current work, Dietiker and Hoffmann [29] performed a computational simulation in a tapered artery with varying degrees of stenosis and made useful comparisons between Newtonian and non-Newtonian flow behaviors. However, their study largely focused on wall shear stress, since the higher value of wall shear stress causes harm to the

endothelium layer. They found that a 50% in diameter reduction (75% area reduction) causes damage to the endothelium layer during peak systole.

Banks and Bressloff [30] tested the efficacy of both the RNG $k - \varepsilon$ turbulence model and the transitional $k - \omega$ turbulence model. They observed two noticeable differences. For the RNG $k - \varepsilon$ model, the flow reattaches approximately one diameter downstream of the stenosis, while the $k - \omega$ model is in good agreement with the experimental results downstream of the stenosis. However, even further downstream of the obstruction, the $k - \omega$ model too fails to predict the correct result. Therefore, neither turbulence model was in good agreement with the experimental data. However, one can consider that the transitional variant of the $k - \omega$ turbulence model predicts much of the flow phenomena correctly and is deemed more suitable for the low Reynolds number internal flows dealing with the transition to turbulence. In addition, the $k - \varepsilon$ model was insensitive to inlet turbulence intensity, since no differences were observed by increasing the turbulence intensity from 0% to 10%, which is physically incorrect. The $k - \omega$ model showed a variation in the flow field with increasing turbulence intensity, i.e., for turbulence intensity, 0% flow behaves as laminar flow, while significant differences are observed in transported quantities with increasing turbulence intensity, a fact briefly discussed in Chapter 5 in the current work.

Liao et al. [31] carried out a comparative study of stenotic vessels under physiological flow, simple pulsatile flow, and equivalent pulsatile flow conditions, and they compared each of them during the various phases of the flow cycle, i.e., initial zero, peak forward flow, middle zero, and peak backward flow. They made two distinct observations about the development of the flow during various flow phases. They reported that flow deceleration is responsible for vortex translation and formation. For example, the size of the recirculating vortex that is distal to

the stenosis increased during the transition from the peak forward state to the middle zero flow phase, i.e., deceleration stage of the flow. Furthermore, a large recirculation region was found to exist for all three cases under investigation during the initial zero phase, although the net inflow rate at that instance was zero. This reflects the fact that the instantaneous flow field is strongly influenced by the previous flow conditions, i.e., peak backward flow cycle preceding the initial zero in their simulations. However, they reported the elevated values of the time-averaged wall vorticity for the simple and equivalent pulsatile flow cases as against the physiological flow conditions, due to the fact that net peak backward flow rate for the simple and equivalent pulsatile flow was 75% greater than the actual physiological flow. The same behavior was found to be true for the axial centerline disturbance intensity.

Non-Newtonian behavior of the blood flow was modeled by Gijsen et al. [32] and compared against the Newtonian flow result under the steady flow condition in the large carotid artery bifurcation model. The shear-thinning property of the blood was considered by employing the Carreau-Yasuda model, while the viscoelastic nature of the blood was ignored in their work. However, significant differences were observed in their comparison of non-Newtonian vs. Newtonian behavior, since the axial velocity was flattened in the common carotid artery relative to the Newtonian case. Furthermore, they observed that Newtonian flow undergoes a flow separation along the divider wall in the internal carotid artery, a region that was found to be absent in the non-Newtonian counterpart.

Scotti and Piomelli [33] conducted their work on a two-dimensional (2-D) channel flow subjected to a pressure-driven oscillating boundary condition. The simplicity of their geometry allowed them to carry out the DNS and LES on the same geometry and compare their results against three different RANS turbulence models, i.e., Spalart-Allamaras, $k-\varepsilon$, and $k-\varepsilon-\nu^2$.

They found that turbulence models based on the RANS formulation predicted the flow statistics, i.e., velocity profiles in agreement with the LES, DNS, and experimental data. However, poor agreement for the RANS turbulence model was established when the turbulent flow statistics were compared against their DNS and LES data. In addition, they observed that turbulence has a sufficient time to decay at low frequency, while the production of turbulence and dissipation is out of phase at high frequency.

Mittal et al. [34] carried out an LES study on the planer channel with one-sided semi-circular constrictions under pulsatile flow conditions in the range of Reynolds numbers 750 to 2000, with focus on the spectral analysis of the turbulent flows. Existence of the Kelvin-Helmoltz types of vortices were found in the shear layer for Reynolds numbers greater than 1000. Furthermore, the magnitude of the turbulence kinetic energy and specific dissipation increases in the vicinity of the stenosis with increasing Reynolds numbers. However, far downstream, regardless of the Reynolds number, a more uniform structure in terms of turbulence statistics was observed.

Mallinger and Drikakis [35] investigated three-dimensional instabilities for the stenotic vessel. Instability was introduced by means of the White perturbation method to break the symmetry along the centerline velocity with 20% amplitude. The structure of instability was classified into two distinct regions: one just downstream of the stenosis, where coherence of the jet is preserved, while the other far downstream of the stenosis, where coherence of the jet is broken. This region is the potential site for the laminar-to-turbulent transition.

Stability analysis of the three-dimensional steady and pulsatile stenotic flows were carried out by Sherwin and Blackburn [36] using linear stability analysis and direct numerical simulation. They used the Floquet stability analysis for their study and found that steady flow

undergoes a Conda-type wall reattachment. Maximum energy for the linear instability modes was found to exist downstream of the stenosis for the pulsatile flows, and breakdown of the tilting ring vortex appears to travel further upstream before it confines itself within the few diameters of the stenosis.

To conclude, these recent studies by Verghese et al. [25, 26], Scotti and Piomelli [33], Mittal et al. [34], and Sherwin and Blackburn [36] emphasized the need for the DNS and LES studies of turbulent pulsatile arterial flow beyond the RANS turbulence model, since more promising results were found with the help of the LES and DNS, especially in terms of turbulence parameters, which they reported. However, this can be achieved only through enormous computational cost for these complex three-dimensional (3-D) geometries.

CHAPTER 3

MODEL GEOMETRY AND GRID GENERATION

3.1 Introduction

To understand the physics of stenotic flows, several assumptions have been made, beginning from the pre-processing to post-processing part of the analysis. This chapter deals with the pre-processing segment of the analysis, such as the selection of model stenosis geometry and grid generation techniques employed in the modeling, including structured and unstructured grid generation methods and its advantages and drawbacks for the geometry under investigation. It also deals with the different parameters required to examine whether the grid is of high quality or poor quality to carry out the computational fluid dynamics (CFD) simulations.

3.2 Geometry Description

An artery resembles a three-dimensional, highly curved and irregular shape. However, for the sake of simplicity, it is assumed that an artery can be modeled as a 3-D smooth cylindrical tube with constant cross-sectional area. When fatty material such as cholesterol accumulates in the inner lining of the artery, it impedes the upstream flow due to the formation of plaque as a result of the biological response of injury to the endothelium cell. The shape of stenosis is patient-specific and may be an axisymmetric, eccentric, or some arbitrary irregular shape. Therefore, it is difficult to model and mesh such geometries, so an assumption is made that stenosis is axisymmetric and follows a Gaussian profile, as given by equation (3.1). A geometrical configuration with a two-inch unoccluded vessel diameter was used to validate the current numerical results with the experimental investigation by Ahmed and Giddens [17].

Consider a blood flow in a vessel with diameter D and length L along the x -axis as depicted in Figure 3.1. A $4D$ inlet length is provided prior to the stenosis, while a $20D$ outlet length is found to be sufficient so that the flow gradients approach normal values. The shape of the stenosis is defined by Gaussian profile and is dependent upon the axial coordinate x and thus, can be represented as [29]

$$R(x) = \begin{cases} R - \frac{h}{2} \left(1 + \cos \left(\frac{\pi x}{x_s} \right) \right) & |x| \geq x_s \\ R & |x| \leq x_s \end{cases} \quad (3.1)$$

where R is the radius of the unoccluded vessel, h is the maximum height of the stenosis at the throat, x_s is the maximum width of the stenosis, R_s is the radius of the stenosis, and L is the length of the vessel.

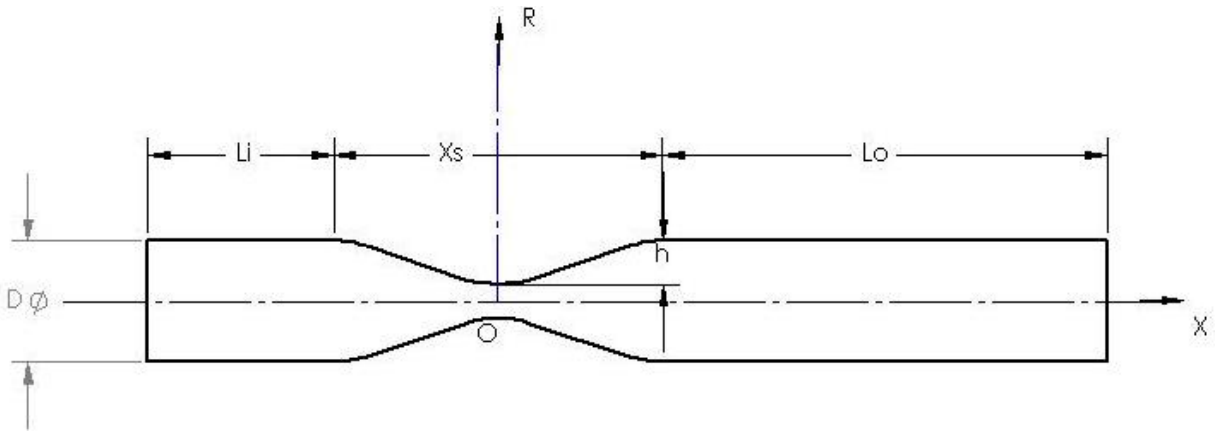


Figure 3.1. Schematic representation of stenotic vessel.

3.3 Severity of Stenosis

The severity of stenosis is defined as the amount of the lumen cross-sectional area narrowed due to the deposition of fatty material, either in terms of percentage reduction in cross-sectional area or percentage reduction in diameter of the lumen.

3.3.1 Percentage Reduction in Cross-Sectional Area

The percentage reduction in cross-sectional area is defined as the amount of cross-sectional area of lumen blocked due to the accumulation of cholesterol and other fatty substances, or

$$\begin{aligned} \% \text{ reduction in area } (dA\%) &= \left(\frac{\pi R^2 - \pi (R-h)^2}{\pi R^2} \right) \\ &= \left[1 - \left(1 - \frac{h}{R} \right)^2 \right] \end{aligned} \quad (3.2)$$

3.3.2 Percentage Reduction in Diameter

The percentage reduction in diameter of the lumen is defined as the amount of diameter blocked due to the accumulation of cholesterol and other fatty substances, or

$$\begin{aligned} \% \text{ reduction in diameter } (dD \%) &= \left[\frac{(D - D_s)}{D} \right] \times 100 \\ &= \left[1 - \frac{D_s}{D} \right] \times 100 \end{aligned} \quad (3.3)$$

It should be noted that only the percentage reduction in area is considered for the current study. Table 3.1 provides the most frequently used reductions by area and their equivalent reductions by diameter for the stenotic geometry against a non-dimensional $\frac{h}{R}$ ratio. For the current work, stenotic vessels with 60%, 75%, and 90% reduction by area were considered, which are equivalent to 36.75%, 50%, and 68.38% reduction by diameter, respectively. Once the geometry was chosen, the next step was to generate a high-quality mesh for the CFD simulations.

TABLE 3.1

REDUCTION OF STENOTIC VESSELS BY AREA AND THEIR EQUIVALENT
REDUCTION BY DIAMETER AGAINST NON-DIMENSIONAL $\frac{h}{R}$ RATIO

$\frac{h}{R}$	Reduction in Area (%)	Reduction in Diameter (%)
0	0	0
0.1340	25	13.40
0.2929	50	29.29
0.5000	75	50
1	100	100

3.4 Grid Generation Considerations

Grid generation is a vital aspect of CFD simulations. A good grid is required in order to achieve a better convergence and reduce numerical errors for the flow field under assessment. Several parameters are responsible for a successful simulation. They are either independent of the problem under investigation or dependent upon the flow field being simulated. Independent parameters are equiangle skewness, aspect ratio and size change, etc.; while dependent parameters are reliant upon the physics of the problem under investigation. These dependent parameters include the necessity to have a fine grid near the wall for wall-bounded turbulent viscous flow in order to achieve wall y^+ , nearly a value of unity, or very fine near-wall mesh in order to capture the smallest possible eddies that exist in the domain for large-eddy simulations. As stated previously, “meshing for physics” drives the requirement for the mesh, and since the flow field under examination is a viscous, incompressible, internal flow, the transition to turbulence is expected in the domain. According to the physics of the problem, it is necessary to have a very fine near-wall mesh in order to achieve a wall $y^+ \cong 1$. Furthermore, there will be a transition to turbulence in the flow field downstream of the stenosis due to local constriction that

exists in the geometry. The extent of turbulence will depend upon the upstream-flow conditions and degree of constriction. Therefore, proper mesh resolution is necessary in the axial direction as well as in the direction normal to the wall, in order to capture the proper length scales of turbulence. A variety of approaches was explored in order to consider the above-specified requirements for the grid generation.

3.5 Grid Generation Approach

Figure 3.2 shows an unstructured grid generated for a 75% area reduction, while Figure 3.3 shows a multi-block structured mesh for the same. For both meshes, a boundary layer was imposed near the wall that advances in the domain. However, a multi-block structured grid is preferred over an unstructured grid due to certain advantages, which will be explained.

There is a notable difference between an unstructured mesh and a multi-block structured mesh, since the multi-block structured mesh provides the feasibility to control the number of grid points in the direction normal to the wall as well as in the axial and radial directions. This feature is inherited due to the decomposition of the solution domain in multiple meshable sub-volumes with the help of Boolean operations that allow us to control the grid points in the area of interest, i.e., in the direction normal to the wall due to the formation of extra edges and faces, while an unstructured grid cannot do this. This attribute of the multi-block structured grid is advantageous in controlling the number of cell counts, in enabling the capture of near-wall turbulence, and in improving the overall mesh quality. Due to the lack of ability to incorporate the grid points in the direction normal to the wall, an unstructured grid unnecessarily increases the number of grid points, even in the region where it is not required; thus, computational time increases.

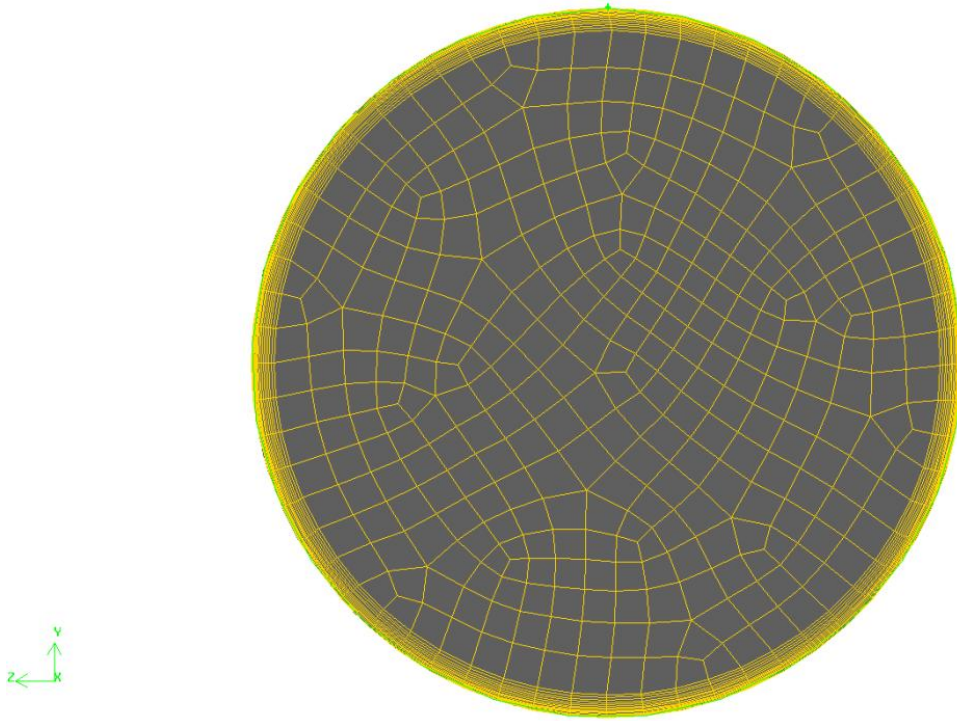


Figure 3.2. Front view of unstructured grid for 75% area reduction.

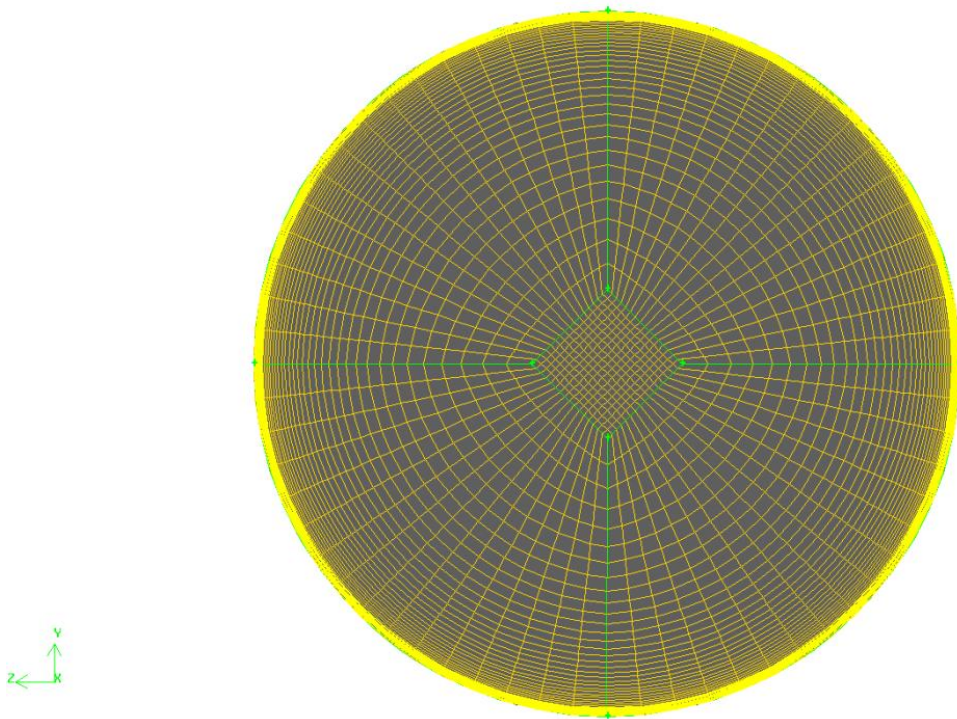


Figure 3.3. Front view of multi-block structured grid for 75% area reduction.

A multi-block structured grid consists of hexahedral cells in 3-D or quadrilateral cells in 2-D, which in turn reduces the truncation error compared to an unstructured counterpart when aligned with the flow [38]. In addition, it also enhances the grid qualities in terms of skewness and aspect ratio. However, there exists a certain disadvantage associated with a multi-block structured grid, since it is required to decompose a solution domain in multiple meshable sub-volumes with the help of Boolean operations. This approach is time-consuming in modeling and meshing a multi-block structured mesh compared to an unstructured counterpart. For the current simulation, the solution domain was divided into 15 sub-volumes to generate a multi-block structured grid.

3.6 Parameters of Grid Quality Test

A successful grid generation using structured or unstructured methodology does not guarantee a better grid for CFD simulations. Therefore, it is important to check whether the mesh is of high quality or poor quality to carry out the CFD simulations because the abnormal values of skewness or aspect ratio are responsible for the error associated with the numerical scheme or results in poor convergence. The commercial grid-generation package GAMBIT 2.4.6 was used as a pre-processing tool for the current work. This software provides certain options to check whether a grid is adequate or inadequate, i.e., mainly equiangle skew (EAS), aspect ratio, and size change.

3.6.1 Equiangle Skew

An equiangle skew (*EAS*) criterion applies to quadrilateral cells in 2-D, or hexahedral, triangular, or tetrahedral cells in 3-D. For the current work, a multi-block structured mesh with hexahedral cells was employed. Therefore, the equiangle skew criteria based on the angle deviation was utilized and thus defined [37] as

$$EAS = \left[\frac{\theta_{\max} - \theta_{eq}}{180 - \theta_{eq}}, \frac{\theta_{eq} - \theta_{\min}}{\theta_{eq}} \right] \quad (3.4)$$

where

θ_{\max} = maximum angle of a face or a cell (degree)

θ_{\min} = minimum angle of a face or a cell (degree)

θ_{eq} = angle of an equilateral face or cell (degree)

Table 3.2 [37] describes the mesh quality based on the equiangle skewness criteria. A scale of 0 means that grid lines are orthogonal to each other, or that a cell or a face is equilateral, while a scale of 1 represents a distorted cell. An EAS scale of 0.1 describes an excellent mesh for 2-D geometry, while an EAS scale of 0.4 describes an excellent mesh for 3-D geometry [37]. Table 3.3 shows an output produced by the GAMBIT 2.4.6 transcript window based on equiangle skew criteria for a grid G3 having 1,624,832 cell counts.

TABLE 3.2

MESH QUALITY BASED ON EQUIANGLE SKEWNESS CRITERIA

Equiangle Skew Range (<i>EAS</i>)	Quality of Element
0	Equilateral
0–0.25	Excellent
0.25–0.50	Good
0.50–0.75	Fair
0.75–0.9	Poor
0.9–1	Very Poor
1	Degenerate

TABLE 3.3
RANGE OF EQUIANGLE SKEWNESS FOR GRID G3

From Value	To Value	Count in Range	% of Total Count (1,624,832)
0.0	0.1	1,399,175	86.11
0.1	0.2	119,388	7.35
0.2	0.3	64,735	3.98
0.3	0.4	32,226	1.98
0.4	0.5	7,924	0.49
0.5	0.6	1,384	0.09
0.6	0.7	0	0
0.7	0.8	0	0
0.8	0.9	0	0
0.9	1.0	0	0
0.0	1.0	1,624,832	100

The measured minimum value of cell skewness is 1.30573e-010, while the measured maximum value for skewness is 0.5 for the given grid. As shown in Table 3.3, the grid consists of 1,624,832 cells, of which 1,399,175 or 86.11% fall in the EAS range of 0 to 0.1.

Figure 3.4 illustrates the location where the grid quality test based on the EAS criteria is explored using “examine the mesh” feature available in GAMBIT 2.4.6, while Figure 3.5 illustrates the close-up view of the cross section shown in Figure 3.4. Figures 3.5 and 3.6 represents the grid quality criteria based on the color-coding scheme provided by GAMBIT 2.4.6.

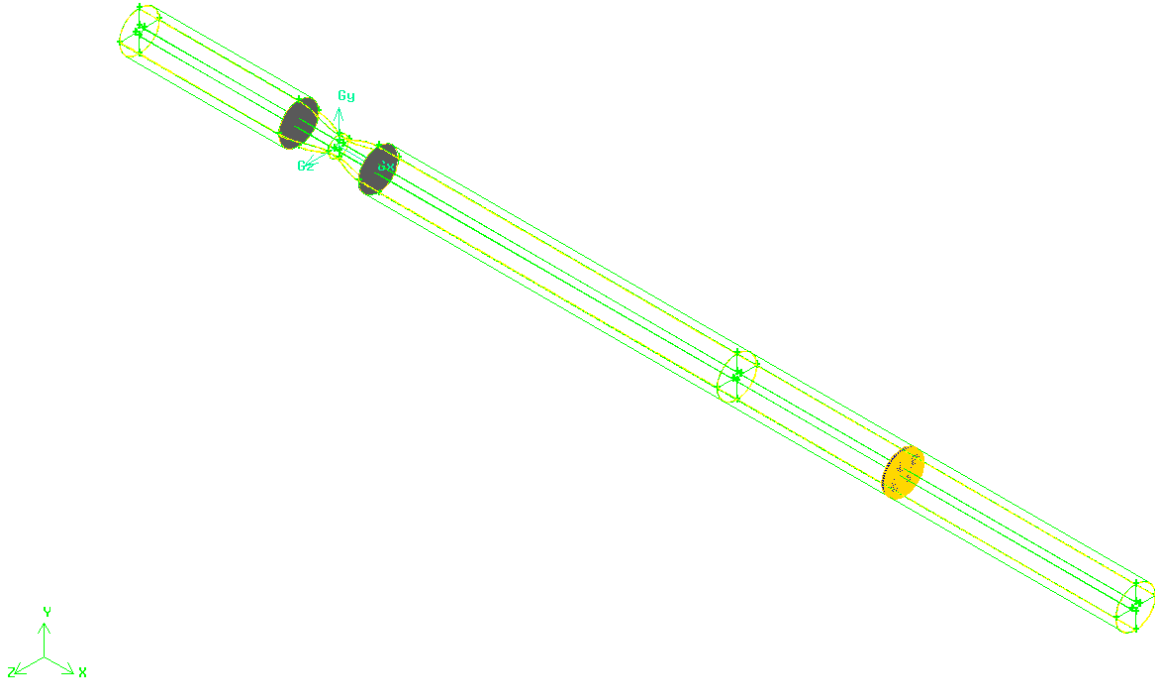


Figure 3.4. Isometric view of grid for mesh quality test along the constant X.

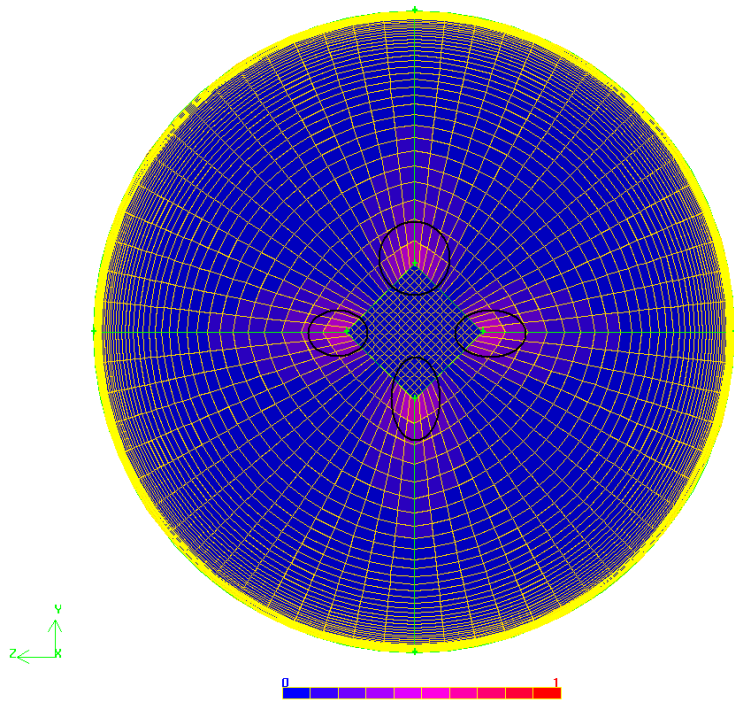


Figure 3.5. Grid quality test based on equiangle skew criteria (wireframe option enabled).

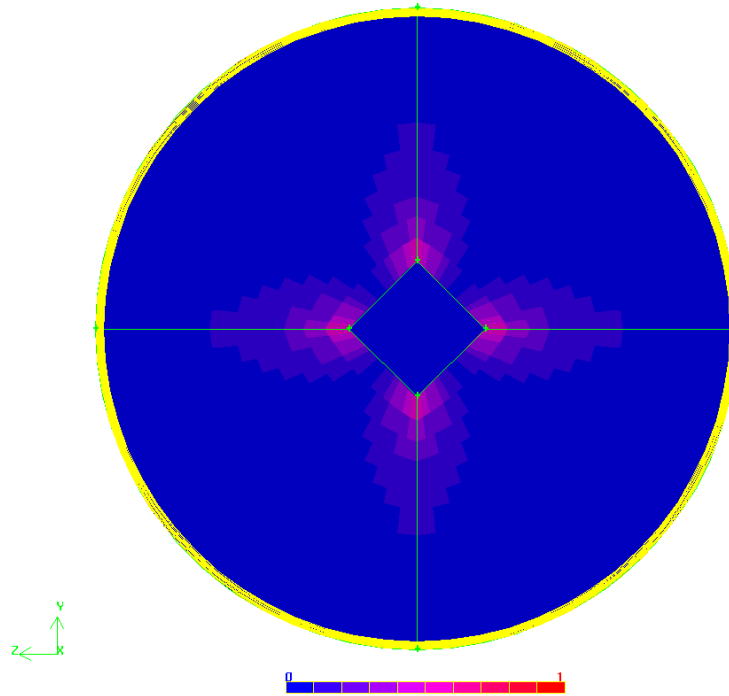


Figure 3.6. Grid quality test based on equiangle skew criteria (wireframe option disabled).

A scale of 0 represents a perfectly equilateral cell and is represented by the color blue, while a scale of 1 is distinguished by the color red . Since the multi-block structured mesh was used for the current work, a branch cut was used to split the cylinder in order to generate an O-type grid. Therefore, the worst elements are located near the intersection of a branch cut and the cylinder with an EAS value of 0.5 and are distinguished with the help of black circles in Figure 3.5. Figure 3.6 describes the same point, except the wireframe option is disabled in it. It is worthwhile to note that the color used to represent a boundary layer in GAMBIT is white; however, this has been changed to yellow for better clarity.

3.6.2 Aspect Ratio

Aspect ratio (AR) is defined as the ratio of maximum dimension of a face or cell to the minimum dimension of a face or cell. For hexahedral cells, it is evaluated as [37]

$$AR = \frac{[e_1, e_2, e_3]_{\max}}{[e_1, e_2, e_3]_{\min}} \quad (3.5)$$

where e_i ($i=1,2,3$) is the average length of the edges in the x-, y-, and z-coordinate directions, respectively, for 3-D hexahedral cells [37]. A higher aspect ratio describes the stretching of a cell and should be avoided in order to achieve accurate results. Therefore, it is recommended that the aspect ratio in the boundary layer should fall in the range of 20 to 100. If the boundary layer capabilities are not used, then an aspect ratio greater than 5 should be avoided. Figure 3.7 shows the four different views of the worst element located in the geometry.

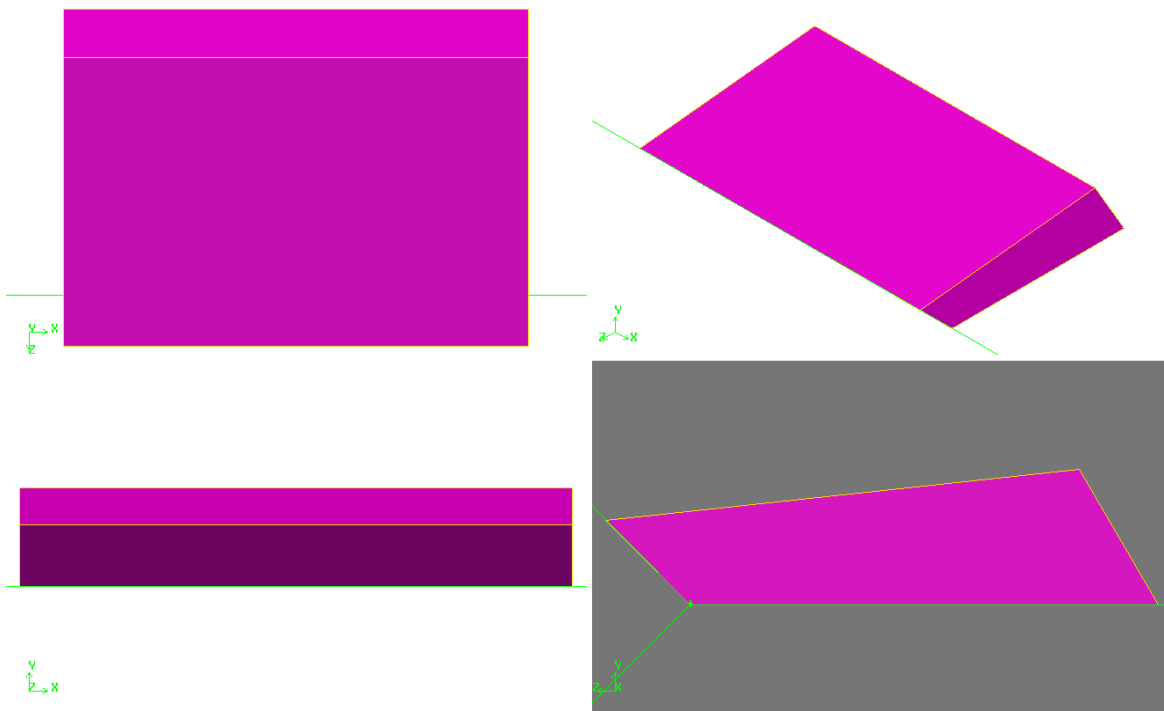


Figure 3.7. Four different views of worst element located in geometry.

3.6.3 Size Change

Size change (Q_{SC}) is a grid-quality measure that is applicable to two-dimensional or three-dimensional elements. For 3-D elements, it is defined as a change of volume between two successive cells that share at least one common face, and it is represented [37] as

$$r_j = \frac{V_i}{V_j} \quad (3.6)$$

Therefore, size-change matrices are deduced [37] as

$$Q_{SC} = [r_1, r_2, \dots, r_n]_{\max} \quad (3.7)$$

Normally $Q_{SC} \geq 0$ is expected. A size-change matrix of 1 represents two successive cells having the same dimension in all three directions and is highly desirable [37]. For the current work, the maximum value of the size-change matrices in grid G3 was 3.27.

CHAPTER 4

NUMERICAL FORMULATION

4.1 Introduction

This chapter deals with the considerations required for the solution of the steady and pulsatile flow conditions, such as governing equations, boundary conditions, numerical formulation of the problem including detailed considerations of the two-equation turbulence model, and the solution discretization.

4.2 Governing Equations

Blood is assumed to be an incompressible, Newtonian fluid with constant viscosity and density. Therefore, the Navier-Stokes equation can be given by [39]

$$\frac{\partial u_i}{\partial x_i} = 0 \quad (4.1)$$

$$\frac{\partial u_i}{\partial t} + u_j \frac{\partial u_i}{\partial x_j} = \frac{-1}{\rho} \left(\frac{\partial p}{\partial x_i} \right) + \nu \frac{\partial^2 u_i}{\partial x_j \partial x_j} \quad (4.2)$$

4.3 Standard $k - \omega$ Turbulence Model

Turbulent flows are characterized by random fluctuations of the flow variables in three dimensions. It is difficult to solve the Navier-Stokes equation since various scales of turbulence are associated with it. In order to do so, the instantaneous component of the solution variable, such as pressure, velocity etc., can be thought of as a contribution from the mean or time-averaged value and fluctuating value [40]:

$$\begin{aligned} u &= \bar{u} + u' \\ v &= \bar{v} + v' \\ w &= \bar{w} + w' \\ p &= \bar{p} + p' \end{aligned} \quad (4.3)$$

The modification of the Navier-Stokes equation is then carried out by taking the time average of each term appearing in the Navier-Stokes equation, and after certain algebraic simplifications, the continuity and momentum equation reduces to equations (4.4) and (4.5). Since each term is time-averaged, this equation is referred to as a Reynolds averaged Navier-Stokes (RANS) equation. During this procedure, several additional unknown parameters appear which require additional equations to be introduced as turbulence models. The set of RANS equations are [42]:

$$\frac{\partial}{\partial t}(\rho) + \frac{\partial}{\partial x}(\rho u_i) = 0 \quad (4.4)$$

$$\frac{\partial}{\partial t}(\rho u_i) + \frac{\partial}{\partial x_j}(\rho u_i u_j) = -\frac{\partial p}{\partial x_i} + \frac{\partial}{\partial x_j} \left[\mu \left(\frac{\partial u_i}{\partial x_j} + \frac{\partial u_j}{\partial x_i} - \frac{2}{3} \delta_{ij} \left(\frac{\partial u_l}{\partial x_l} \right) \right) \right] + \frac{\partial}{\partial t}(-\overline{\rho u_i u_j}) \quad (4.5)$$

In equation (4.5), an additional term, $-\overline{\rho u_i u_j}$, known as the Reynolds's stress tensor, is an additional unknown Boussinesq suggested that for turbulent flow, shear stress can be thought of as being similar to Newton's law of viscosity. However, shear stress in a turbulent flow is due to the transverse momentum of the fluid and can be thought of as a contribution from the laminar and turbulent flow conditions rather than a separate turbulent shear stress. This gives rise to an additional unknown parameter known as eddy viscosity. If one equation is required to solve eddy viscosity, then it is referred to as a one-equation turbulence model; if two equations are required to solve eddy viscosity, then it is referred to as a two-equation turbulence model. Reynolds stress terms can be approximated by using Boussinesq's hypothesis [42]:

$$-\overline{\rho u_i u_j} = \mu_t \left(\frac{\partial u_i}{\partial x_j} + \frac{\partial u_j}{\partial x_i} \right) - \frac{2}{3} \left(\rho k + \mu_t \frac{\partial u_k}{\partial x_k} \right) \quad (4.6)$$

As discussed previously, eddy viscosity can be modeled as a function of the turbulence kinetic energy (k) and specific dissipation rate (ω); therefore it is referred to as the two-equation

turbulence model. Turbulence kinetic energy and specific dissipation rate are given by equations (4.7) and (4.8) [42]:

$$\frac{\partial}{\partial t}(\rho k) + \frac{\partial}{\partial x_i}(\rho k u_i) = \frac{\partial}{\partial x_j} \left(\Gamma_k \frac{\partial k}{\partial x_j} \right) + G_k - Y_k \quad (4.7)$$

$$\frac{\partial}{\partial t}(\rho \omega) + \frac{\partial}{\partial x_i}(\rho \omega u_i) = \frac{\partial}{\partial x_j} \left(\Gamma_\omega \frac{\partial \omega}{\partial x_j} \right) + G_\omega - Y_\omega \quad (4.8)$$

where Γ_k, Γ_ω are the effective diffusivity due to turbulent kinetic energy and specific dissipation rate, respectively; G_k, G_ω are the generation of the turbulent kinetic energy and specific dissipation rate, respectively; and Y_k, Y_ω represents the destruction term for the same. Effective diffusivity can be represented as the function of the turbulent Prandtl number and represented as

$$\Gamma_k = \mu + \alpha^* \left(\rho \frac{k}{\omega} \right) \frac{1}{\sigma_k} \quad (4.9)$$

$$\Gamma_\omega = \mu + \alpha^* \left(\rho \frac{k}{\omega} \right) \frac{1}{\sigma_\omega} \quad (4.10)$$

The difference between the standard $k-\omega$ model and its transitional variant is due to the introduction of the low Reynolds number correction coefficient (α^*). Since α^* is directly proportional to eddy viscosity, a scale of $\alpha^* = 0$ resulting in a turbulent viscosity of 0 implies that laminar conditions prevail. If $\alpha^* = 1$, then it assumes the standard $k-\omega$ model. Therefore, a low Reynolds number correction factor controls the influence on the overall structure of the flow field, depending upon the local flow conditions, and it is given as

$$\alpha^* = \alpha_\infty^* \left(\frac{\alpha_0^* + \frac{\text{Re}_t}{\text{Re}_k}}{1 + \frac{\text{Re}_t}{\text{Re}_k}} \right) \quad (4.11)$$

where $Re_t = \frac{\rho}{\mu} \left(\frac{k}{\omega} \right)$, while Re_k , α_0^* and β_i are the model constants given by 6, 0.024, and 0.072, respectively.

The turbulence kinetic energy is given by [42]

$$G_k = -\overline{\rho u_i u_j} \frac{\partial u_j}{\partial x_i} \quad (4.12)$$

Therefore, production of the specific dissipation rate is evaluated from equation (4.12):

$$G_w = \alpha \left(\frac{\omega}{k} \right) G_k \quad (4.13)$$

The coefficient α can be given similarly from equation (4.11) as:

$$\alpha = \frac{\alpha_0}{\alpha^*} \left(\frac{\alpha_0 + \frac{Re_t}{Re_\omega}}{1 + \frac{Re_t}{Re_\omega}} \right) \quad (4.14)$$

where $R_w = 2.95$, and α^* is governed by equation 4.11,

The dissipation of the k is given by [42]

$$Y_k = \rho \beta^* f_{\beta^*} k \omega \quad (4.15)$$

where

$$f_{\beta^*} = \begin{cases} 1 & \chi_k \leq 0 \\ \frac{1 + 680 \chi_k^2}{1 + 400 \chi_k^2} & \chi_k > 0 \end{cases} \quad (4.16)$$

where

$$\chi_k = \frac{1}{\omega^3} \left(\frac{\partial k}{\partial x_j} \right) \left(\frac{\partial \omega}{\partial x_j} \right) \quad (4.17)$$

$$\beta^* = \beta_i^* [1 + \zeta^* F(M_t)] \quad (4.18)$$

$$\beta_i^* = \beta_\infty^* \left[\frac{0.2666 + \left(\frac{Re_t}{R_\beta} \right)^4}{1 + \left(\frac{Re_t}{R_\beta} \right)^4} \right] \quad (4.19)$$

Similarly, the dissipation of ω is given by [41]

$$Y_\beta = \rho \beta_i f_\beta \omega^2 \quad (4.20)$$

where auxiliary relations can be given by [41]

$$f_\beta = \frac{1 + 70\chi_\omega}{1 + 80\chi_\omega} \quad (4.21)$$

$$\chi_\omega = \left| \frac{\Omega_{ij} \Omega_{jk} S_{ki}}{(\beta_\infty^*)^3} \right| \quad (4.22)$$

$$\Omega_{ij} = \frac{1}{2} \left(\frac{\partial u_i}{\partial x_j} - \frac{\partial u_j}{\partial x_i} \right) \quad (4.23)$$

Table 4.1 shows the model constant for the transition $k - \omega$ model [41, 42].

TABLE 4.1

MODEL CONSTANT FOR TRANSITIONAL $k - \omega$ Model

Closure Coefficient for the Transitional $k - \omega$ Model					
$\alpha_\infty^* = 1$	$\alpha_\infty = 0.52$	$\alpha_0 = 0.1111$	$\beta_\infty^* = 0.09$	$\beta_i = 0.072$	$R_\beta = 8$
$R_k = 6$	$R_w = 2.95$	$\zeta^* = 1.5$	$M_{t0} = 0.25$	$\sigma_k = 2.0$	$\sigma_w = 2$

4.4 Assumptions

The following assumptions were used for the current numerical efforts:

- Non-Newtonian behavior is found to exist in the smaller vessels such as capillaries. However, a constant shear strain rate 100 sec^{-1} is reported for the vessel with greater than 0.5 mm diameter [43]. Therefore, Newtonian assumption for the blood flow is valid for the current study.
- The shape of the artery is highly curved and irregular. However, for the sake of simplicity, an artery can be thought of as a cylindrical tube with a constant cross-sectional area.
- The shape of the stenosis is patient-specific. It may be eccentric or some irregular arbitrary shape. However, for the sake of simplicity, it is assumed that stenosis follows a cosine curve given by equation (3.1).
- The compliance nature of the artery is not modeled as a result of accumulation of the cholesterol and fatty substances in the arterial wall.
- Waveform in the circulation system can be accurately represented by means of the physiological waveform. However, a sinusoidal pulsatile waveform, rather than a physiological waveform, is imposed at the inlet.

4.5 Boundary Conditions

4.5.1 Velocity Inlet

For steady flow, flow conditions upstream of the stenosis are laminar and fully developed. Therefore, the Reynolds number at the inlet is calculated based on the hydraulic diameter and is defined by

$$\text{Re}_D = \frac{\rho U_{avg} D}{\mu} \quad (4.24)$$

where Re_D = Reynolds number based on the hydraulic diameter, D = diameter of the unoccluded blood vessel, μ = absolute viscosity, and ρ = density of the blood. Density of the blood is considered to be 1050 Kg/m^3 , while viscosity is considered to be $0.003675 \frac{\text{Kg.m}}{\text{sec}}$.

For a fully developed pipe flow, U_{max} is evaluated from the Poiseuille solution as

$$U_{avg} = \frac{1}{2}(U_{max}) \quad (4.25)$$

Therefore, non-dimensional velocity profile at the inlet is calculated as

$$U_x = U_{max} \left(1 - \frac{r^2}{R^2} \right) \quad (4.26)$$

$$U_r = 0 \quad (4.27)$$

$$U_\theta = 0 \quad (4.28)$$

A sine waveform is imposed at the inlet for the pulsatile flow simulations and is given by

$$U(t) = 0.25 \left[1 + \sin \left(2\pi \frac{t}{T} \right) \right] \quad (4.29)$$

4.5.2 Outlet

An outflow boundary condition is provided at the outlet. The outflow boundary condition extrapolates information from the interior of the domain and assumes a zero flux at the outlet normal to the face [42].

4.5.3 Wall

A no-slip boundary condition is specified at the vessel walls.

4.6 Turbulence Boundary Conditions

Additional parameters must be provided to define turbulence at the inlet and outlet [42]. Furthermore, it is also important to provide a proper estimate of turbulence kinetic energy and specific dissipation rate for the flow simulation under assessment. However, it is challenging to estimate the explicit values of turbulence kinetic energy and specific dissipation rate unless experimental values are available. For this purpose, one needs to provide the convenient parameters such as turbulence intensity, length scale, etc., as they are associated with the turbulence kinetic energy and specific dissipation rate through empirical relationships [42]. Several appropriate parameters are used to define the level of turbulence at the inlet and outlet boundary conditions [42]:

- Turbulence Intensity (I)
- Length Scale (l)
- Turbulence Viscosity Ratio $\left(\frac{\mu_t}{\mu}\right)$

Appropriate parameters must be selected for describing turbulence, depending upon the class of the problem under investigation (such as a compressible or incompressible flow, internal or external flow) and the turbulence model under investigation. For example, if the turbulence model under investigation is Spalart-Allamaras, then it is necessary to choose a turbulence viscosity ratio as a turbulence specification parameter since it is appropriate for the given turbulence model. Since current efforts are conducted on blood flow simulations, turbulence intensity and length scale are suitable parameters to describe the level of turbulence at the inlet and outlet boundaries.

4.6.1 Turbulence Intensity

Turbulence intensity (I) is measured as the root mean square of velocity fluctuations to the average velocity [42] as

$$I = \frac{U'_{rms}}{U_{avg}} \quad (4.30)$$

For blood flow simulations, turbulence intensity at the core of a fully developed flow is estimated from the following empirical relationship [42]

$$I = \frac{U'_{rms}}{U_{avg}} \cong 0.16(\text{Re}_D)^{-\frac{1}{8}} \quad (4.31)$$

Therefore, turbulence intensity is calculated as 6.74% from equation (4.31). It is worthwhile to note that since the upstream flow conditions are fully developed and laminar, one can provide turbulence intensity in the range of 0% to 5%.

4.6.2 Length Scale

The turbulent length scale (l) represents the size of the largest eddies that contains energy in a turbulent flow. It is given by an empirical formula [42] as

$$l = 0.07L \quad (4.32)$$

A factor of 0.07 is based on the greatest value of mixing length in a fully developed turbulent pipe flow, while L is the characteristic length scale. An artery resembles the shape of a pipe; therefore, a characteristic length scale (L) is equivalent to the hydraulic diameter (D_H) of a pipe [42]:

$$l = 0.07D_H \quad (4.33)$$

Thus, turbulence kinetic energy is calculated as [42]

$$k = \frac{3}{2} (U_{avg} I)^2 \quad (4.34)$$

So, the specific dissipation rate is evaluated from the turbulence kinetic energy and represented as

$$\omega = \left(\frac{\sqrt{k}}{\sqrt[4]{c_\mu}} \right) l \quad (4.35)$$

where $c_\mu = 0.09$ is an empirical model constant, and l is a turbulent length scale [42].

It can be seen from equations (4.34) and (4.35) that it is simpler to estimate the values for turbulence kinetic energy and specific dissipation rate by means of conveniently derived parameters, such as turbulence intensity and turbulence length scale, rather than providing the explicit values for the turbulence kinetic energy and specific dissipation rate.

4.7 Numerical Discretization

Commercial finite volume package FLUENT 6.3 [42] was used to solve incompressible Navier-Stokes equation with pressure based segregated solver. A parallel version of this software was used with the double precision. Continuity and momentum equations are the governing Navier-Stokes equations for the incompressible flow. Continuity and momentum together produces the four equations with four unknown flow variables, i.e., u , v , w and p . Flow is driven by pressured gradient, which is coupled with velocity in momentum equation and therefore it is required to use guess and correct approach to solve unknown variables since continuity equation is constraint. Semi Implicit Momentum Pressure Linked Equation Consistent (SIMPLEC) algorithm was used for pressure-velocity coupling for steady flow simulations with default value of under-relaxation parameters was utilized. Pressure-Implicit Splitting of Operators (PISO) algorithm was used as a pressure-velocity coupling for transient flow calculation since the large time step sizes were involved in the computations i.e. $1e-3$. Skewness and neighbor correction

were set as default value, i.e., 1. 2nd order upwind discretization scheme was assured for the flow as well turbulence quantities while 2nd order implicit formulation was considered for unsteady flow with 1e-3 convergence criterion was set for all simulations.

CHAPTER 5

STEADY-STATE SIMULATIONS

5.1 Introduction

Blood flow in the human body is pulsatile in nature, due to the pumping action of the heart. The Reynolds number is not constant throughout the circulation system since the diameters of arteries vary, with the largest being the aorta and the smallest being in some of the smaller vessels such as capillaries. For example, the time-averaged Reynolds number in the human aorta is somewhat less than 1500, while in the common carotid artery, it is less than 400 [17]. Therefore, a systematic study is required to understand the effect of the varying Reynolds numbers in the human circulation system in the vicinity of the varying degrees of stenosis and its clinical implication from a fluid dynamics point of view, considering the wall shear stress and effect of turbulence. In this chapter, efforts are made to investigate the range of Reynolds number from 500 to 2000 based on the diameter of the vessel in the vicinity of the stenosis with a 75% area reduction. The same geometry is used for the validation study by Ahmed and Giddens [17] with a two-inch unoccluded diameter of the vessel.

5.2 Non-Dimensionalization

Non-dimensionalization of parameters is used in the current work to ensure better prediction of the results. At the different axial locations, axial velocity (V_x) is non-dimensionalized by the mean velocity (V_m), axial location (X) is non-dimensionalized by an unoccluded tube diameter (D) and the non-dimensional ratio is expressed as $\bar{X} = X/D$. For the wall shear stress study, wall shear stress is non-dimensionalized by the upstream value of shear stress, i.e., value of the shear stress for the pipe flow of the same diameter.

5.3 Assessment of Standard $k-\omega$ Turbulence Model

This section deals with the numerical assessment of the standard $k-\omega$ model for the problem under investigation using velocity profile and turbulence intensity as validation parameters.

5.3.1 Non-Dimensional Axial Velocity Profile of Standard $k-\omega$ Turbulence Model

Figures 5.1 through 5.6 show the non-dimensional velocity profile plotted against the non-dimensional radial distance at axial locations $\bar{X} = 0, 1, 2.5, 4, 5,$ and $6,$ respectively, and compared against the available experimental results from Ahmed and Giddens [17] for different degrees of turbulence intensity.

It is clear that when the flow passes through the stenosis, a jet is formed and the relative magnitude of the velocity exceeds a value four times higher than the mean velocity, as shown in Figure 5.1 at $\bar{X} = 0,$ i.e., throat or minimum cross-sectional area. However, a diverging section follows just after the throat, which is responsible for the adverse pressure gradient, and as a result of jet formation and the adverse pressure gradient, a flow-separation region exists downstream of the stenosis. Figures 5.2 and 5.3 show flow separation at 1 and 2.5 diameters distal to the stenosis, respectively, and these are in good agreement with the experimental values. Experimental data suggests that the flow continues to be separated from the wall even at $\bar{X} = 4,$ 5, as shown in Figures 5.4 and 5.5, respectively, and finally reattaches to the wall at $\bar{X} = 6,$ as shown in Figure 5.6.

However, current simulations predict the flow reattachment at one diameter earlier than the experimental suggested value of $\bar{X} = 6,$ and hence it is not in agreement with the experimental data for the stated value of inlet-specified turbulence intensity. Furthermore, it is quite difficult to differentiate the effect of the turbulence intensity from the non-dimensional

velocity profile, since velocity profiles are overlapping each other, although the magnitude of the turbulence intensity varies. Therefore, further detailed analysis is required to gain more insight into the problem by exploring the effect of turbulence intensity.

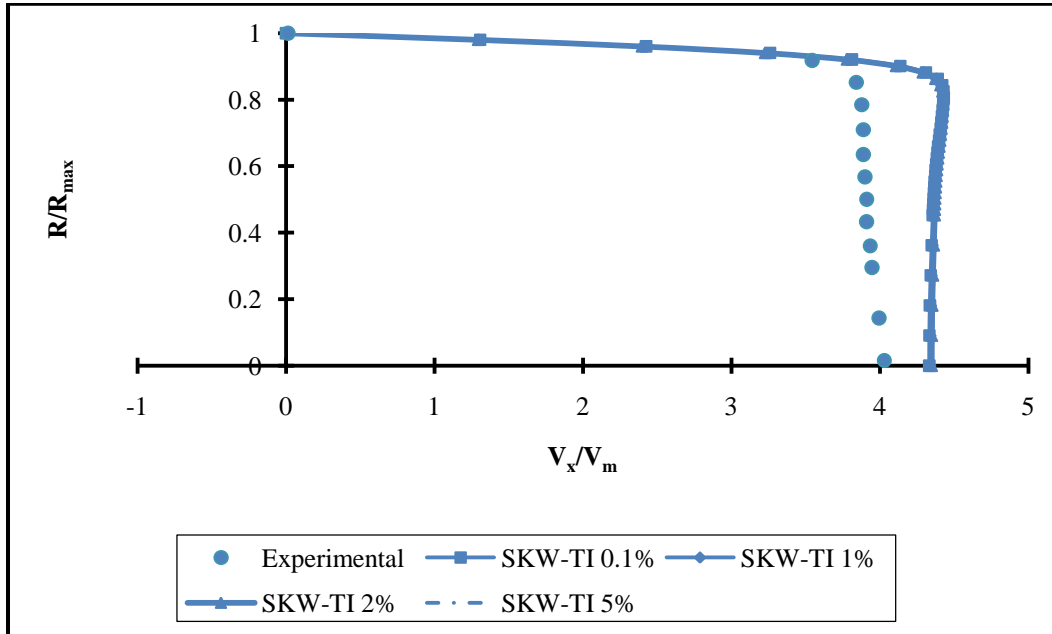


Figure 5.1. Non-dimensional velocity profile at axial location $\bar{X} = 0$.

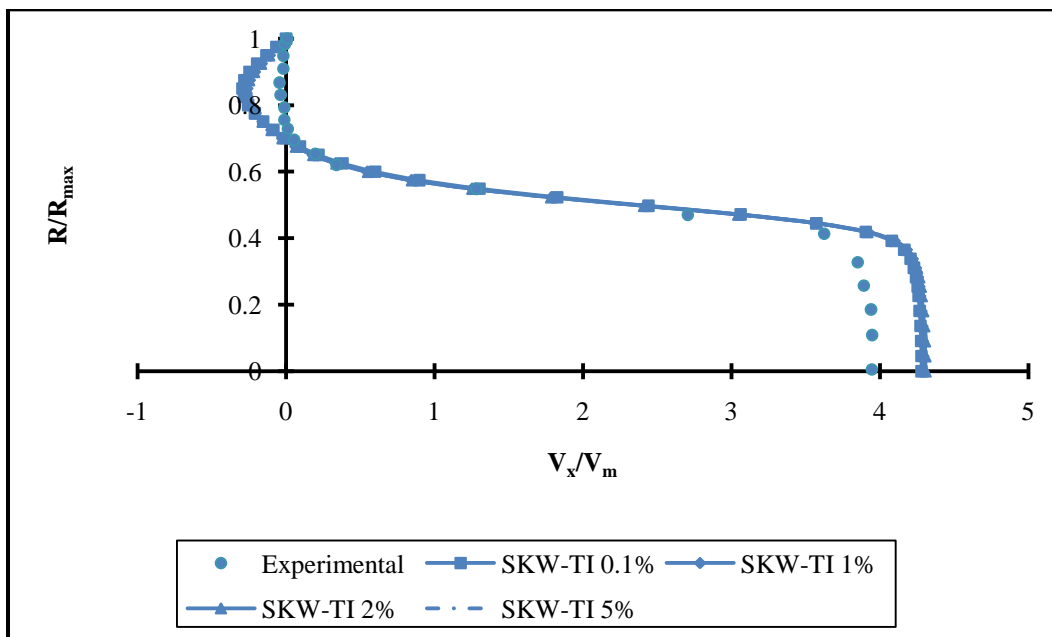


Figure 5.2. Non-dimensional velocity profile at axial location $\bar{X} = 1$.

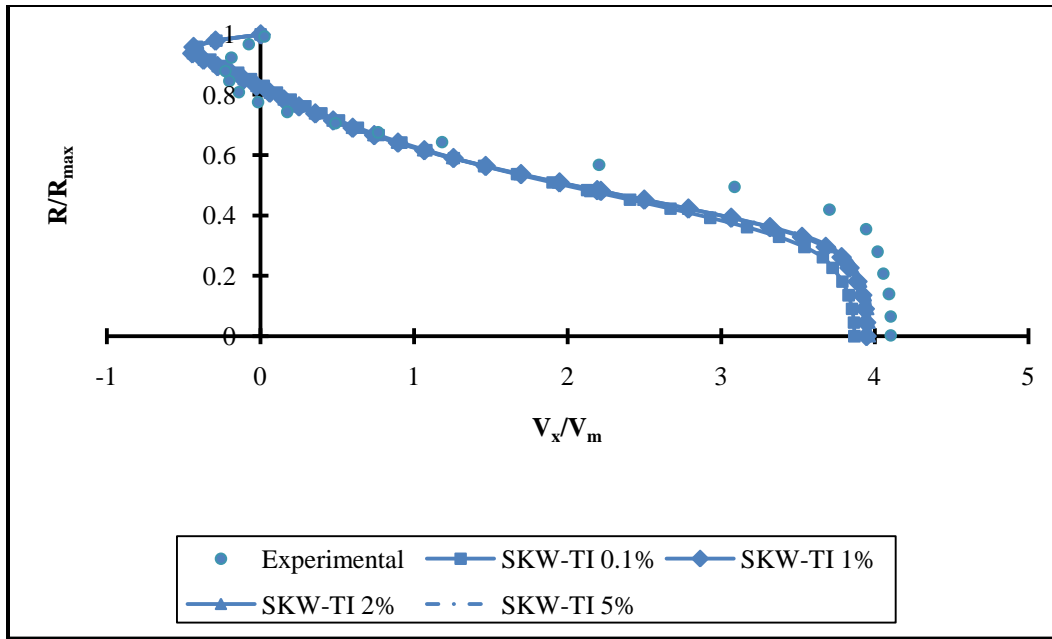


Figure 5.3. Non-dimensional velocity profile at axial location $\bar{X} = 2.5$.

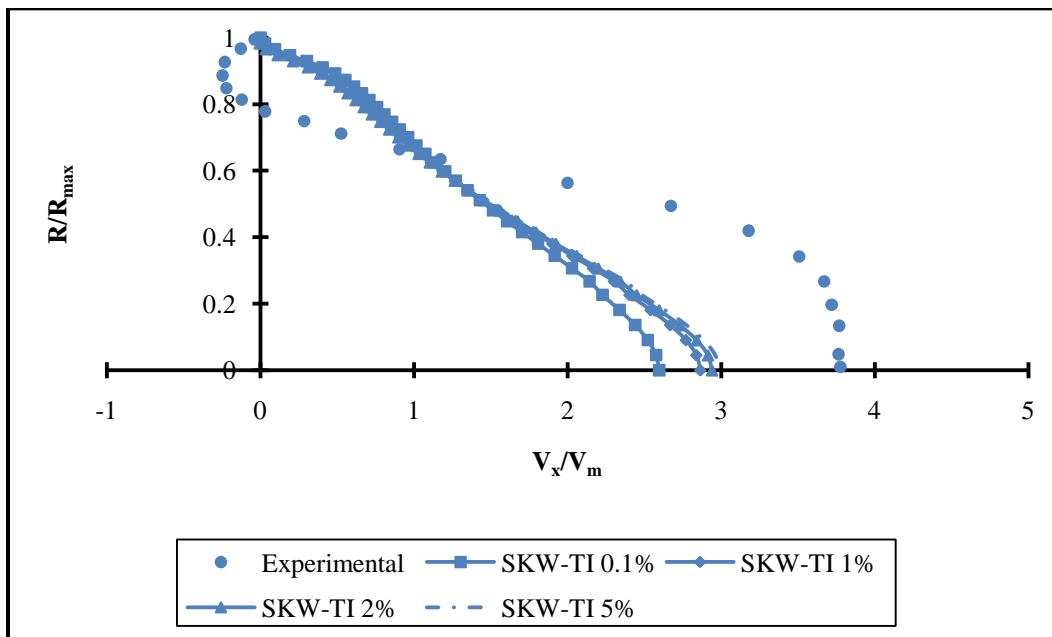


Figure 5.4. Non-dimensional velocity profile at axial location $\bar{X} = 4$.

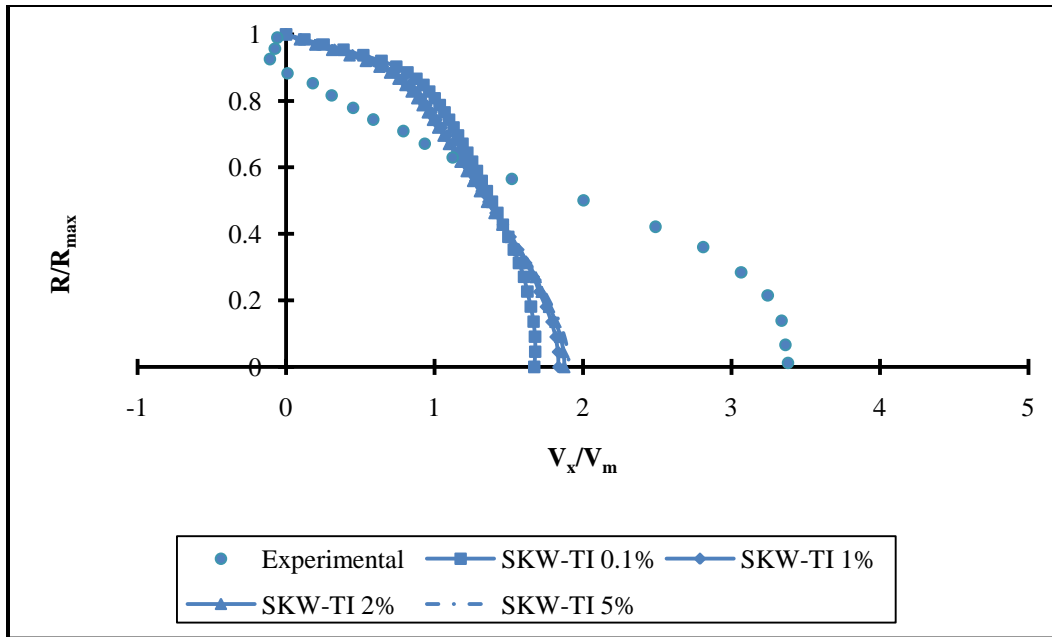


Figure 5.5. Non-dimensional velocity profile at axial location $\bar{X} = 5$.

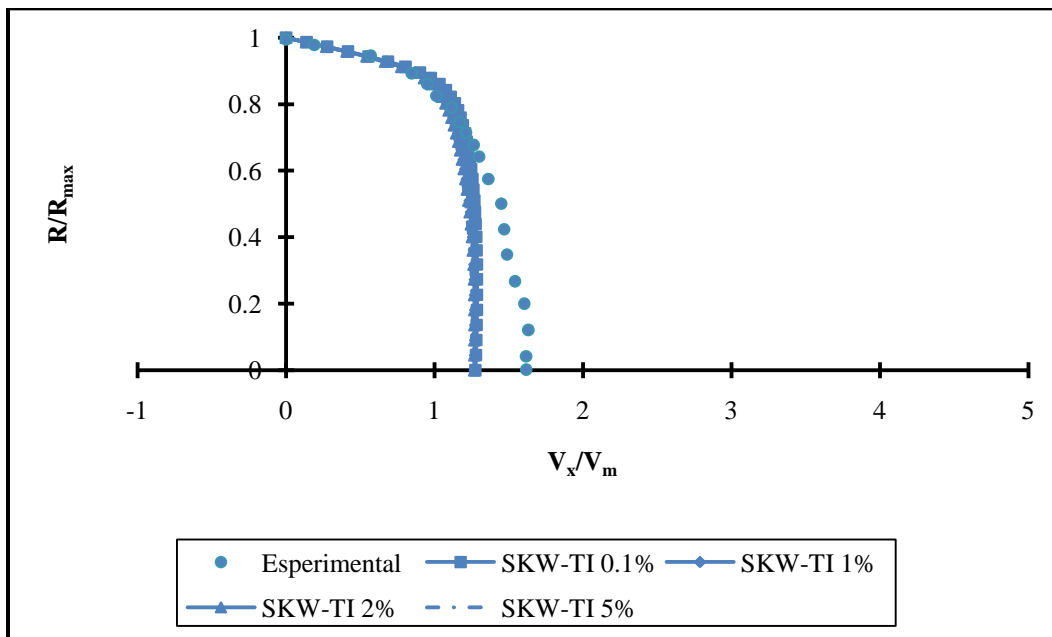


Figure 5.6. Non-dimensional velocity profile at axial location $\bar{X} = 6$.

5.3.2 Turbulence Intensity of Standard $k - \omega$ Turbulence Model

Turbulence intensity is represented in the percentage on the ordinate and is plotted against the non-dimensional distance $\frac{X}{D}$ along the centerline, as shown in Figure 5.7. It is clearly evident from the experimental data that the flow remains laminar upstream of the stenosis as well as a few diameters downstream of the stenosis until $5 < \bar{X} < 6$ for the Reynolds number 1000 with 75% area reduction. However, the current numerical simulation predicts the peak value of turbulence intensity at the throat of the stenosis in the range of 35% to 45%, as compared to the nearly 4% experimental measured value, as shown in Figure 5.8 for the different values of turbulence intensity. Moreover, it also predicts higher values of turbulence intensity proximal to the stenosis, although in reality the upstream flow conditions are laminar.

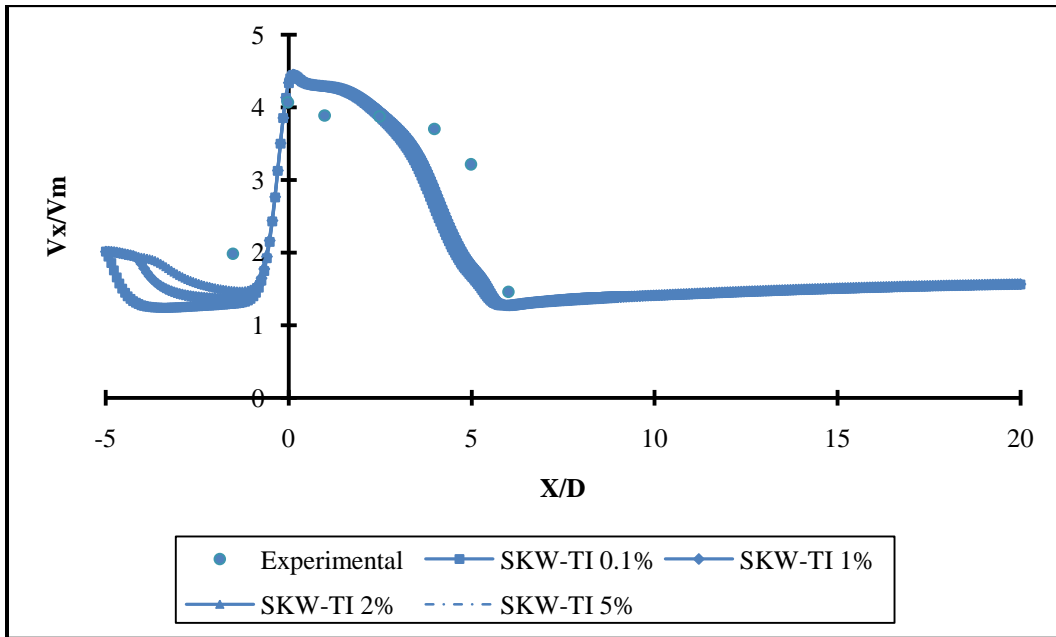


Figure 5.7. Variation of centerline axial velocity for standard $k - \omega$ turbulence model under inlet-specified turbulence intensity.

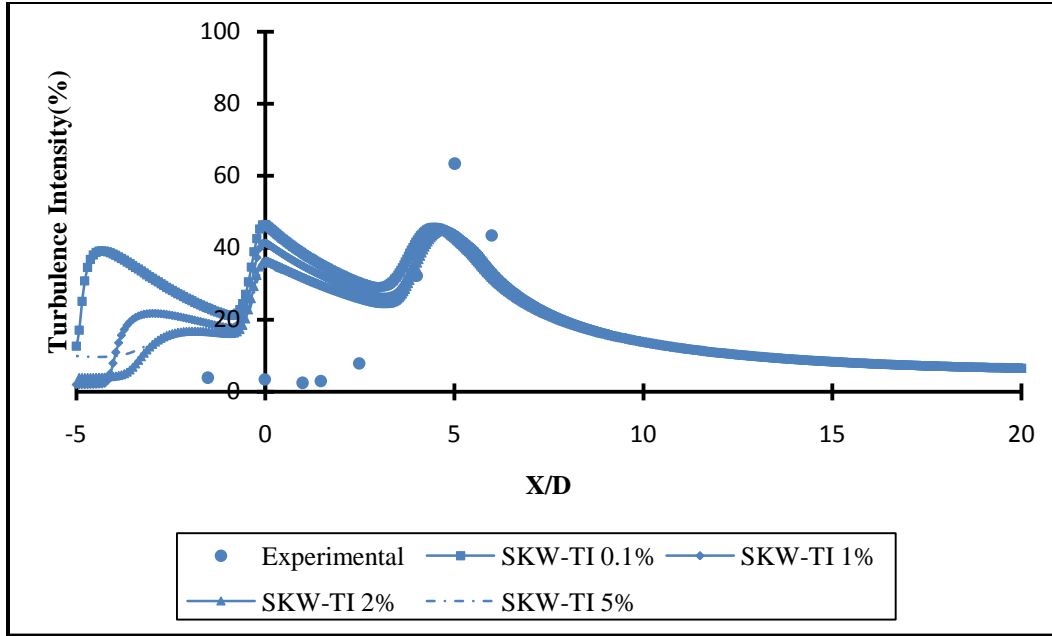


Figure 5.8. Variation of turbulence intensity for standard $k-\omega$ turbulence model under inlet-specified turbulence intensity.

Thus, it can be concluded that the standard $k-\omega$ model fails to predict the correct physics of the current problem, since non-dimensional velocity profiles are not in good agreement downstream of the stenosis. The relative magnitude of the turbulence intensity is much higher upstream of the stenosis and indicates that flow is turbulent even in the laminar region of the flow field.

5.4 Assessment of Transitional $k-\omega$ Turbulence Model

In this section, the transitional variant standard $k-\omega$ model is used to test the efficacy of numerical simulations by comparing it against the experimentally measured values.

5.4.1 Non-Dimensional Axial Velocity Profile of Transitional $k-\omega$ Turbulence Model

Figures 5.9 through 5.14 represent the non-dimensional velocity profiles at the different axial locations and plotted against the non-dimensional radial distance for different values of inlet-specified turbulence intensity. For different values of the inlet turbulence intensity, the non-

dimensional axial velocity profiles are in good agreement at $\bar{X} = 0, 1, \text{ and } 2.5$, which are shown in Figures 5.9, 5.10, and 5.11, respectively. In fact, the experimentally measured value for the non-dimensional velocity profile at $\bar{X} = 2.5$ is in excellent agreement with the inlet turbulence intensity of 5% for the same location, as can be seen in Figure 5.11. However, at the axial locations $\bar{X} = 5$ and 6, shown in Figures 5.13 and 5.14, a large difference between the different amounts of inlet turbulence intensity with the experimental data is observed. It is quite clear from these two figures that inlet turbulence intensities of 0.1% and 1% predict the flow to be separated at those locations.

The axial location $\bar{X} = 6$ (Figure 5.14) is a point of interest. It was established from the experimental data that the flow reattaches somewhere in the area $5 < \bar{X} < 6$, but the inlet specified turbulence intensities of 0.1% and 1% suggest that the flow is not yet reattached. In fact, the turbulence intensity of 0.1% shows that the flow does not reattach until $\bar{X} = 14$. The same results were reported by Verghese et al. [26] who found that flow does not reattach until $\bar{X} = 16$, i.e., the outlet length in their simulation, and eventually ends up with negative wall shear stress at the outlet. However, in this current work, it was found that increasing the inlet turbulence intensity from 0.1% to 5% decreases the reattachment length.

Furthermore, it can be seen in Figures 5.9 to 5.14 that the velocity magnitude of the core flow decreases for a higher degree of turbulence intensity at the same axial location compared to lower turbulence intensity. In addition, it is firmly established that the transitional $k - \omega$ model is sensitive to the inlet turbulence intensity, a fact reported by Banks and Bressloff [30] in their numerical work.

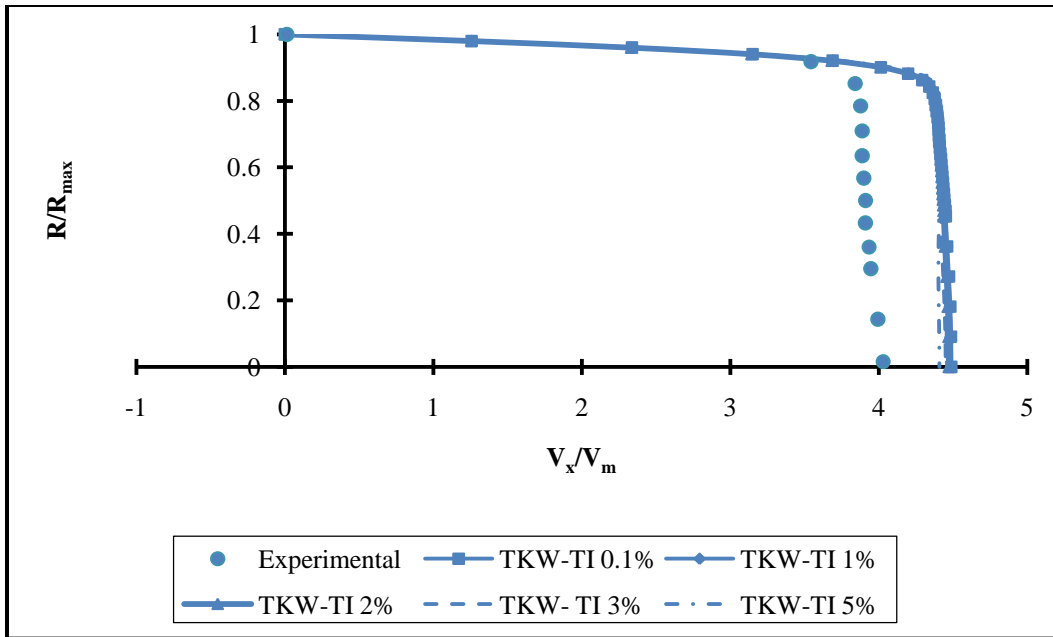


Figure 5.9. Non-dimensional velocity profile at axial location $\bar{X} = 0$.

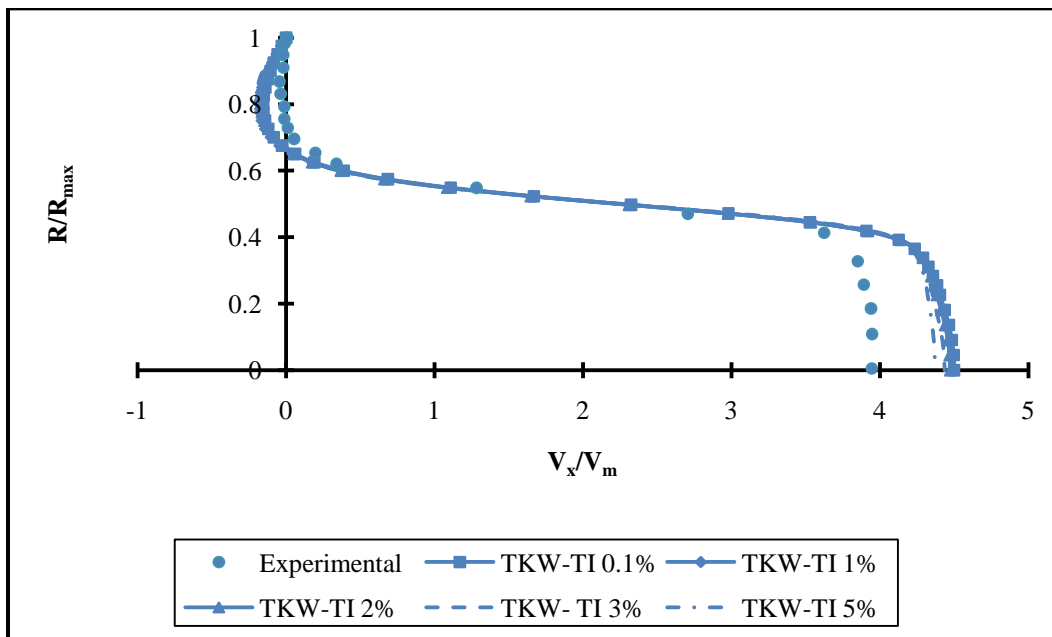


Figure 5.10. Non-dimensional velocity profile at axial location $\bar{X} = 1$.

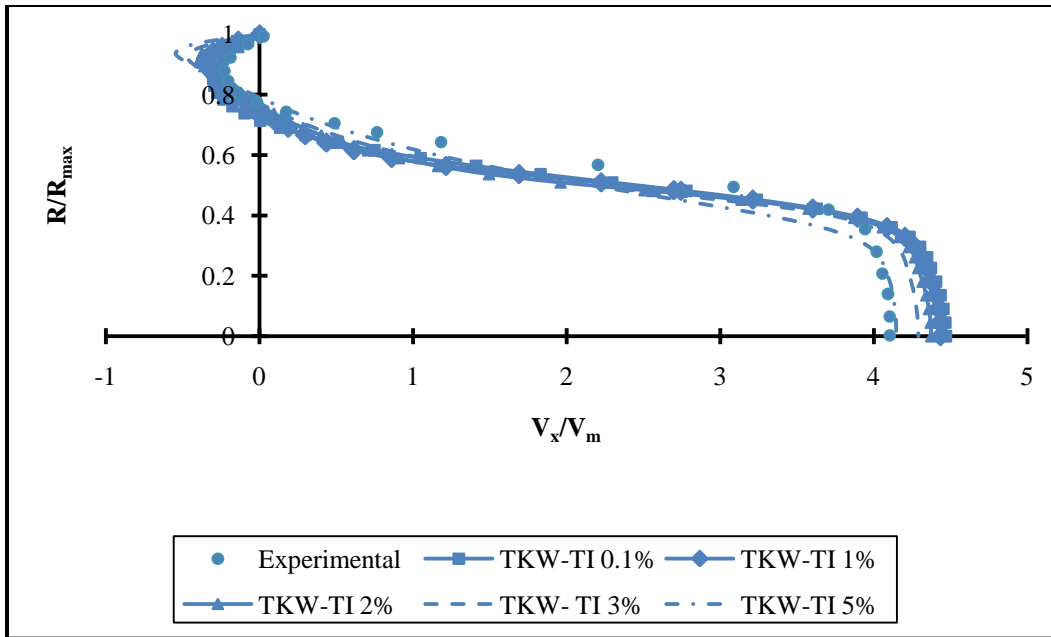


Figure 5.11. Non-dimensional velocity profile at axial location $\bar{X} = 2.5$.

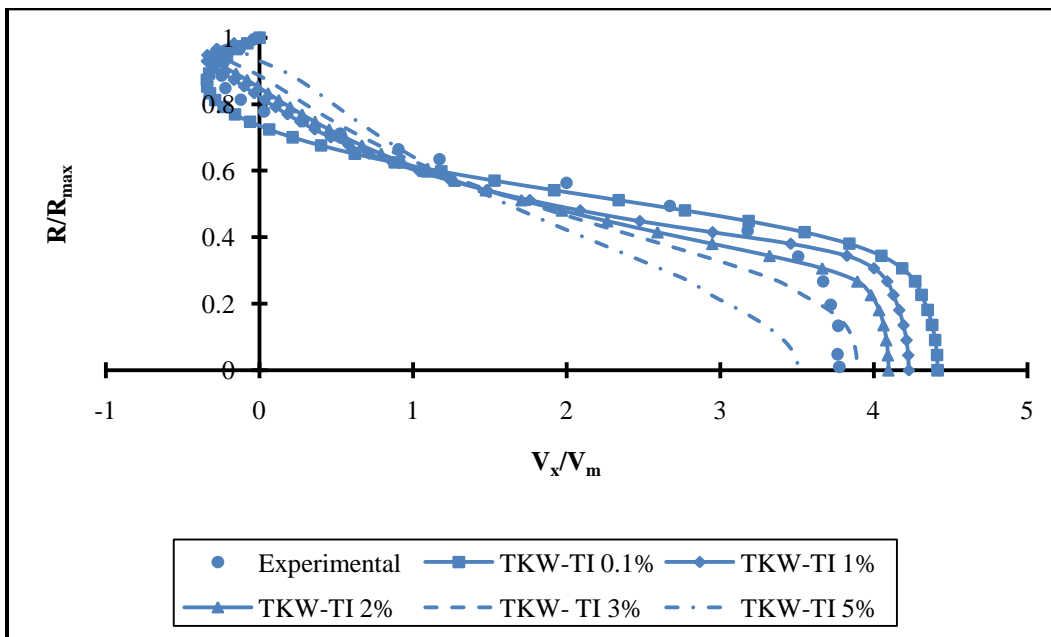


Figure 5.12. Non-dimensional velocity profile at axial location $\bar{X} = 4$.

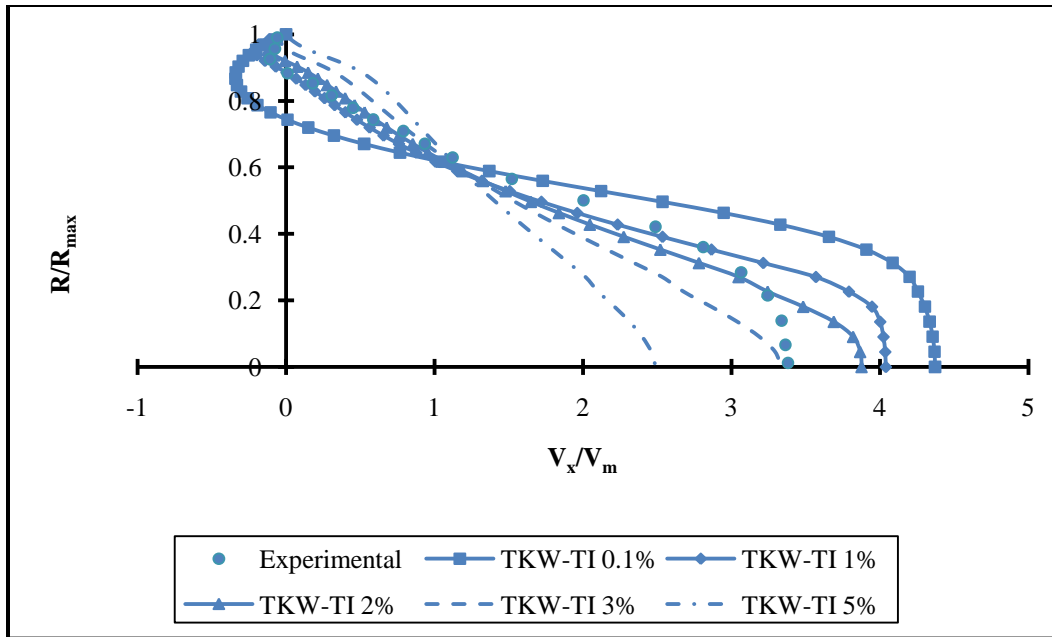


Figure 5.13. Non-dimensional velocity profile at axial location $\bar{X} = 5$.

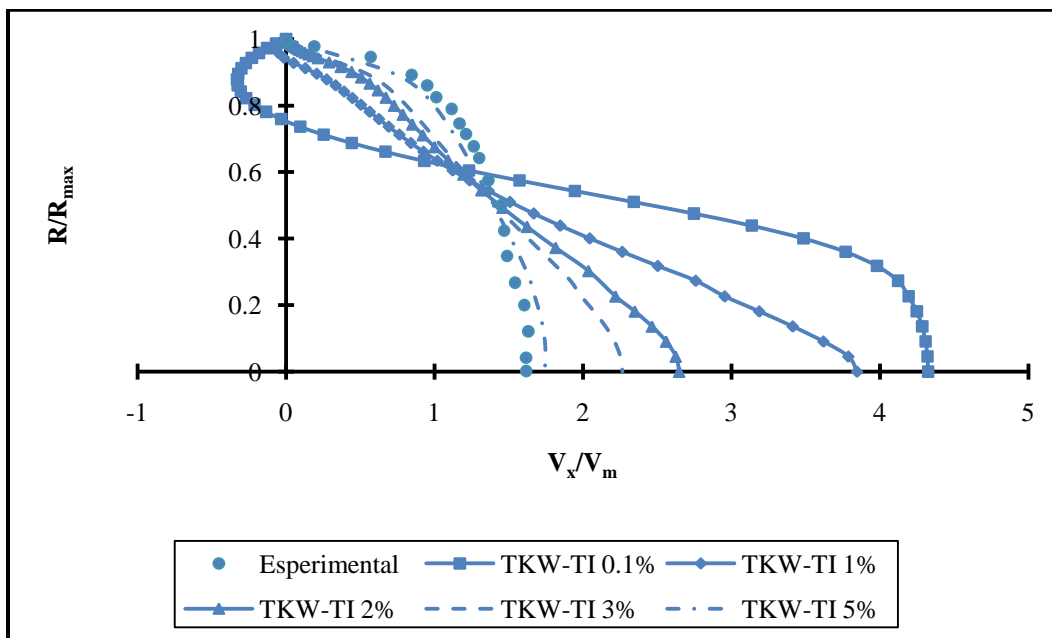


Figure 5.14. Non-dimensional velocity profile at axial location $\bar{X} = 6$.

Figure 5.15 shows the variation of the axial centerline velocity for the different amounts of inlet turbulence intensity in comparison with the experimental data. It appears from Figure 5.15 that the turbulence intensity of 5% shows good agreement with the experimental data, while

a turbulence intensity of 0.1% is not at all in agreement. However, further investigation is required by means of observing the turbulence intensity.

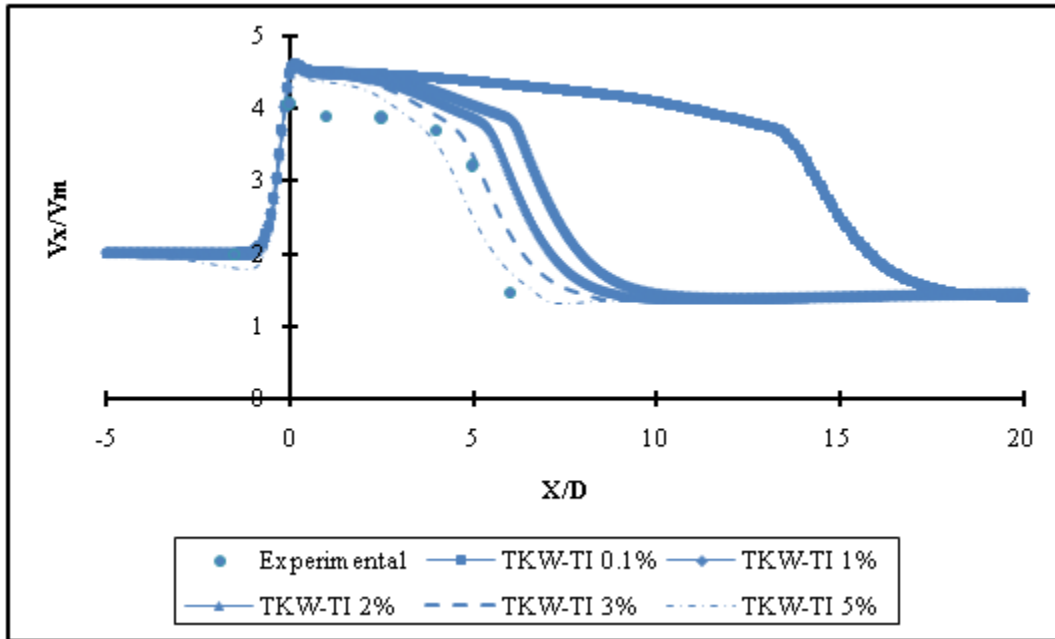


Figure 5.15. Variation of the centerline axial velocity for transitional $k - \omega$ turbulence model under inlet-specified turbulence intensity.

5.4.2 Turbulence Intensity of Transitional $k - \omega$ Turbulence Model

Figure 5.16 shows the variation of the turbulence intensity along the centerline of the blood vessel. It was found that flow remains laminar for most of the flow field for a turbulence intensity of 0.1%. Experimental data suggest that the flow remains laminar proximal to the stenosis and a few diameters downstream of the stenosis. However, increasing the turbulence intensity alters this fact, since turbulence intensities of 0.1%, 1%, and 2% predict that the flow remains laminar proximal to the stenosis and in the throat of the stenosis by agreeing with the experimental data. In contradiction to the earlier findings in terms of non-dimensional velocity profiles where it appears that turbulence intensity of 5% provides a better agreement with the experimental data, here 5% turbulence intensity provides a very high value of turbulence at the throat of the stenosis, i.e., 24% vs. the 4% experimentally measured value. Therefore, a

turbulence intensity of 2% is more suitable for the current work, since a reasonable amount of turbulence is predicted by it.

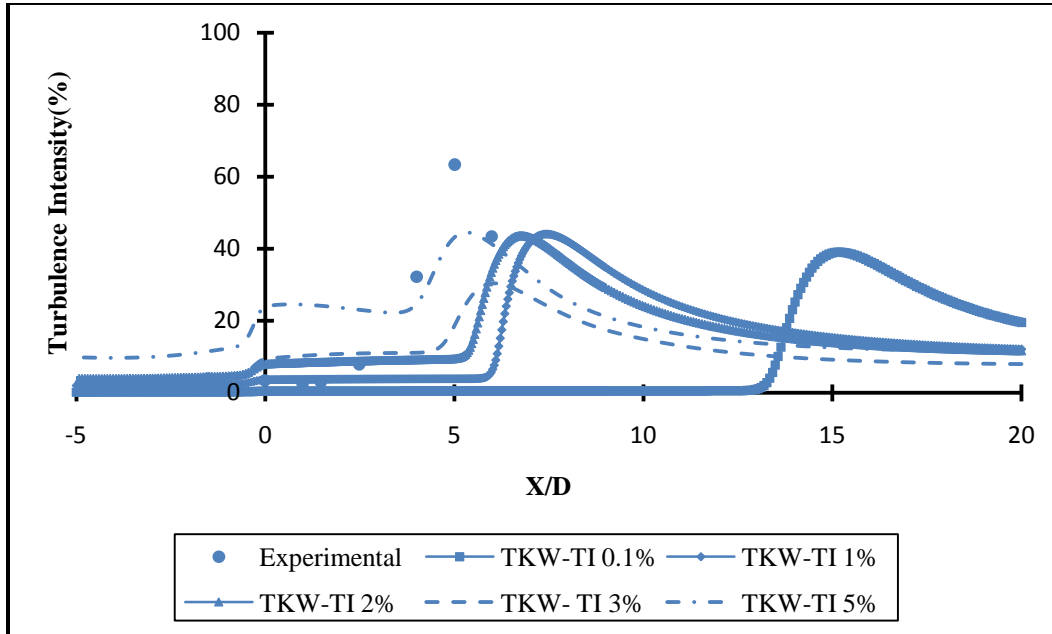


Figure 5.16. Variation of the turbulence intensity for transitional $k-\omega$ turbulence model under inlet-specified turbulence intensity.

It is interesting to make an analogy between Figures 5.15 and 5.16 because it is useful for predicting the location of transition to turbulence. For example, a drop in the axial centerline velocity for the 2% turbulence intensity is reported somewhere in the region $5 < \bar{X} < 6$, as shown in Figure 5.15, and this is the same location where a corresponding jump in turbulence intensity is observed in Figure 5.16. Therefore, this is the location where the flow field undergoes a transition to turbulence and is verified in Figures 5.15 and 5.16.

5.5 Validation Studies

5.5.1 Grid Independence

Once it was shown that the transitional variant of the $k-\omega$ turbulence model produces far superior results than the standard $k-\omega$ model, then the next step was to establish a grid

independent study to check the validity of the current simulations to ensure whether or not any further improvement would be possible by considering a more dense grid in this process. For the grid independence study, it was strictly ensured that the independent flow parameters, such as equiangle skew (Q_{EAS}) and aspect ratio, were well within the established practice for the CFD simulations, as discussed in Chapter 3.

The grid independence study was carried out on three different sets of grids: G1, G2, and G3. Of these, grid G1 was composed of a number of grid points concentrated near the wall rather than using the boundary layer, while grids G2 and G3 utilized boundary layer capabilities. Two parameters were considered of paramount importance for the grid validation: recirculation length and wall $y+$. The grid configuration is shown in Table 5.1.

TABLE 5.1

GRID CONFIGURATION FOR GRID INDEPENDENCE STUDY

Grid	Number of Cells
G1	572,000
G2	707,200
G3	1,624,832

Figure 5.17 shows the plot of the non-dimensional wall shear stress for grids G1, G2, and G3, which is non-dimensionalized by the upstream value of the wall shear stress. The wall shear stress value was almost identical for all three grids, with the maximum value occurring at the throat of the stenosis and a negative wall shear stress being observed up to a few diameters downstream of the stenosis. Reattachment length is defined as the length between the two points where the flow detaches from the wall as a result of the adverse pressure gradient to the point where the flow reattaches to the wall by changing the wall shear stress sign from negative to positive, i.e., favorable pressure gradient.

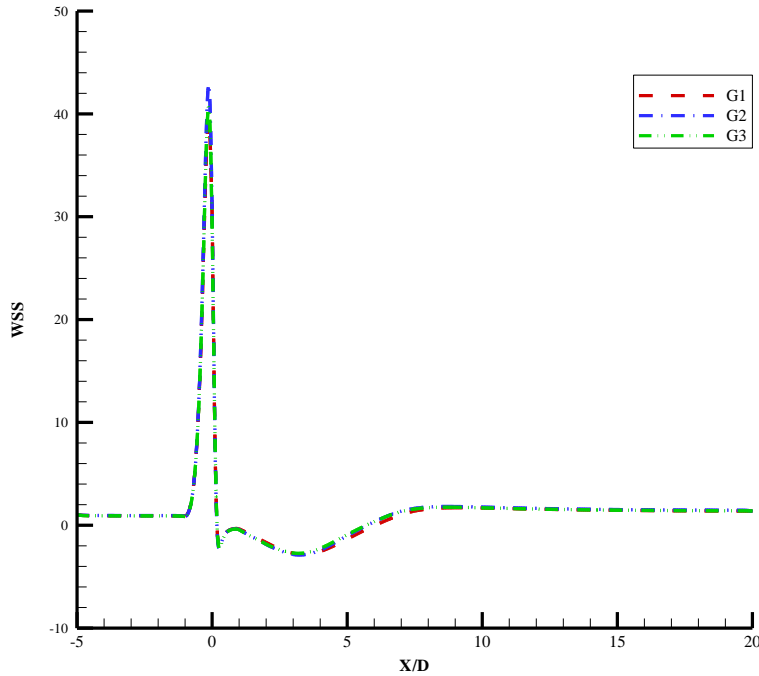


Figure 5.17. Non-dimensional wall shear stress value for grids G1, G2, and G3.

Figure 5.18 shows the zoom-in region from Figure 5.17 where the flow reattaches for the recirculation length study. Table 5.2 shows the percentage difference between the reattachment lengths for grids G1, G2, and G3. Considering grid G3 as a baseline grid, the percent difference in recirculation length was measured. The difference between all three grids was minimal, but grids G2 and G3 were preferred for further simulations. The recirculation length study from Figure 5.18 clearly indicates that for grid G1, the flow reattaches at $\bar{X} = 6.05$, while for grids G2 and G3, the flow reattaches at $\bar{X} = 5.8$ and 5.77 , respectively, measured from the throat of the stenosis. Therefore, grids G2 and G3 are in excellent agreement with the experimental data, since the experimental data suggest that the flow reattaches somewhere in the region of $5 < \bar{X} < 6$, measured from the throat of the stenosis.

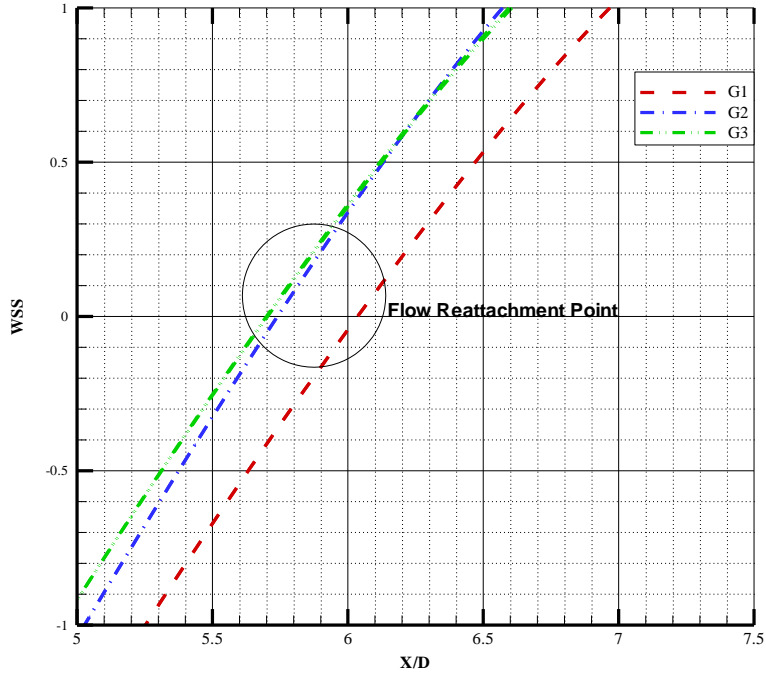


Figure 5.18. Zoom-in regions for grids G1, G2, and G3 for flow reattachment study.

TABLE 5.2

RECIRCULATION LENGTH FOR GRIDS G1, G2, AND G3

Grid	Recirculation Length	% difference
G1	5.8525	4.47
G2	5.6035	0.026
G3	5.6020	0

Figure 5.19 shows the variation of wall y^+ for grids G1, G2, and G3. As can be seen, grid G1 produces wall y^+ at nearly 1.6, while the other two grids, which utilize boundary-layer capabilities, produce this wall y^+ around 0.35 and 0.15, respectively. Since the ultimate goal was to achieve a wall y^+ less than 1, it is evident that grids G2 and G3 provide the most promising results. Therefore, recirculation length and wall y^+ confirm that the difference

between grids G2 and G3 is negligible and that grid G2 is favored for all subsequent calculations in order to save computational time.

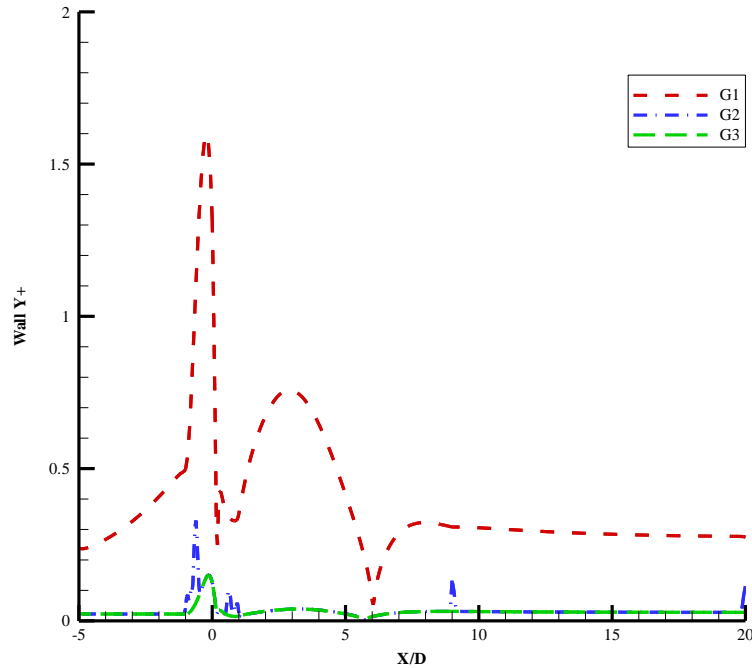


Figure 5.19. Wall y^+ comparisons for grid G1, G2 and G3.

5.5.2 Steady-State Simulation vs Transient-State Simulation

For the current work, a fully developed Poiseuille flow was imposed at the inlet, with a maximum centerline velocity corresponding to Reynolds numbers of 500 and 1000. For an upstream Reynolds number of 500, the flow remained laminar in the post-stenotic region, and transition to the turbulence was not observed (not shown here). However, for an upstream Reynolds number of 1000, the flow was in the process of transition to the turbulence much earlier than the prescribed range for the smooth pipe flow, i.e., $Re_{cr} = 2300$. Therefore, instabilities do exist distal to the stenosis at a Reynolds number of 1000 corresponds to the centerline of the tube due to the local constriction in the form of stenosis. However, that issue was reflected during the solution procedure since convergence issues were associated with the transitional $k - \omega$ model when the turbulence intensities of 0.1% and 1% were specified at the

inlet boundary condition. Therefore, a time-dependent steady-state approach was used to overcome the convergence issue, considering the fact that the instabilities were time-dependent in nature.

Here, a systematic study was carried out by considering a transient flow and steady-state flow option available in the finite volume solver FLUENT. As discussed in Chapter 4, the semi-implicit method for pressure-linked equations-consistent (SIMPLEC) algorithm was used for the steady flow, while the pressure implicit with splitting of operators (PISO) algorithm was used for unsteady or time-dependent flow. For the sake of comparison, the simulations were carried out with the same boundary conditions by considering the steady-state and transient-state options available in FLUENT. A 20-second cycle was used for transient calculations, with a time-step size (Δt) of $1e-3$, which requires 20,000 iterations to complete. A detailed calculation is shown in the appendix.

Figures 5.20 and 5.21 show the axial variation of the centerline velocity along the non-dimensional axial distance and the variation of turbulence intensity over the same for 2% turbulence intensity, respectively. The results of both approaches—transient approach by enforcing the time-step size and the steady-state approach—are identical to each other. Similar observations were found for turbulence intensities of 3% and 5%. However, they are not shown here. It is worthwhile to note that the time-dependent steady-state simulation is superior for turbulence intensities of 0.1% and 1%, since it provides better convergence than the steady-state simulation with the same boundary conditions, which does not have the feasibility of providing a time-step size. Therefore, comparison of turbulence intensities of 0.1% and 1% are not shown here, since the solution was unable to converge for these two cases under the steady-state simulations. From here forward, a time-dependent steady-state reference will be used for the

steady-state simulations when they are treated as transient or unsteady flow by providing the time-step size.

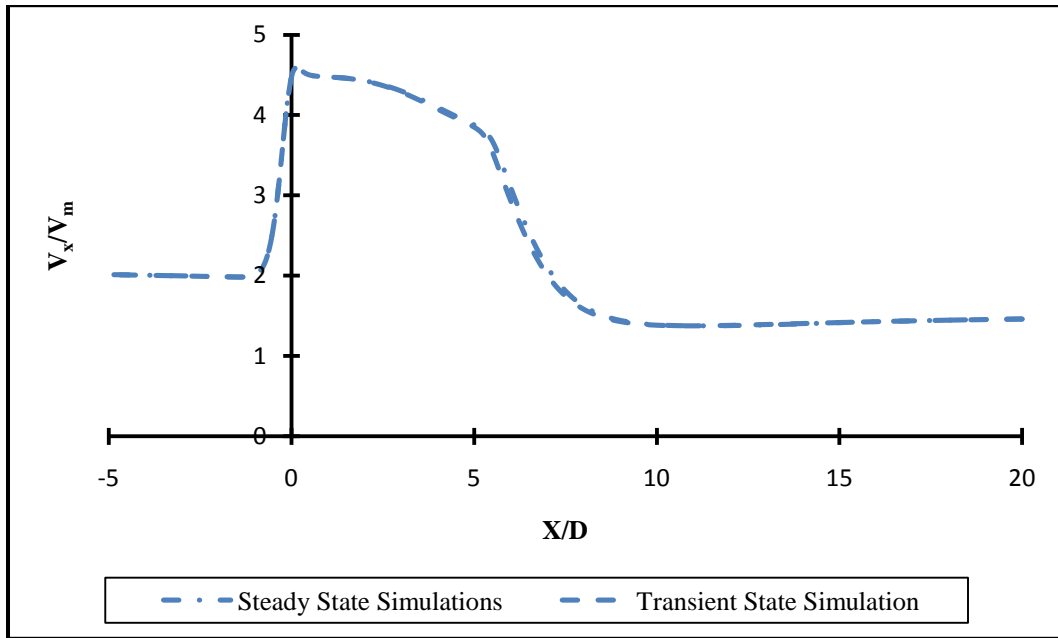


Figure 5.20. Axial variation of centerline velocity for 75% area reduction at $Re = 1000$.

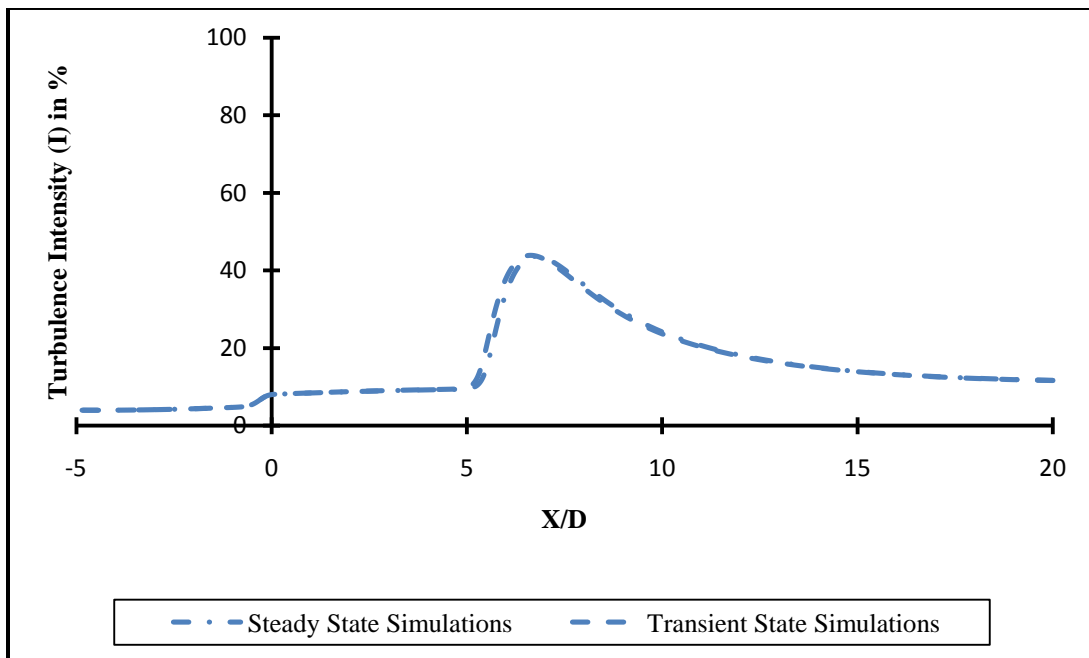


Figure 5.21. Variation of turbulence intensity (I) along centerline velocity for 75% area reduction at $Re = 1000$.

It is worth noting that the time-dependent steady-state approach was quite time consuming and required substantial computational resources compared to the steady-state simulations. It is good practice to consider a time dependant flow if convergence issues arise.

5.5.3 Effect of Time-Step Size

Two different time-step sizes, i.e., $\Delta t = 0.01$ and 0.001 , were provided for the numerical studies. Recirculation length was considered in order to examine the effect of time-step size on overall flow field. No differences were observed in the recirculation length by decreasing the time-step size from 0.01 to 0.001 , as shown in Figure 5.22. Furthermore, Figure 5.23 shows that the amounts of turbulence intensity predicted by both sizes of time steps are identical to each other. However, to be conservative, the current computational work used a time-step size of 0.001 , which came with increased computational cost.

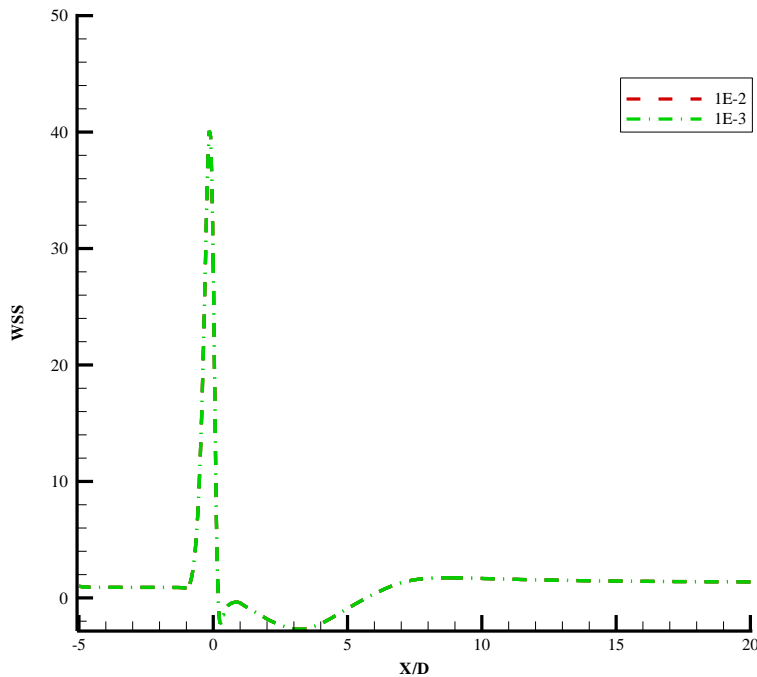


Figure 5.22. Comparison of wall shear stress using time-step sizes 0.01 and 0.001 .

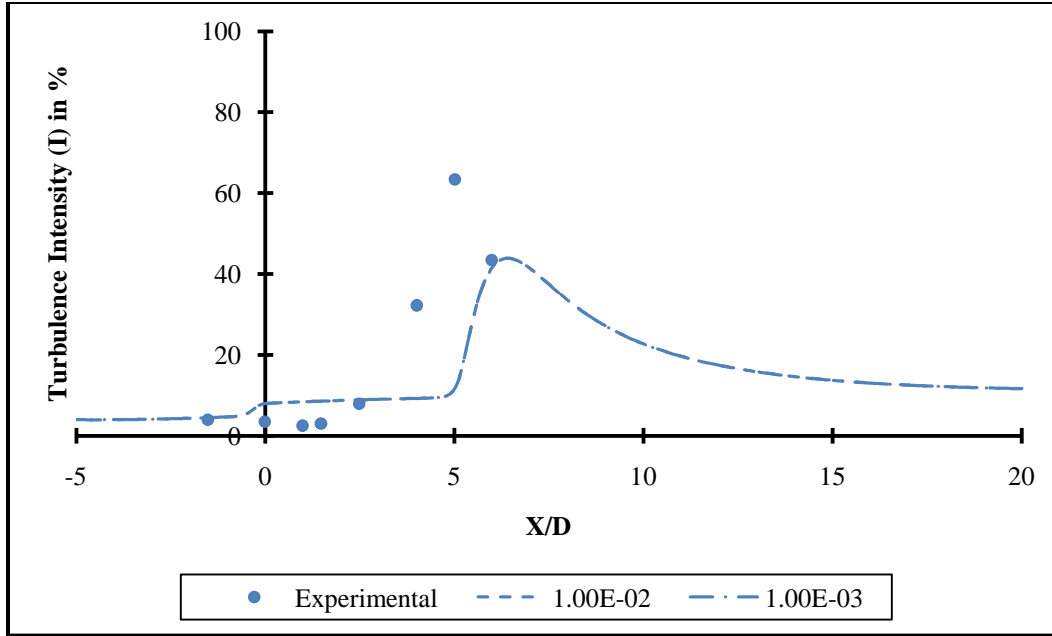


Figure 5.23. Comparison of turbulence intensity along centerline of vessel at time-step sizes 0.01 and 0.001.

5.5.4 Effect of Flow Cycle on the Solution

The effect of flow cycle on the solution was investigated using 20-second, 40-second, and 60-second time cycles. It was found that flow resembles the same behavior throughout the cycles, since no differences were observed for the recirculation study and the non-dimensional velocity profile study. Figure 5.24 shows a comparison of the wall shear stress distributions during $T = 20$, 40, and 60 seconds per cycle. The maximum non-dimensional wall shear stress value reported at $T = 20$ seconds was 40.30, while this value reported at $T = 40$ and 60 seconds was 40.10. Therefore, the difference in wall shear stress at $T = 20$, 40, and 60 seconds was negligible. Figure 5.25 shows the zoom-in region for the maximum wall shear stress for $T = 20$, 40, and 60 seconds near the throat of the stenosis.

Furthermore, Figures 5.26 and 5.27 show the comparisons of selected axial locations corresponding to $T = 20$, 40, and 60 seconds, and they all indicate excellent agreement.

Therefore, the 20-second time period was used for further analysis in order to reduce computational efforts. From here forward, only the recirculation length study was used to evaluate the effect of the other parameters.

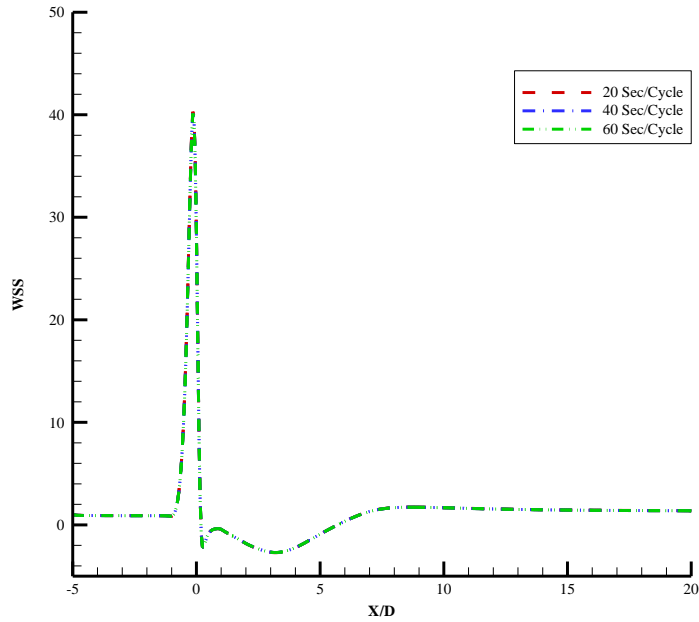


Figure 5.24. Distribution of wall shear stress corresponding to 20-second, 40-second, and 60-second time cycles.

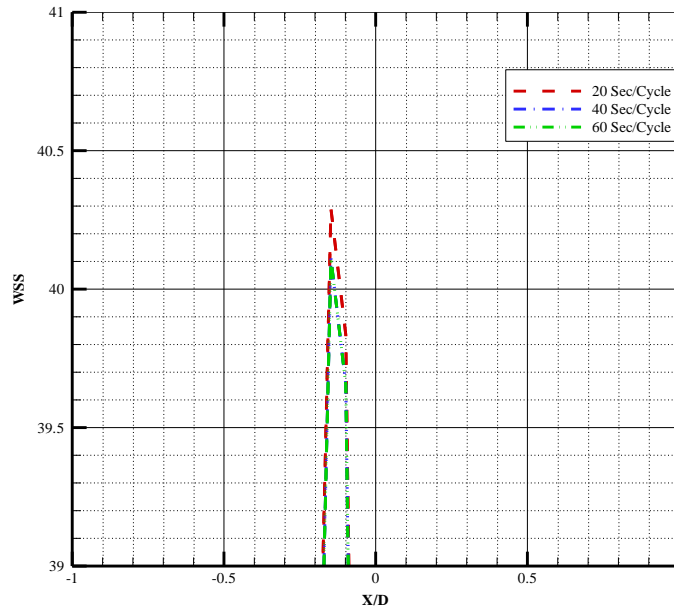


Figure 5.25 Maximum wall shear stress distributions near throat of stenosis corresponding to 20-second, 40-second, and 60-second time cycles.

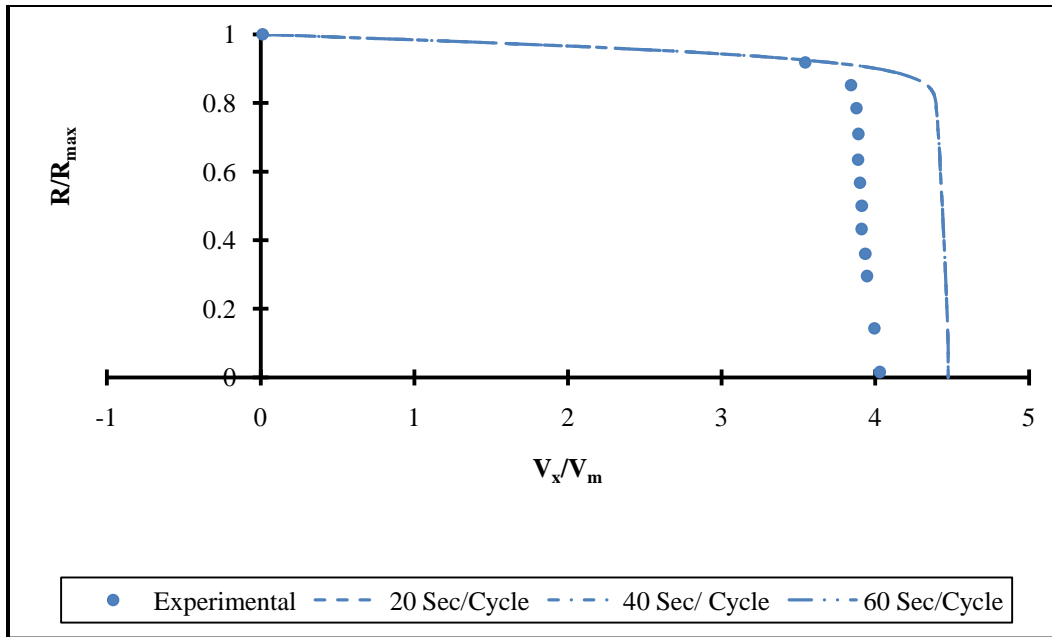


Figure 5.26. Axial velocity profiles at $\bar{X} = 0$.

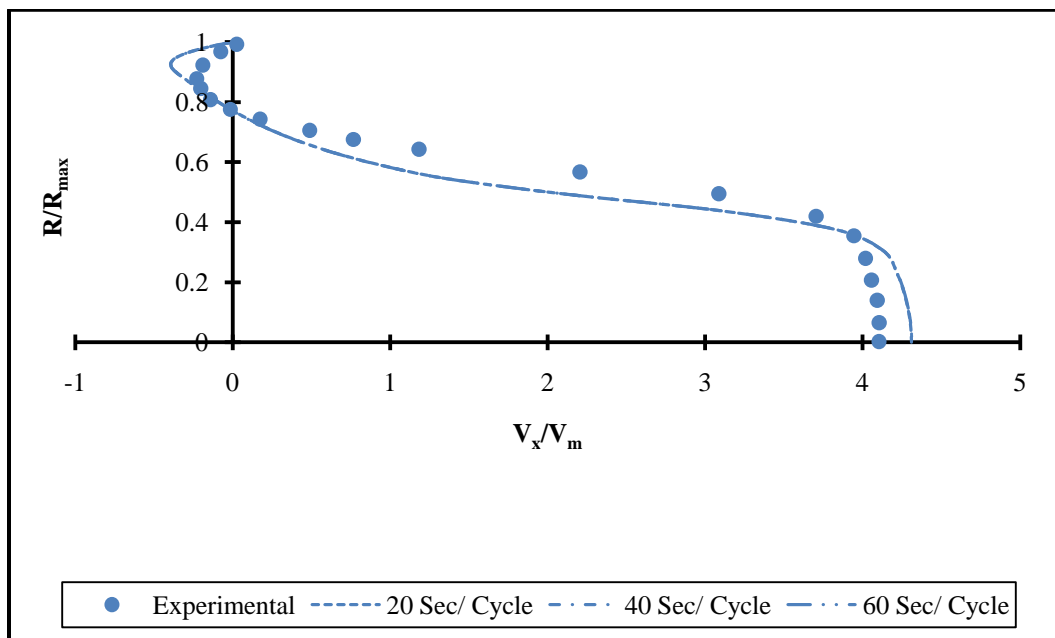


Figure 5.27. Axial velocity profiles at $\bar{X} = 2.5$.

5.5.5 Influence of Inlet and Outlet Lengths

Table 5.3 shows the influence of three different inlet and outlet cases on the recirculation length: 8D inlet length and 20D outlet, 4D inlet length and 20D outlet, and 4D inlet length and

24D outlet. It can be seen clearly from the data that extending the upstream length from 4D to 8D decreases the recirculation length significantly. The shortest recirculation length was observed for the combination of the 8D inlet length and 20D outlet length, while the 4D inlet length and 24D outlet length provided the maximum recirculation length, i.e., 5.7480. For all three cases under investigation, the flow separates just downstream of the stenosis at $\bar{X} = 0.1820$ and reattaches at $\bar{X} = 5.05$, 5.3850, and 5.93, respectively. From experimental observation, the flow is expected to reattach somewhere in the region of $5 < \bar{X} < 6$; therefore, all three cases are in good agreement with the experimental work. The effect of the entrance length is neglected since a fully developed Poiseuille solution was imposed at the inlet; therefore, a 4D inlet length in combination with a 20D outlet length was considered appropriate for the current study, which saved computational resources, compared to the other two cases where the inlet and outlet lengths were extended up to 4 diameters, respectively.

TABLE 5.3

EFFECT OF INLET AND OUTLET LENGTHS ON RECIRCULATION LENGTH

Inlet Length (L_i)	Outlet length (L_o)	Recirculation Length (L_r)
8D	20D	4.8680
4D	20D	5.5650
4D	24D	5.7480

5.6 Contour Plots

Figures 5.28 and 5.29 show the contour plots for streamlines and turbulent kinetic energy under inlet-specified turbulence intensities of 0.1%, 1%, 2%, 3%, and 5% for the transitional $k - \omega$ model at $Re = 1000$.

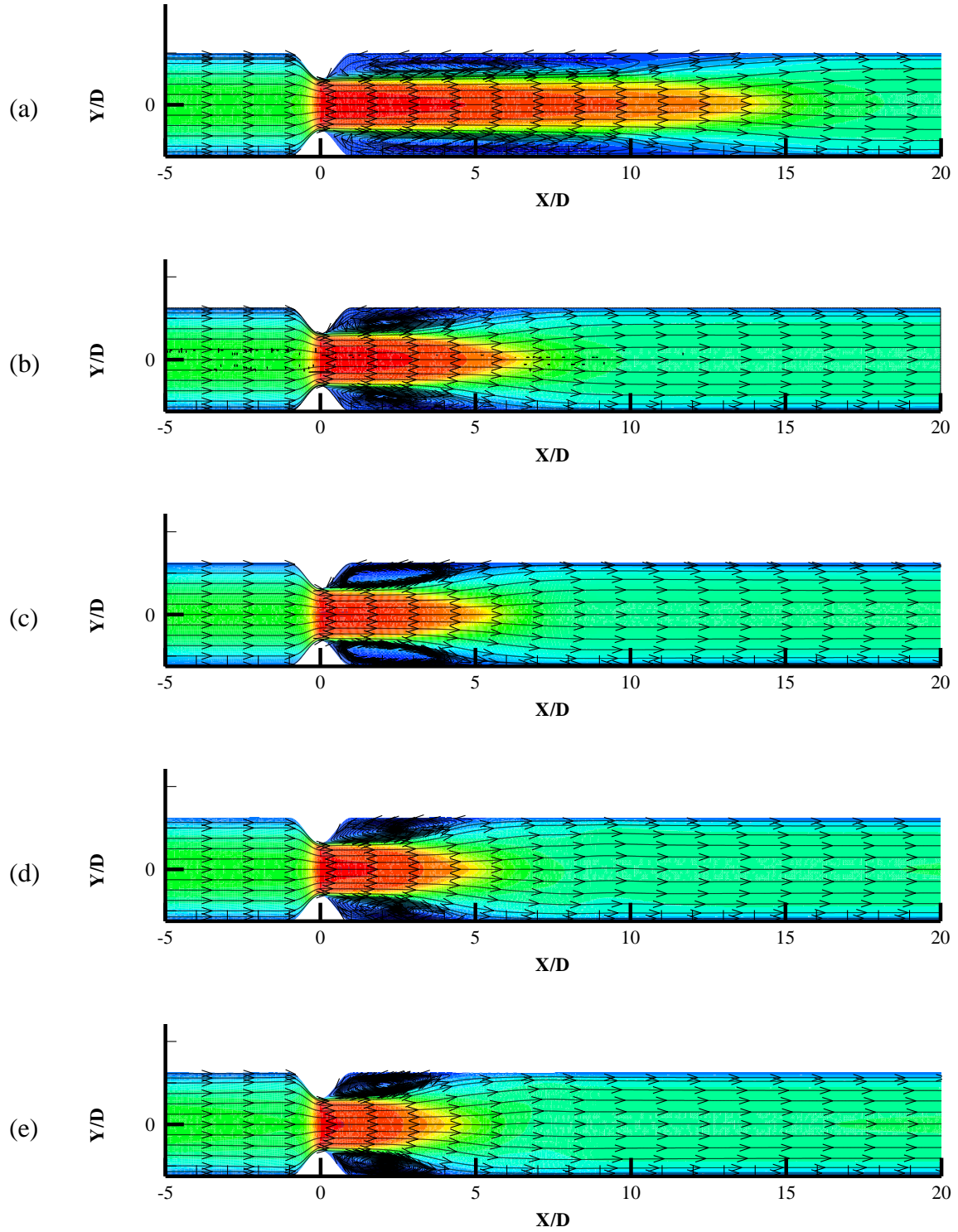


Figure 5.28. Contours of streamlines for transitional $k-\omega$ turbulence model with turbulence intensities of (a) 0.1% , (b) 1% , (c) 2% , (d) 3% , and (e) 5% at $Re = 1000$ for 75% area reduction.

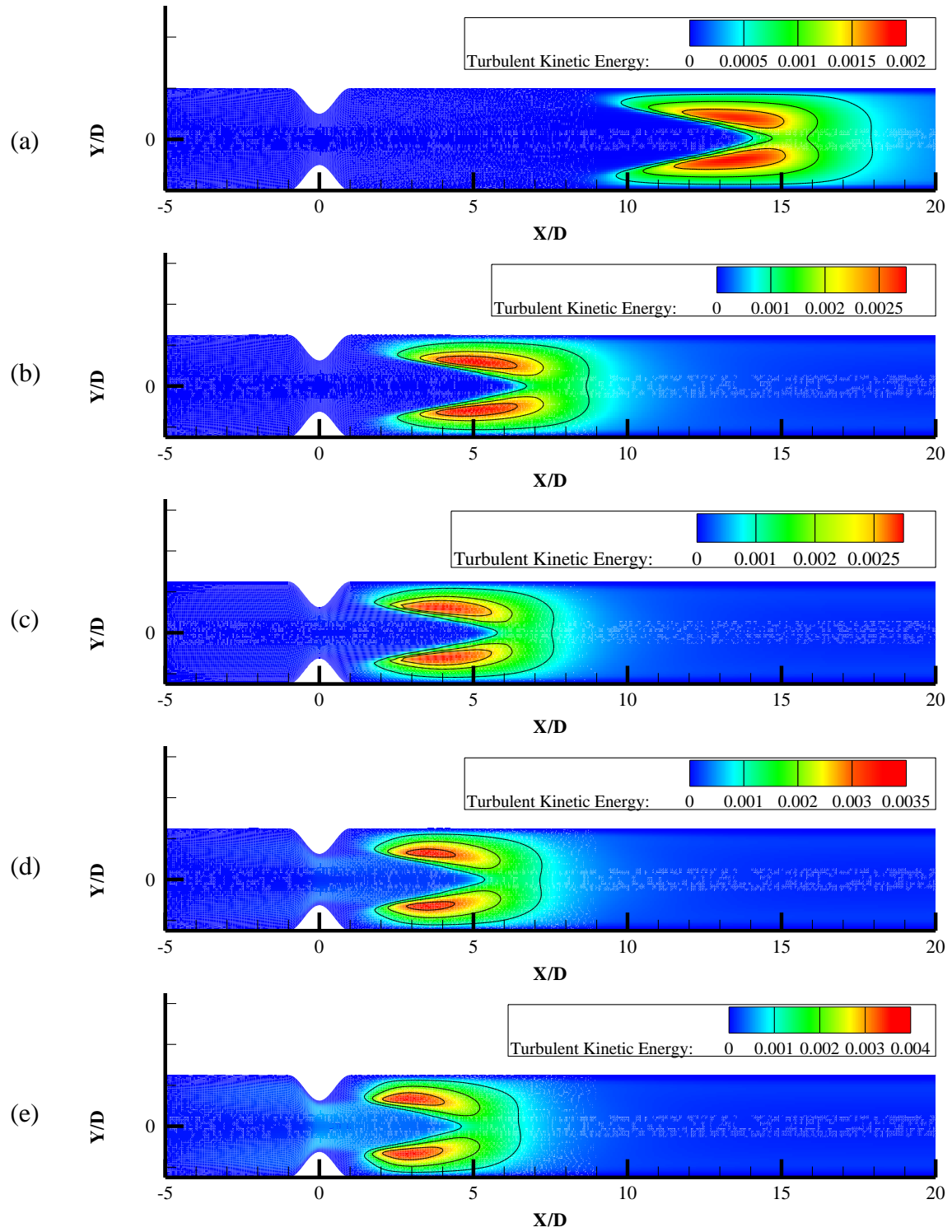


Figure 5.29. Contours of turbulence kinetic energy for transitional $k-\omega$ turbulence model with turbulence intensities of (a) 0.1% , (b) 1% , (c) 2% , (d) 3% , and (e) 5% at $Re = 1000$ for 75% area reduction.

CHAPTER 6

PULSATILE-FLOW SIMULATIONS

6.1 Introduction

It is of paramount importance to simulate the pulsatile nature of blood flow. This chapter shows that efforts were made to investigate the effect of blood flow pulsatility and its effect on the flow dynamics in the vicinity of the stenosis. The same geometrical configuration was used for the pulsatile-flow study as for the steady-state analyses, with a variation in vessel diameter, which is considered 6 mm for pulsatile-flow simulations. All other flow parameters were considered the same as used in the steady-state simulations, except a pulsatile waveform was imposed at the inlet boundary condition. For the current simulation, a pulsatile sinusoidal waveform was provided and is represented by equation (6.1) and depicted in Figure 6.1. The velocity is plotted against the non-dimensional time $\frac{t}{T}$. A cycle of 0.4 second was used for the analysis, which is similar to that used by Dietiker and Hoffmann [29].

$$U(t) = 0.25 \left[1 + \sin \left(2\pi \frac{t}{T} \right) \right] \quad (6.1)$$

The waveform in Figure 6.1 can be divided into four different phases: early systole, peak systole, mid-deceleration, and end-deceleration. Early systole corresponds to $\frac{t}{T} = 0$ in Figure 6.1. Then it undergoes the acceleration phase and attains peak velocity at $\frac{t}{T} = 0.25$. Hence, it is referred to as peak systole. Flow enters the deceleration phase, a representation of the diastolic flow condition in the circulatory system, and is depicted by $\frac{t}{T} = 0.50$ and 0.75 , which correspond to the mid-deceleration and end-deceleration phases, respectively. The maximum Reynolds

number of 800 corresponds to the peak systole phase, and the minimum Reynolds number of 200 corresponds to the end-deceleration phase, with the Womersley parameter being 6.1.

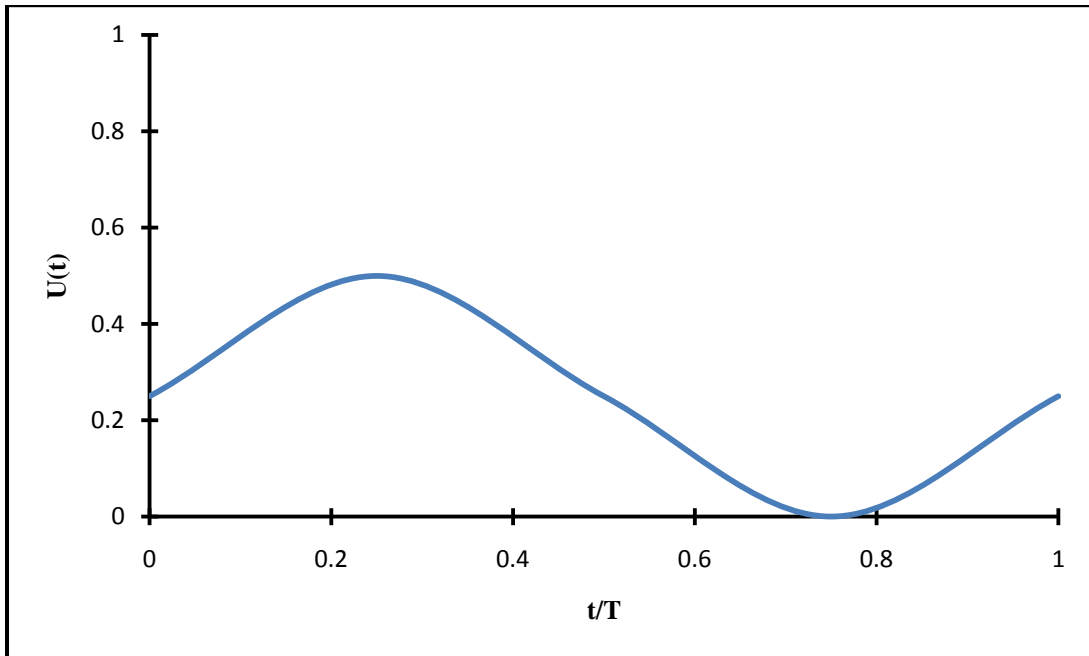


Figure 6.1. Inlet pulsatile waveform plotted against non-dimensional time $\frac{t}{T}$.

A non-dimensional Womersley parameter is a measure of the unsteadiness that arises due to the pulsatile or oscillatory nature of the blood flow, also referred to as an unsteady Reynolds number, and is represented by α . It corresponds to the ratio of the viscous forces to the inertial forces [12]:

$$\alpha = \frac{D}{2} \sqrt{\frac{\omega \rho}{\mu}} \quad (6.2)$$

If $\alpha < 1$, then viscous forces dominate over the inertial forces; hence, flow can be accurately represented by the Poiseuille flow for the pipe flow. If $\alpha > 1$, inertia dominates over the viscous forces; therefore, the driving pressure gradient lags 90 degrees behind the flow field, and the velocity profile is flat, in contrast to the parabolic flow where the pressure gradient is in phase with the centerline velocity [12]. The Womersley parameter is a strong function of the

vessel diameter, since the rest of the flow properties are constant relative to the circulatory system.

In this chapter, the effect of the increasing constriction ratio on the overall flow and wall shear stress during systolic and diastolic flow cycles and the relevance of this from a clinical point of view will be discussed. In addition, a transitional variant of the $k-\omega$ model is used with an inlet-specified turbulence intensity of 1%, and the possible transition of the turbulence depending on the local flow structure is discussed.

6.2 Non-Dimensionalization

For pulsatile-flow simulations, the centerline velocity is not constant with the maximum during peak systole pressure, i.e., from highest of 0.50 ms^{-1} to lowest of 0 ms^{-1} which corresponds to the end-deceleration phase. Therefore, the average velocity of one pulse cycle, i.e., 0.25 ms^{-1} was used for the non-dimensionalization. The fluctuations of velocity magnitudes during the course of a cycle result in the oscillating value of the upstream value of wall shear stress corresponding to a different time interval, and therefore, the wall shear stress is not non-dimensionalized in this chapter and expressed by pascal.

6.3 Axial Velocity Profile

Figures 6.2 through 6.7 represent the comparison of non-dimensional axial velocity profile against the non-dimensional radial location at different axial locations, measured from the throat of the stenosis over the time period T for the 75% area reduction case. Figure 6.2 shows the variation of the velocity profile at one diameter upstream of the stenosis over a course of a non-dimensional time period. A nearly flat velocity profile is observed upstream of the stenosis during early systole and continues to accelerate through peak systole, since it behaves similar to a fully developed Poiseuille flow during peak systole where the velocity corresponds to the

centerline velocity, which approaches nearly $1.9U_{avg}$. The magnitude of the centerline velocity started to decrease as the flow began decelerating. With further decrease in the centerline velocity, the adverse pressure gradient was sufficient to cause the flow separation upstream of the stenosis during the end-deceleration phase.

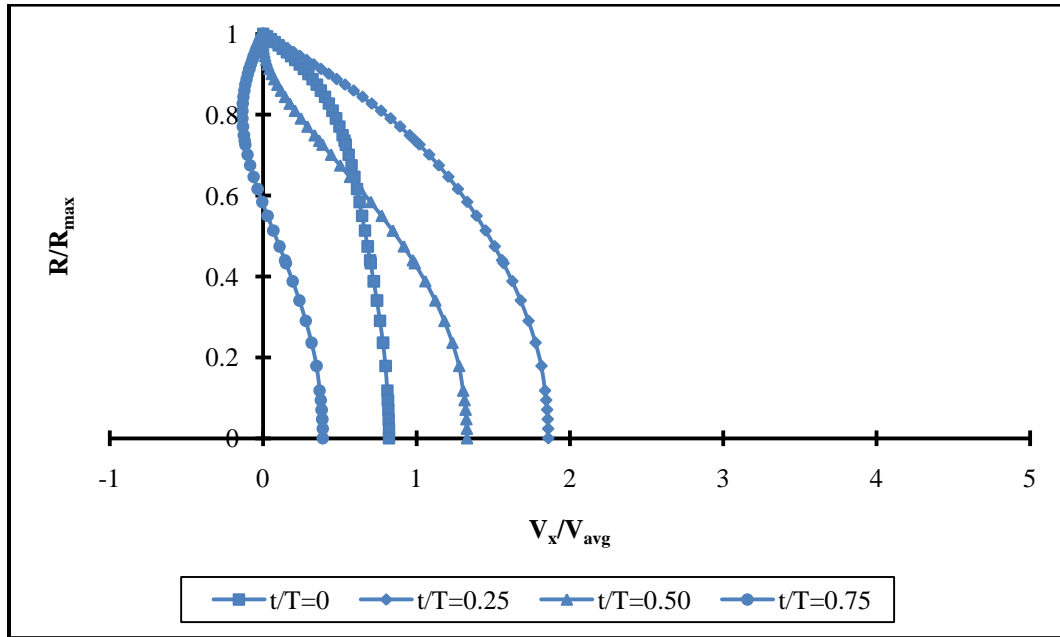


Figure 6.2. Non-dimensional velocity profiles at axial location $\bar{X} = -1$.

When the flow passes through the stenosis, a jet is formed as a result of the area reduction during early systole and continues to gain momentum as it advances towards peak systole, since the velocity exceeds the average velocity of $4.5U_{avg}$. From here onward, flow starts to experience the deceleration and centerline velocity, thus losing momentum. During the end-deceleration phase, flow continued to decelerate further, and a condition was reached whereby there was no inlet flow. This led to a small recirculation region at the throat of the stenosis itself and resulted in detachment of the shear layer from the throat of the stenosis, corresponding to $\frac{t}{T} = 0.75$, as shown in Figure 6.3.

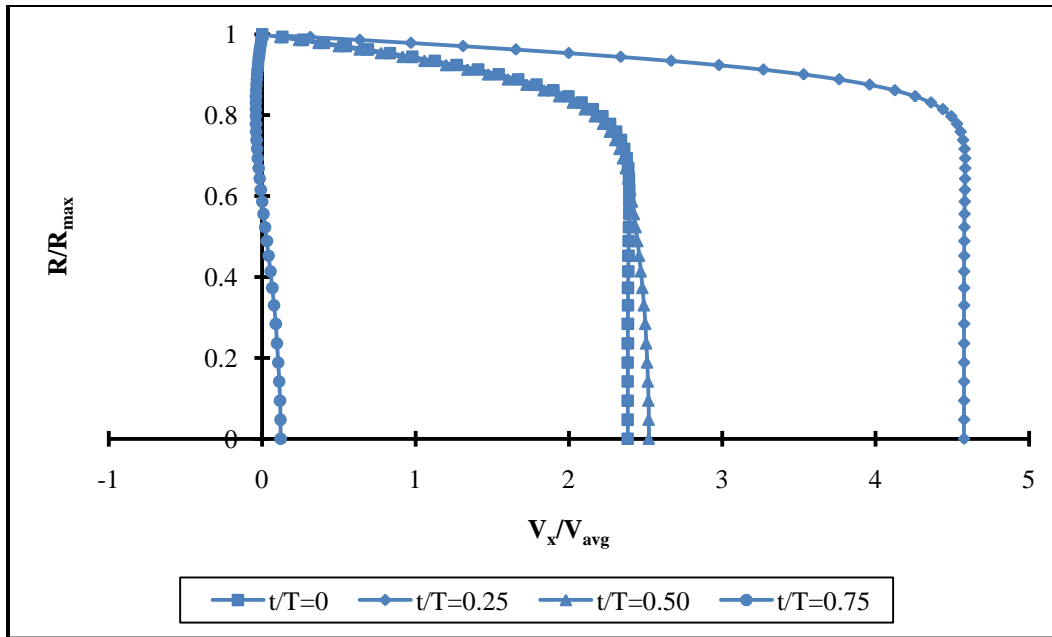


Figure 6.3. Non-dimensional velocity profiles at axial location $\bar{X} = 0$.

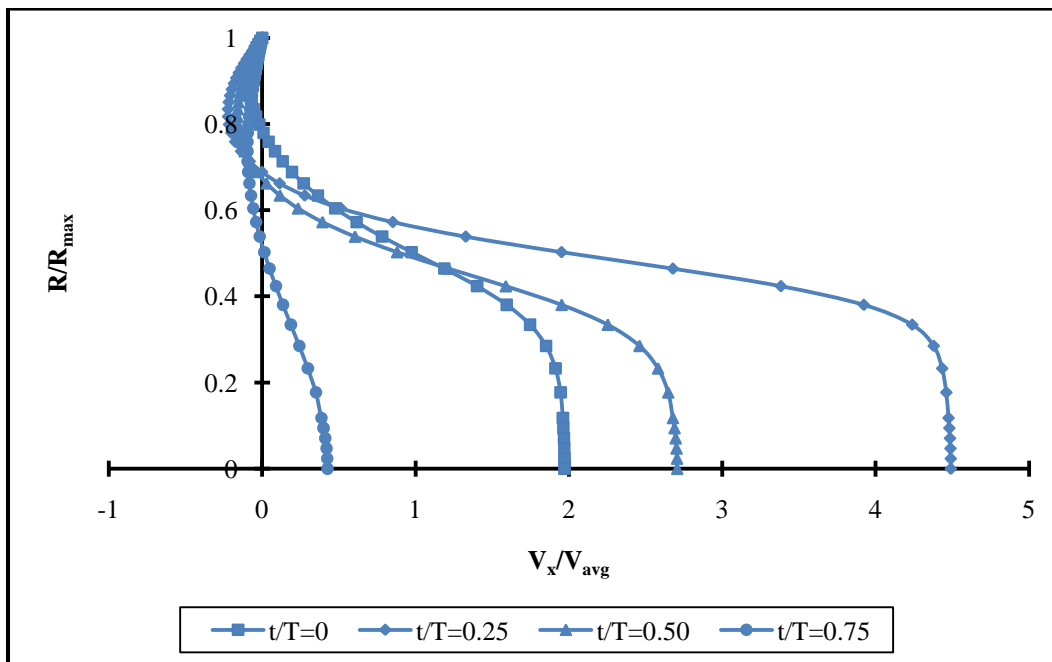


Figure 6.4. Non-dimensional velocity profiles at axial location $\bar{X} = 1$.

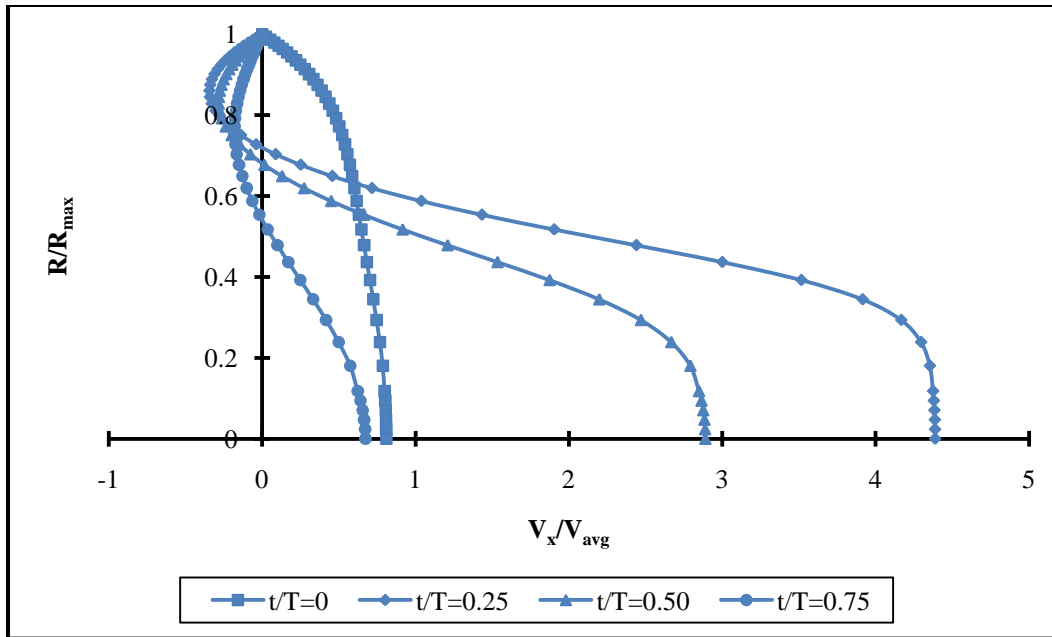


Figure 6.5. Non-dimensional velocity profiles at axial location $\bar{X} = 2$.

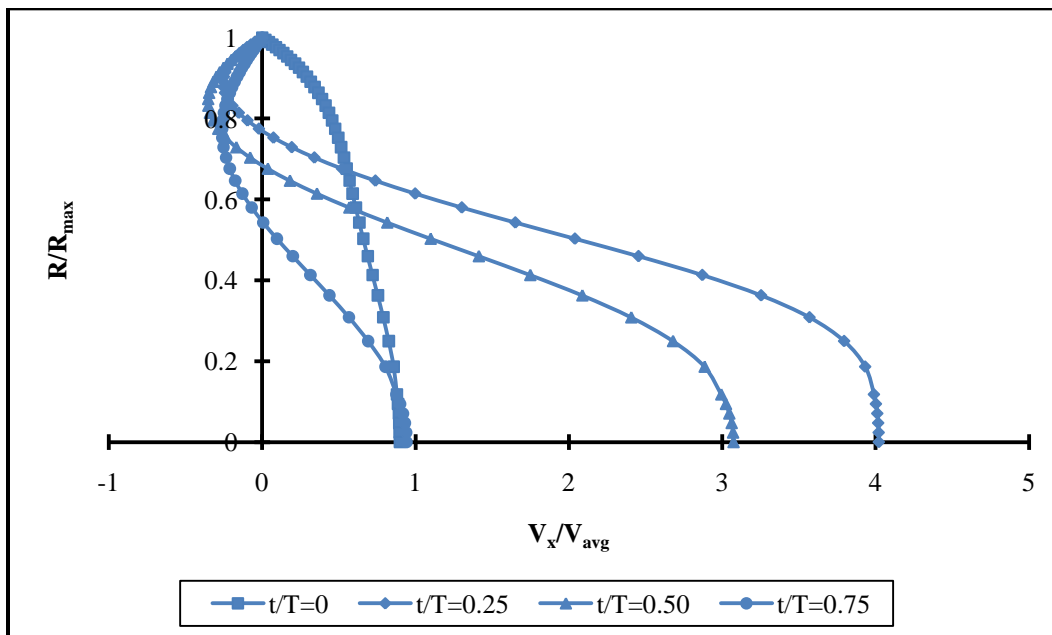


Figure 6.6. Non-dimensional velocity profiles at axial location $\bar{X} = 4$.

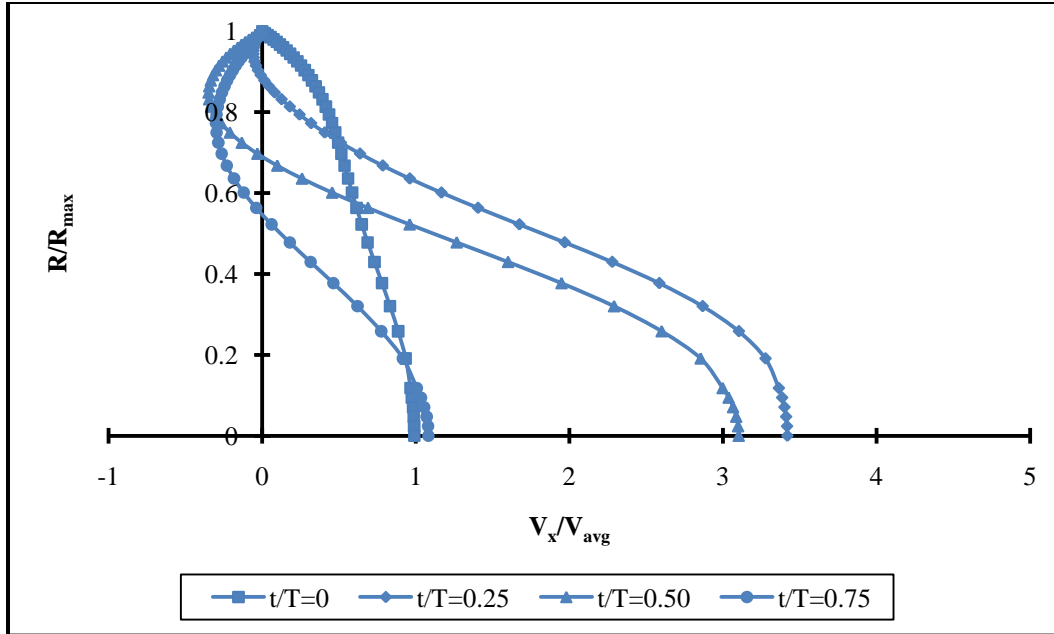


Figure 6.7 Non-dimensional velocity profiles at axial location $\bar{X} = 6$.

It is clear from Figures 6.2 to 6.6 that the shear layer continues to travel further downstream over a course of inlet-specified pulse cycles. The trailing shear layer travels up to 3 diameters downstream of the stenosis during early systole, and extends up to 7 diameters during peak systole (not shown here) and occupies the entire downstream area of the stenosis corresponding to the mid-deceleration and end-deceleration phases. In addition, the flow reattaches at approximately 3 diameters downstream of the stenosis during early systole. The reattachment point moves further downstream during peak systole as the flow accelerates. The flow finally reattaches at approximately 8 diameters distal to the stenosis (not shown here), convects further downstream during the mid- and end-deceleration phases, and is proximal to the stenosis during the end-deceleration phase. Therefore, it is believed that the flow deceleration phase is important for translation of the vortices.

It is obvious from Figures 6.2 to 6.7 that although the centerline velocities, corresponding to the non-dimensional time interval early systole and mid-deceleration phases, are almost

identical to each other, a relatively higher centerline velocity magnitude is observed during the mid-deceleration, compared to early systole where, in fact, the flow is accelerating. This is due to the fact that the former is followed by peak systole while the later is followed by the end of the deceleration phase. Similar trends were observed for the 60% and 90% area reductions. However, they are not shown here.

6.4 Centerline Velocity Comparisons

Figures 6.8 to 6.11 show variations of the axial centerline velocity for 60%, 75%, and 90% area reduction, at non-dimensional time levels 0, 0.25, 0.50, and 0.75, which correspond to early systole, peak systole, and mid-deceleration phase, and end-deceleration phase, respectively.

Figure 6.8 shows the variation of the axial centerline velocity during early systole. It is evident from Figure 6.8 that when flow encounters the throat or minimum cross-sectional area, a substantial increase in the centerline velocity is reported near the throat of the stenosis, with the smallest increase for the 60% area reduction where the centerline velocity increases up to $1.78U_{avg}$, and the largest increase reported for the 90% area reduction, i.e., $5.73U_{avg}$. Therefore, increasing the severity of stenosis from 60% to 90% is accompanied by an increase in the centerline axial velocity, up to a factor of 3.64.

However, as expected, the maximum increase in the peak of the centerline velocity is reported during peak systole near the throat of the stenosis, with the largest value for the 90% area reduction to the smallest value for the 60% area reduction, as shown in Figure 6.9. Again, velocity increases up to a factor of 3.57, with increasing severity of the constriction from 60% to 90%. However, the effect of the jet tends to last longer for all three cases during peak systole compared to early systole, since the effect of the jet diminishes within the few diameters of the stenosis during early systole.

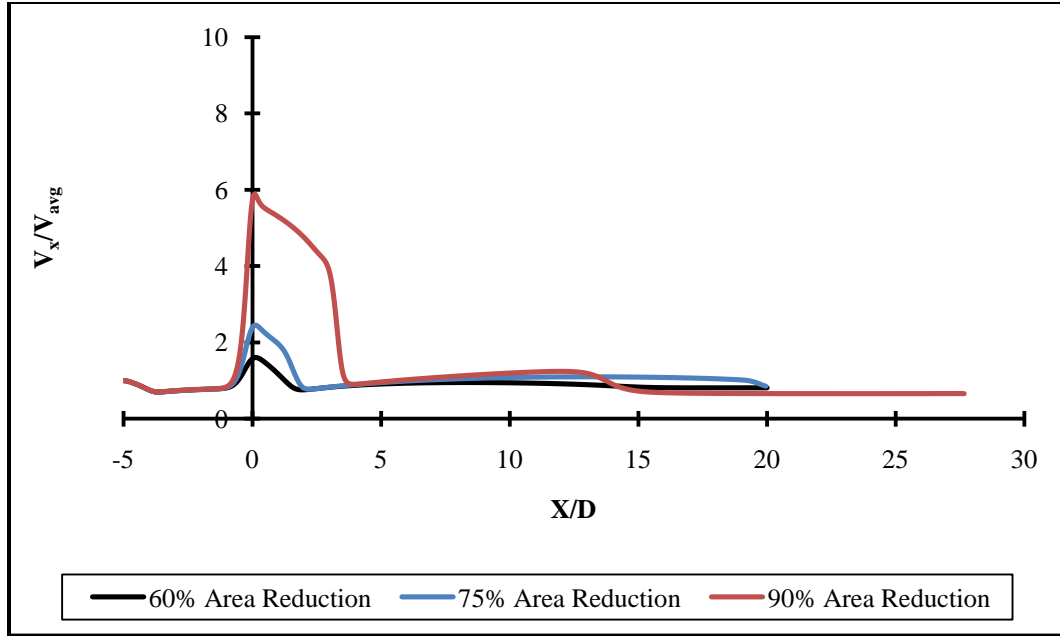


Figure 6.8. Variations of axial centerline velocity for 60%, 75%, and 90% area reductions corresponding to $\frac{t}{T} = 0.0$.

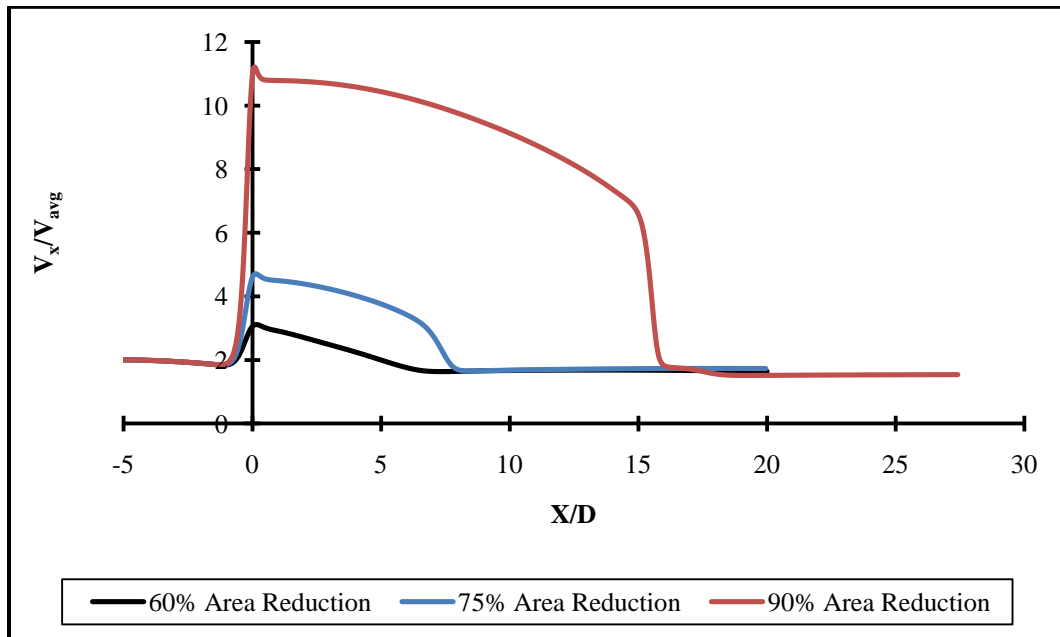


Figure 6.9. Variations of axial centerline velocity for 60%, 75%, and 90% area reductions corresponding to $\frac{t}{T} = 0.25$.

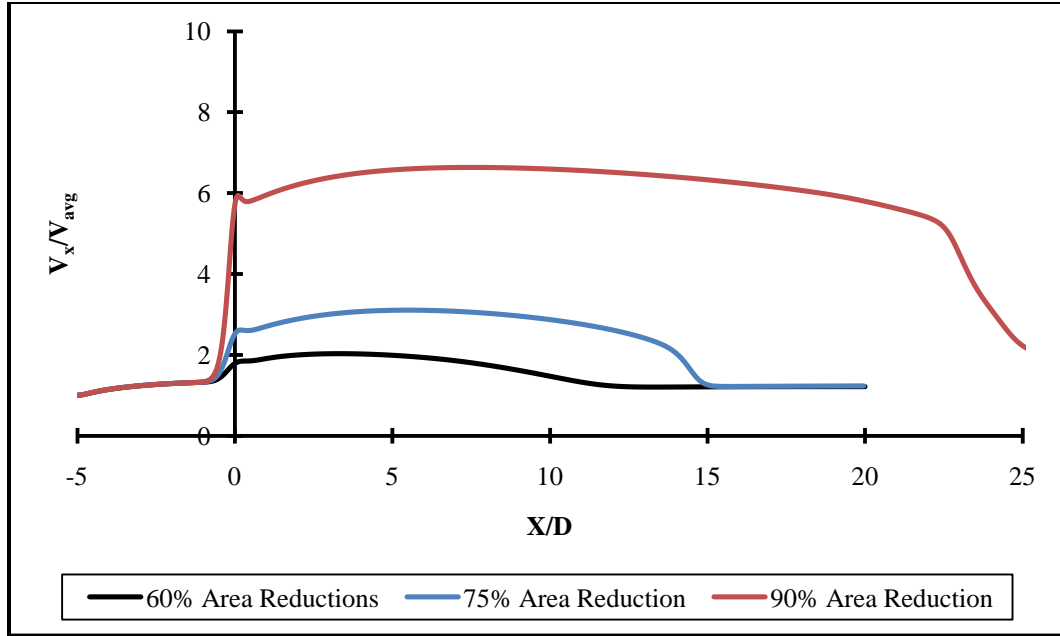


Figure 6.10. Variations of axial centerline velocity for 60%, 75%, and 90% area reductions corresponding to $\frac{t}{T} = 0.50$.

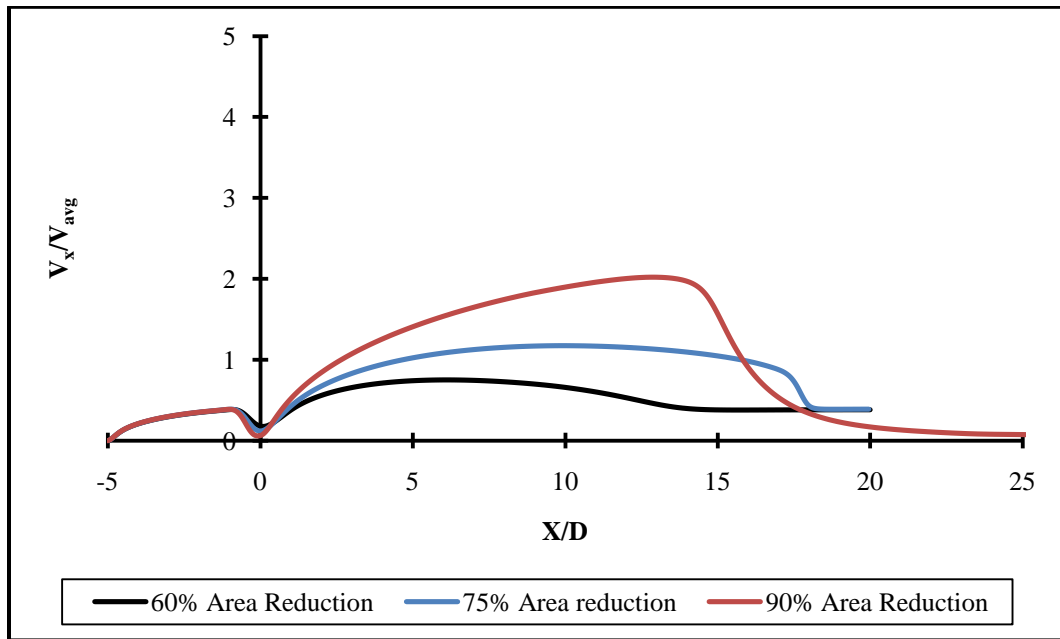


Figure 6.11 Variations of axial centerline velocity for 60%, 75%, and 90% area reductions corresponding to $\frac{t}{T} = 0.75$.

Similar observations were found for the mid-deceleration and end-deceleration phases. Furthermore, increasing the severity of the stenosis from 60% to 90% was accompanied by an approximately 3.5 times higher centerline velocity near the throat of the stenosis for the 90% area reduction. However, an exception to this was the end-deceleration phase where the higher velocity near the throat of the stenosis was observed for the 60% area reduction compared to the 90% area reduction.

In addition, the effect of the jet was sustained longer with the increasing degree of constriction. For example, the effect of the shear layer during peak systole ceases at approximately 6 diameters for the 60% reduction case, 8 diameters for the 75% reduction case, and 16 diameter for the 90% area reduction case, measured from the throat of the stenosis where the centerline velocity recovers from the effect of the jet and reaches the upstream value of the stenosis.

6.5 Wall Shear Stress Comparisons

Figures 6.12 to 6.15 show comparisons of wall shear stress for 60%, 75%, and 90% area reductions at non-dimensional time levels 0, 0.25, 0.50, and 0.75, respectively. It is clear from Figure 6.12 that during early systole, only 90% area reduction exceeds the critically reported value, i.e. $400 \frac{\text{dyne}}{\text{cm}^2}$, that causes damage to the endothelium cell layer [13]. However, this scenario changes considerably during peak systole, where the magnitude of the wall shear stress is much higher for the 75% and 90% area reductions as the velocity reaches peak values. Elevated values of the wall shear stress were found for both cases corresponding to the non-dimensional time of 0.25. Both configurations exceeded the critical value of $400 \frac{\text{dyne}}{\text{cm}^2}$.

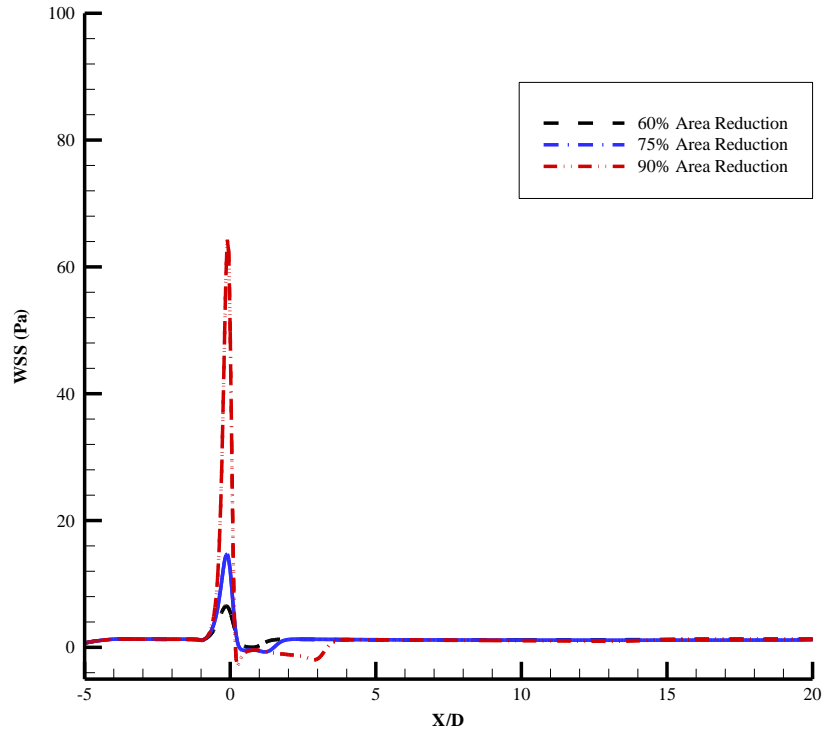


Figure 6.12. Comparisons of wall shear stress at non-dimensional time $\frac{t}{T} = 0.0$.

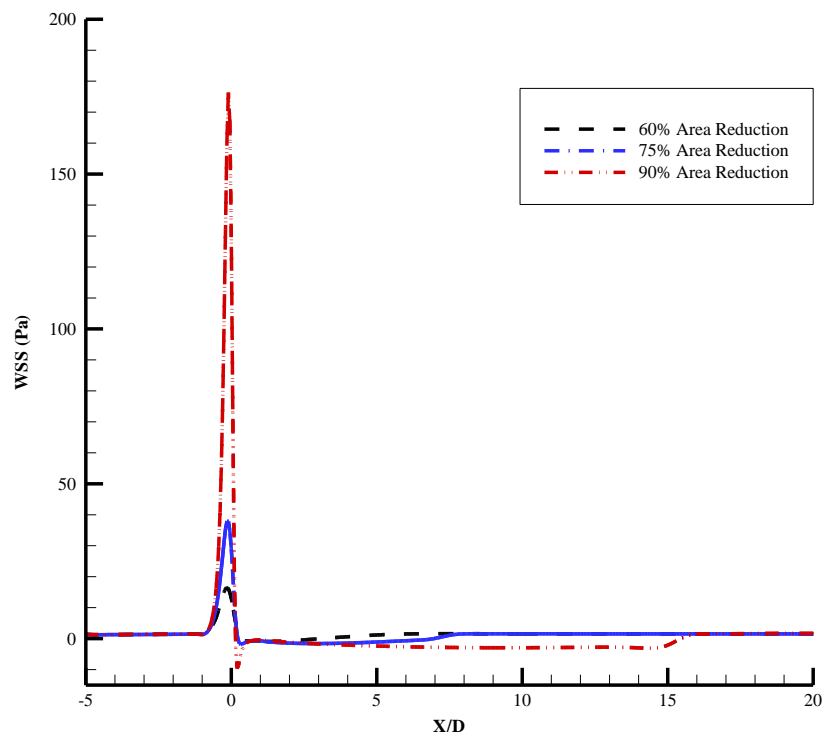


Figure 6.13. Comparisons of wall shear stress at non-dimensional time $\frac{t}{T} = 0.25$.

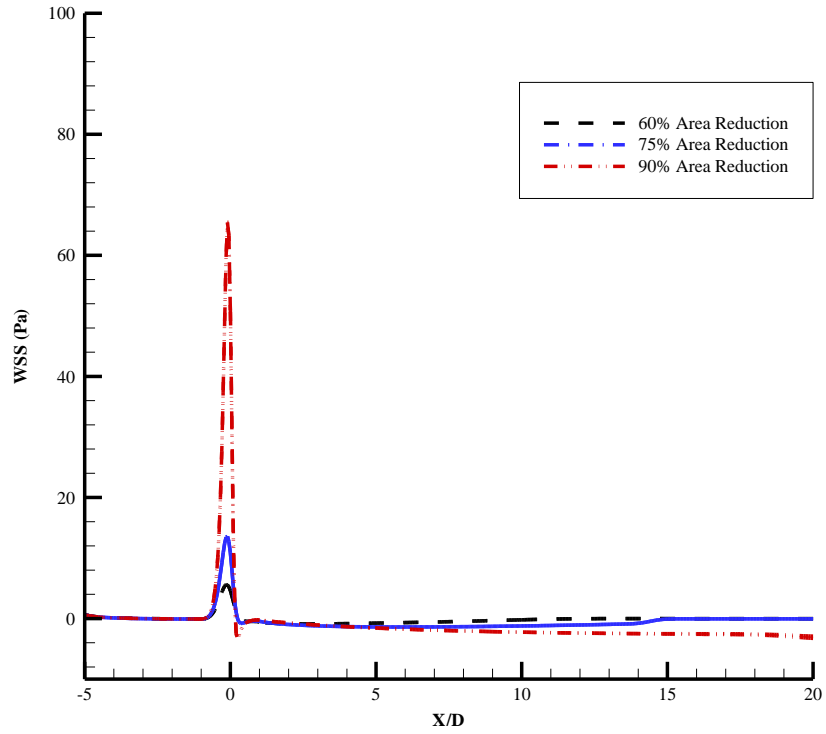


Figure 6.14. Comparisons of wall shear stress at non-dimensional time $\frac{t}{T} = 0.50$.

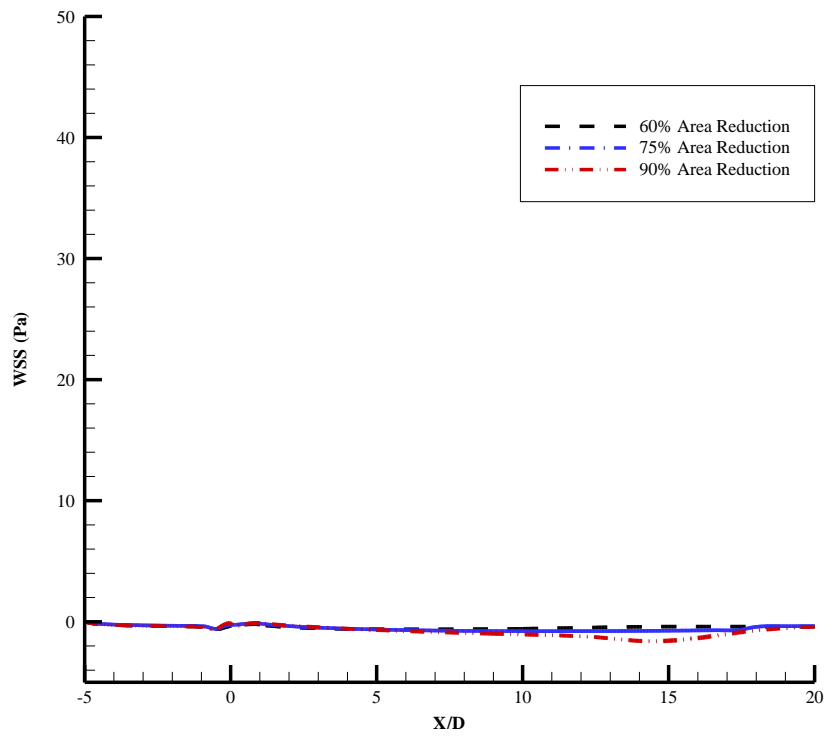


Figure 6.15. Comparisons of wall shear stress at non-dimensional time $\frac{t}{T} = 0.75$.

Figure 6.14 shows the variation of wall shear stress at the non-dimensional time 0.50, which exhibits a similar behavior as that shown in Figure 6.12, since the magnitude of the inlet centerline velocity is identical for both time levels. However, a slight variation in the maximum value of wall shear stress near the throat of the stenosis is observed for both cases when they are compared to each other. An increased value of wall shear stress is reported for the non-dimensional time level 0.50, compared to early systole, i.e., non-dimensional time level 0. Although the difference is minor, it is still noticeable. This is because early systole is followed by the end-deceleration phase, while the mid-deceleration phase is followed by peak systole; therefore, the higher velocity is observed during the mid-deceleration phase. In addition, a large difference is noticed between Figures 6.12 and 6.14 in terms of the reattachment point. The flow-separation region occupies the entire area downstream of the stenosis, since it fails to reattach during the mid-deceleration phase, as shown in Figure 6.14, while reattachment of the flow is established within the few diameters downstream of the stenosis during 60%, 75%, and 90% area reductions for the inlet-specified turbulence intensity of 1% during early systole phase. However, the location of the reattachment point is dependent upon the degree of severity. This is due to the fact that the flow experiences acceleration during early systole as it advances towards peak systole, while it follows deceleration during the mid-deceleration phase as it advances to reach the minimum inlet-flow conditions.

For the non-dimensional time 0.75, a negative wall shear stress was observed for all three cases under investigation; these are shown in Figure 6.15. By increasing the severity of the stenosis from 60% to 90%, the separation point moves further upstream, while the reattachment point moves further downstream of the stenosis, regardless of time level. As expected, the maximum value of the wall shear stress was observed near the throat of the stenosis in all cases.

It would be more interesting to correlate the magnitude of the wall shear stress from a clinical point of view. Malik et al. [44] reported that the normal artery is exposed to a range of wall shear stress from $10\text{--}70 \frac{\text{dyne}}{\text{cm}^2}$. Arterial sites subjected to wall shear stress of $\pm 4 \frac{\text{dyne}}{\text{cm}^2}$ are more prone to atherosclerosis, while wall shear stress ranges of $\geq 100 \frac{\text{dyne}}{\text{cm}^2}$ are more inclined to cause high shear thrombosis.

Figure 6.16 shows the variation of wall shear stress for the 75% area reduction. A permanent flow separation region was found to exist up to 3 diameters downstream of the stenosis, regardless of the time period. This region is vulnerable to atherosclerosis as a result of the low value of wall shear stress and increased residence particle time, while elevated values of wall shear stress are found near the throat of the stenosis. Figure 6.17 shows the variation of wall shear stress near the throat of the stenosis over a time period T for the 90% area reduction.

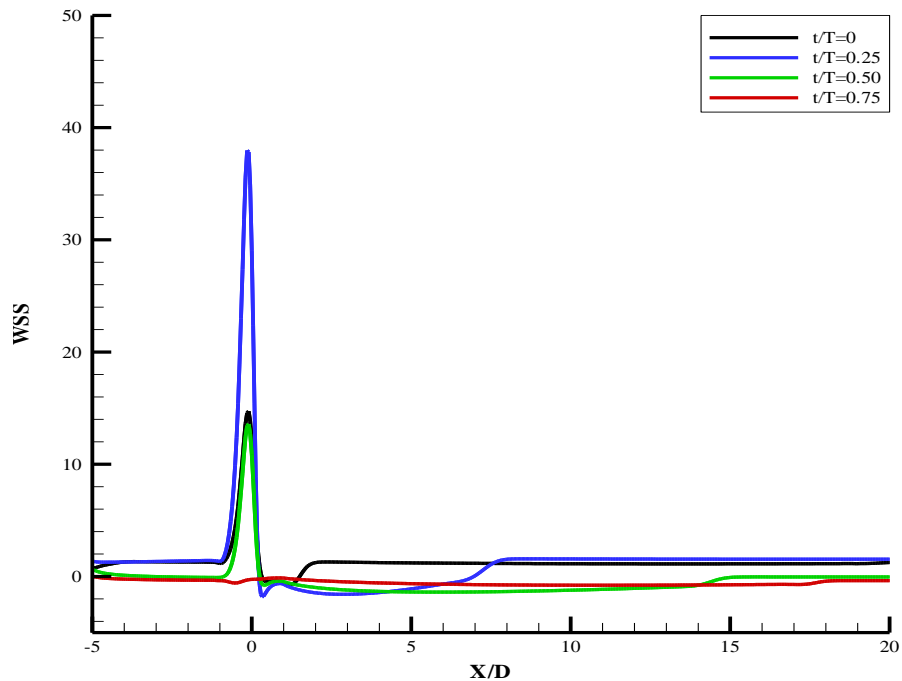


Figure 6.16. Variation of wall shear stress during different time levels for 75% area reduction.

It is clear from Figure 6.17 that the artery is subjected to the oscillatory wall shear stress under pulsatile flow conditions.

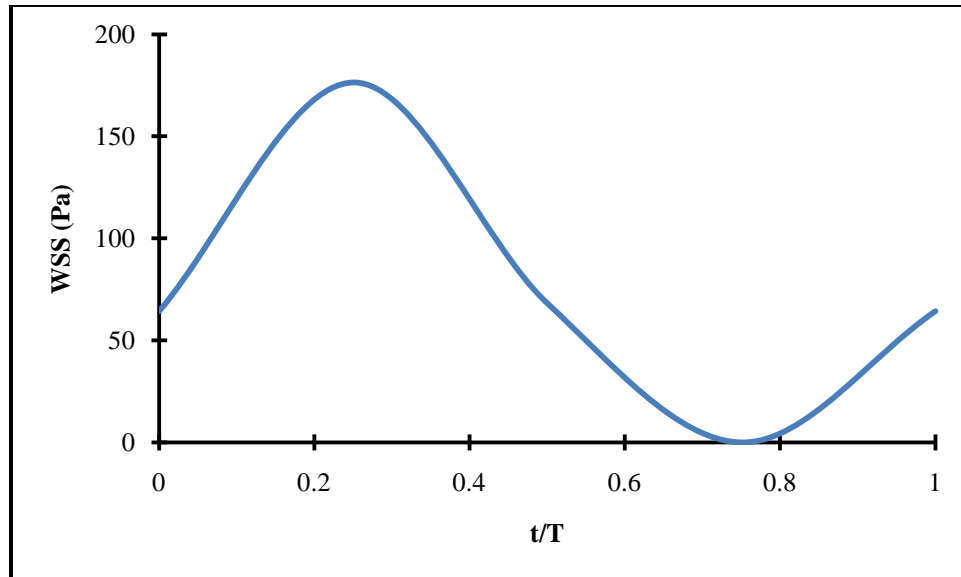


Figure 6.17. Variation of wall shear stress over non-dimensional time $\frac{t}{T}$ near throat of stenosis for 90% area reduction.

6.6 Axial Turbulence Intensity

Figures 6.18 through 6.21 show the variation of turbulence intensity for 60%, 75%, and 90% area reductions corresponding to the centerline of the tube during early systole, peak systole, mid-deceleration, and end-deceleration, respectively. As shown, no significant turbulence activities were reported for the 60% and 75% area reductions; therefore, it is believed that the laminar flow conditions prevailed for both cases. However, the scenario changes drastically for the 90% area reduction case, where a substantial amount of turbulence activity was observed during the deceleration of the flow; therefore, further discussions on turbulence intensity will be restricted to the 90% area reduction, due to the onset of turbulence.

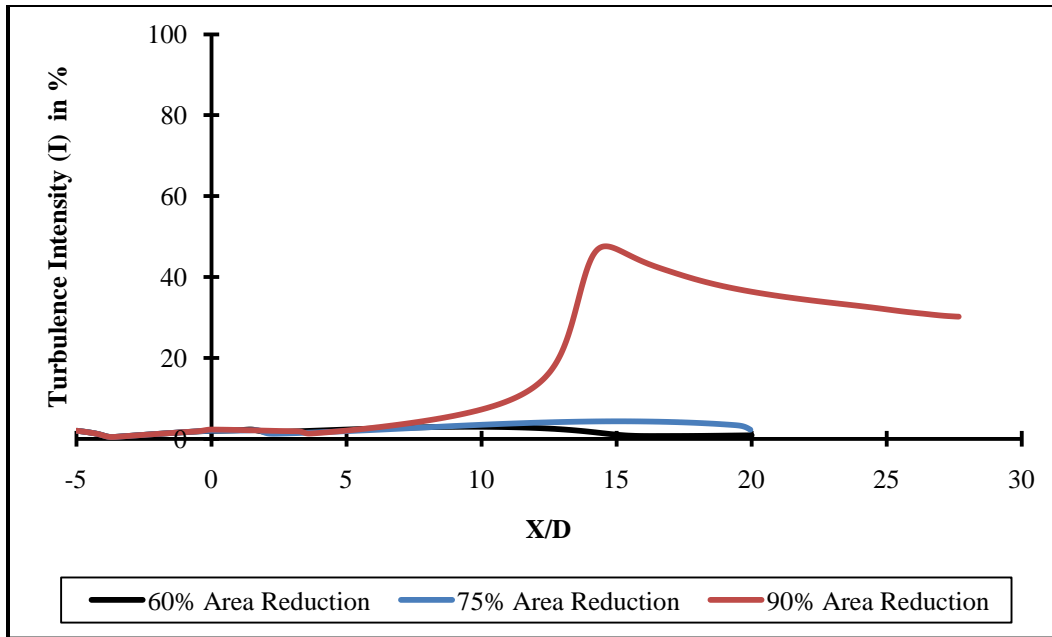


Figure 6.18. Comparisons of variation of turbulence intensity along centerline of vessel for 60%, 75%, and 90% area reductions corresponding to non-dimensional time $\frac{t}{T} = 0$.

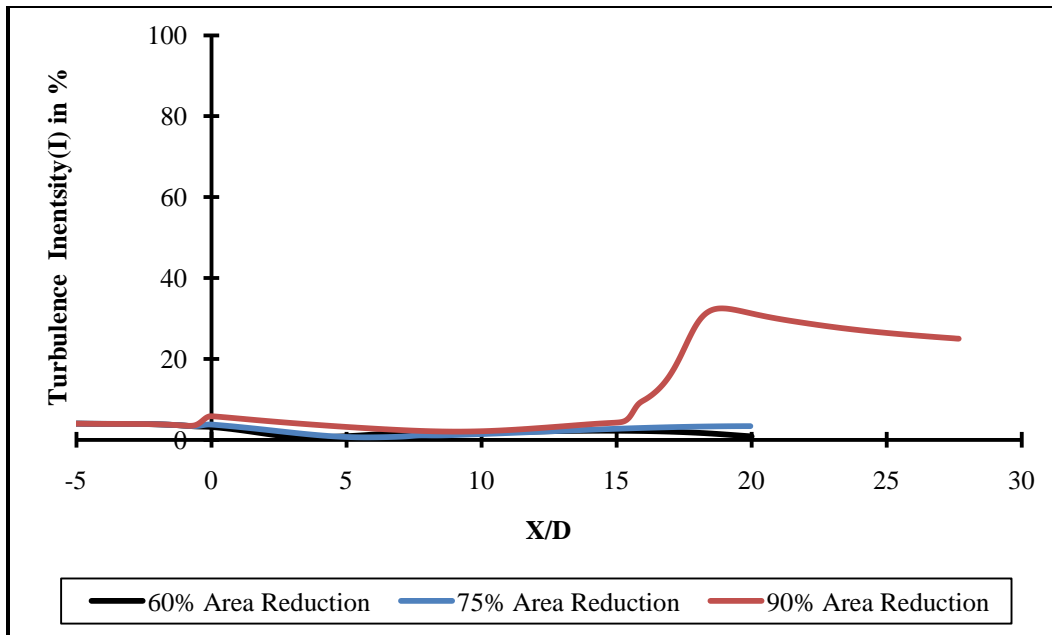


Figure 6.19. Comparisons of variation of turbulence intensity along centerline of vessel for 60%, 75%, and 90% area reductions corresponding to non-dimensional time $\frac{t}{T} = 0.25$.

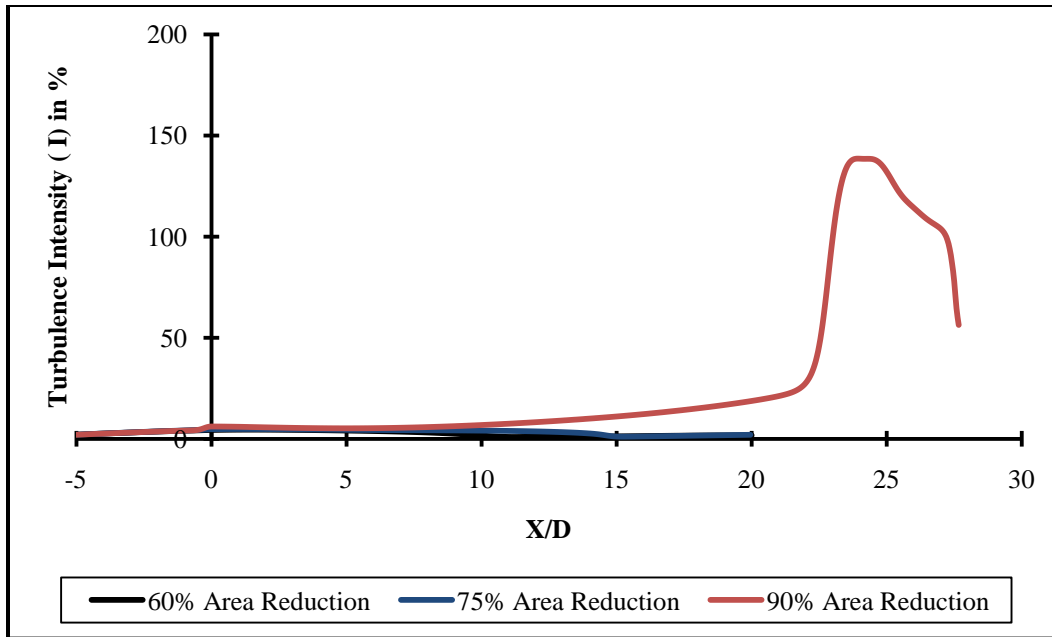


Figure 6.20. Comparisons of variation of turbulence intensity along centerline of vessel for 60%, 75%, and 90% area reductions corresponding to non-dimensional time $\frac{t}{T} = 0.50$.

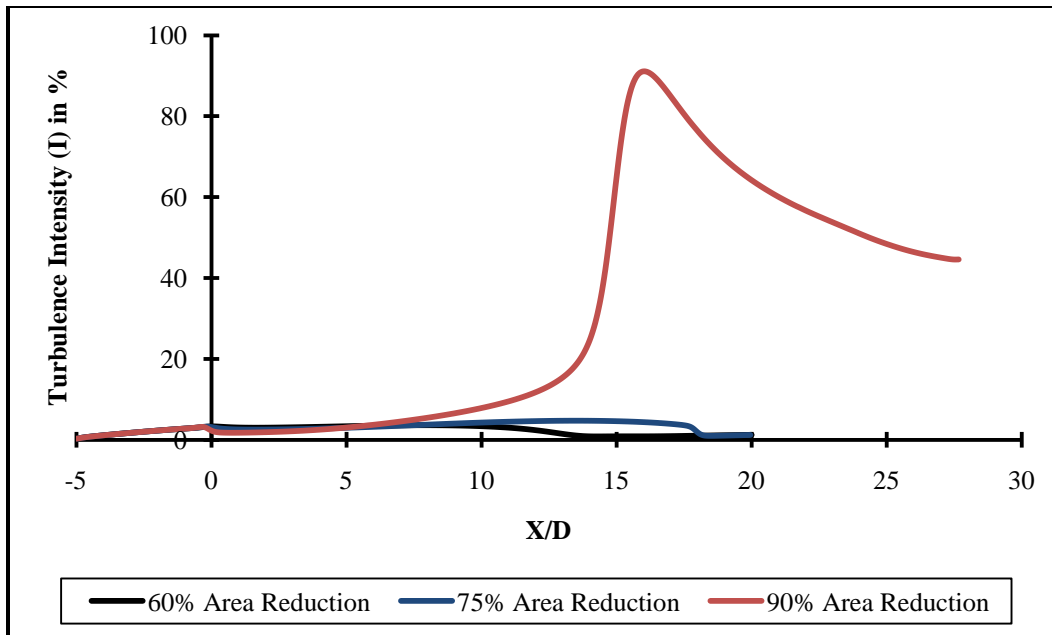


Figure 6.21. Comparisons of variation of turbulence intensity along centerline of vessel for 60%, 75%, and 90% area reductions corresponding to non-dimensional time $\frac{t}{T} = 0.75$.

A moderate-to-very high turbulence intensity was noticed for the 90% area reduction case in the solution domain, with maximum turbulence intensity attained during the deceleration phase and minimum turbulence intensity noticed during peak systole. Higher turbulence intensity was reported during early systole, as compared to peak systole, which is shown in Figures 6.18 and 6.19. The compelling reason behind this is that early systole is followed by the end-deceleration phase, where a higher amount of turbulence intensity is observed, and the flow is recovering from disturbances caused during the previous flow cycle; therefore, higher turbulence intensity is observed during early systole. These phenomena strongly suggest that the instantaneous flow field is vigorously influenced by previous flow conditions.

A very high amount of turbulence intensity was noticed for the deceleration phase, since the turbulence intensity crossed the 100% level approximately 23 diameters downstream of the stenosis and increased up to nearly 140% along the centerline of the tube approximately 24 diameters downstream of the stenosis. Similarly, a large amount of the turbulence intensity was observed during the end of the deceleration phase, although the net inflow was zero. Therefore, it is believed that the turbulence intensity was mitigated during the acceleration phase and increased rapidly during the deceleration phase.

In addition, Figures 6.18 to 6.21 suggest that the flow conditions proximal to the stenosis are laminar, since a lower turbulence intensity is noticed near the throat of the stenosis as well as upstream of the stenosis. However, flow obstruction in the form of the stenosis brings instability to the main flow field, and flow is expected to undergo transition to turbulence downstream of the obstruction. For the 90% stenosis severity, a possible transition to turbulence is noticed far downstream of the stenosis, a location identified by the sharp jump in axial turbulence intensity in Figures 6.18 to 6.21. For example, the location of transition to turbulence occurs during early

systole and is approximately 12 diameters downstream of the stenosis, while during the mid-deceleration phase, it is located up to 23 diameters distally, measured from the throat of the stenosis. Therefore, the current numerical simulations are consistent with the findings of other researchers, since they reported that the stenosis brings instability to the main flow just downstream of the stenosis with streamwise velocity fluctuations; however, coherences of the jet are broken far downstream, with intense streamwise as well as cross fluctuations, a possible location for transition to the turbulence depending upon the local flow structure. For the 90% area reduction, a rapid increase in the turbulence intensity was noticed up to a few diameters distal to the stenosis, and this is the same location where a corresponding jump in the axial centerline velocity can be reported for the same flow phase and thus verified from Figures 6.8 to 6.11 for the same degree of constriction.

6.7 Convection of Turbulence

Figures 6.22 through 6.24 show the variation of turbulence intensity in the radial direction during peak systole, mid-deceleration, and end-deceleration, respectively, corresponding to $\bar{X} = 0, 6, 12, 16, 18, 24, 26$. It is quite clear that the flow remains laminar in the near-wall region, since the production of turbulence is zero at the wall and maximum near the core region of the vessel.

It was revealed in the current study that flow remains laminar near the throat of the stenosis, since low-turbulence activities are noticed in the above-mentioned region. However, instabilities arose due to the obstruction, resulting in trailing-edge shear layer and flow separation, and a condition was reached where instabilities were sufficiently powerful to cause the transition to turbulence. The effect of turbulence was convected further downstream of the domain with increasing axial distance near the core of the vessel. Therefore, production of the

turbulence kinetic energy is maximum at 16 diameters downstream, measured from the throat of the stenosis, and thereafter affects turbulence decays with further increase in axial location.

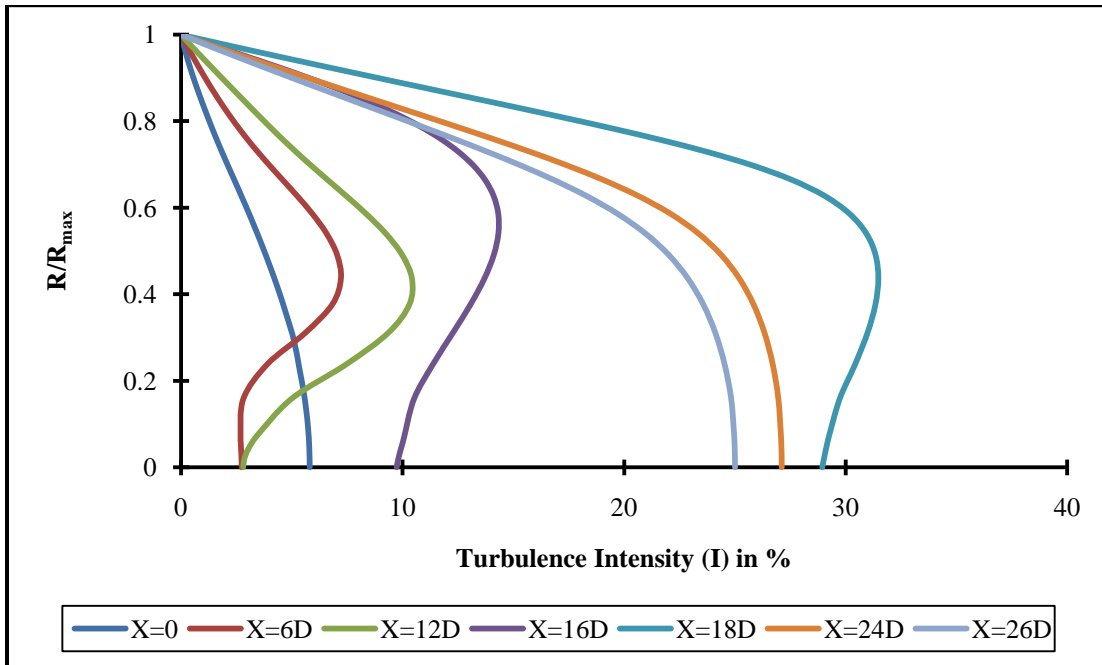


Figure 6.22. Convection of turbulence along axial location during peak systole.

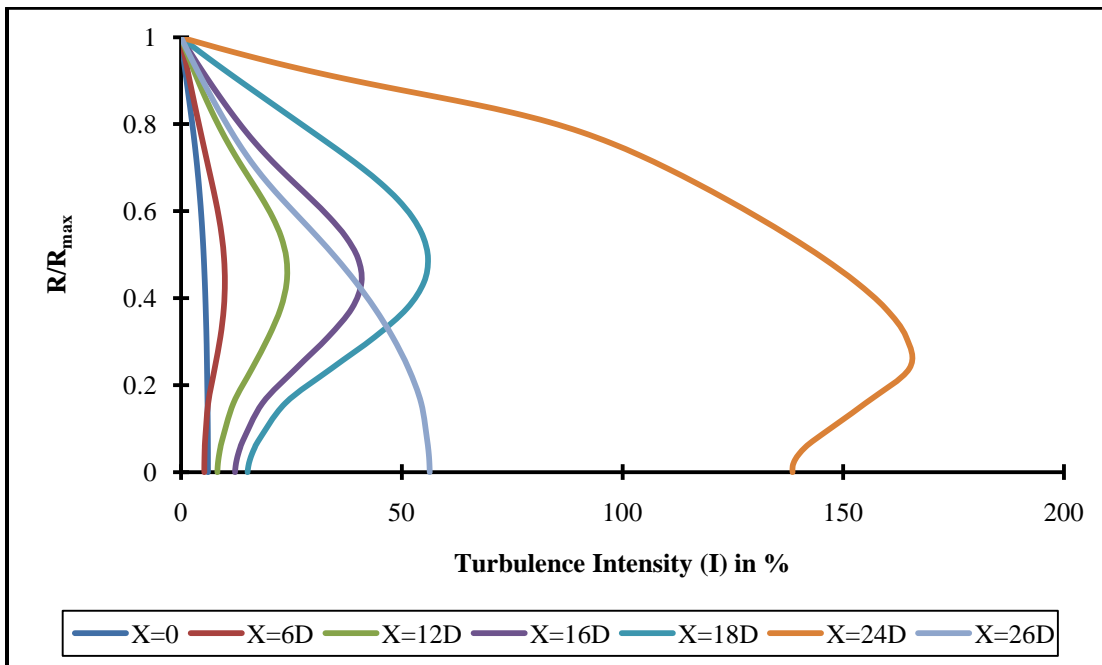


Figure 6.23. Convection of turbulence along axial location during mid-deceleration.

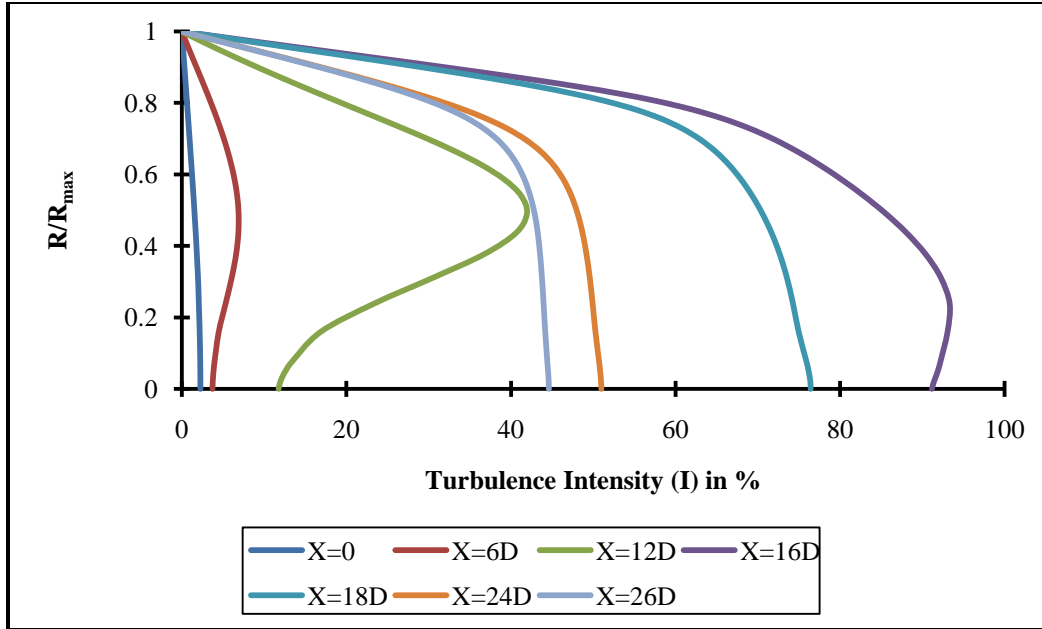


Figure 6.24. Convection of turbulence along axial location during end-deceleration.

In the 90% area reduction case, a 26 diameter outlet length was provided instead of the 20 diameters due to convergence issues. Figure 6.21 provides the justification for extending the outlet length for the 90% area reduction case, since it can be seen that turbulence intensity started increasing from 18 diameters, and the effect of turbulence is convected and reaches the greatest level at 23 diameters. Therefore, when a 20 diameter outlet length was used for the 90% area reduction, the solution was unable to converge, due to substantial turbulence activity at the outlet. However, increasing the outlet length from 20 to 26 diameters yielded a convergent solution, since the effects of turbulence started decaying after 24 diameters; therefore, it is believed that a 26 diameter outlet length can only justify convergence for the 90% area reduction. For the current work, if a convergence issue arises, it is suggested that turbulence parameters be checked at the outlet boundary to determine whether outlet length is sufficient long to converge the solution if an outflow boundary condition is used.

CHAPTER 7

CONCLUSIONS

7.1 Conclusions

In the current investigation, it was demonstrated that the standard $k-\omega$ model over-predicted the amount of turbulence in the solution domain, especially proximal to the stenosis, which is not the actual physics of the problem. While excellent agreement was found between the experimental results and the numerical study when an inlet turbulence intensity of 2% was specified for the transitional $k-\omega$ model. However, the transitional variant of the $k-\omega$ model also under-predicted the amount of turbulence in the post-stenotic region. It is believed that the transitional $k-\omega$ model shows great promise in dealing with the low Reynolds number internal wall-bounded flow involving turbulence or transition to turbulence by agreeing with the experimental data, except for the slight variation in the peak of turbulence intensity, and this is reported in the current study. To overcome this issue, a good choice appears to be the selection of LES or DNS as a numerical tool, since all possible scales of turbulence can be modeled using these higher turbulence models. Because RANS-based conventional two-equation turbulence models are based on the averaging of flow quantities, it is not possible to model all possible scales of the turbulence.

For pulsatile flow simulations, only the flow associated with a 90% area reduction undergoes transition to turbulent flow. It is evident from the results of the turbulence-intensity study that the flow remains laminar in the vicinity of the stenosis as well as in the throat of the stenosis. The same are true for case of steady flow simulations. However, obstruction of the main flow generated the shear layer, and an adverse pressure gradient which caused the flow to separate. While a stenosis caused an instability of the main flow that was convected further

downstream, a condition was reached whereby these instabilities of the main flow were sufficient to trigger the transition to turbulence further downstream from the stenosis. Therefore, the effect of turbulence spread through the domain as a result of the convection and reached its greatest level along the centerline of the vessel further downstream from the stenosis. A location was identified for the transition to turbulence. This location was dependent upon the degree of severity of stenosis and the flow phase. The production of turbulent kinetic energy at the wall was zero and varied normal to the wall with increasing radius as a result of the prescribed boundary condition and reached a maximum value near the core of the vessel. This supported the fact that flow laminarity is maintained near the wall. In addition, an elevated value of wall shear stress was reported for the 75% area reduction configuration during peak systole near the throat of the stenosis. This high value of shear stress could cause damage to the endothelium cell layer. On the other hand, the elevated value of wall shear stress for 90% area reduction were found to exist during early systole, peak systole, and mid-deceleration, with sufficient potential to damage endothelium cells. While a negative wall shear stress was found to exist just downstream of the stenosis as a result of adverse pressure gradient, and was more prone to cause atherosclerosis as a result of increased residence particle time.

REFERENCES

REFERENCES

- [1] World Health Organization, Cardiovascular Diseases (CVDs)
<http://www.who.int/mediacentre/factsheets/fs317/en/index.html> [cited October 25, 2010].
- [2] Lloyd-Jones, D. et al., Heart Disease and Stroke Statistics 2010 Update: A Report from the American Heart Association, *Circulation*, Vol. 121, Issue 7, 2010, pp. e46-215.
- [3] Waite, L., and Fine, J., *Applied Biofluid Mechanics*, 1st ed., McGraw-Hill, New York, 2007, Chapter 5.
- [4] <http://www.sci.sdsu.edu/class/bio590/pictures/lect5/artery-vein.jpeg> [cited October 25, 2010].
- [5] American Heart Association, Atherosclerosis,
<http://www.americanheart.org/presenter.jhtml?identifier=4440> [cited February 5, 2011].
- [6] National Heart Lung and Blood Institute, Atherosclerosis,
http://www.nhlbi.nih.gov/health/dci/Diseases/Atherosclerosis/Atherosclerosis_WhatIs.html [cited February 5, 2011].
- [7] National Heart Lung and Blood Institute, Coronary Artery Diseases,
http://www.nhlbi.nih.gov/health/dci/Diseases/Cad/CAD_WhatIs.html [cited February 5, 2011].
- [8] National Stroke Association, Explaining Stroke,
http://www.stroke.org/site/DocServer/ExplainingStroke_web.pdf?docID=3321 [cited February 5, 2011].
- [9] Zaret, B., Moser, M., and Cohen, L., *Yale University School Of Medicine Heart Book*, 1st ed., William Morrow & Co., 1992.
- [10] Ross, R., and Glomset, J. A., “The Pathogenesis of Atherosclerosis,” *New England Journal of Medicine*, Vol. 295, No. 7, 1976, pp. 369-377.
- [11] George, S. J., and Johnson, J., *Atherosclerosis: Molecular and Cellular Mechanisms*, 1st ed., Wiley-VCH, 2010, Chapter 1.
- [12] Chandran, K. B., Yoganathan, A. P., and Rittgers, S. E., *Biofluid Mechanics: The Human Circulation*, 1st ed., CRC Press, Boca Raton, FL, 2007.
- [13] Fry, D. L., “Acute Vascular Endothelial Changes Associated with Increased Blood Velocity Gradients,” *Circulation Research*, Vol. 22, 1968, pp.165-197.

- [14] Caro, C. G., Fitz-Gerald, J. M., and Schroter, R. C., "Atheroma and Arterial Wall Shear Observations, Correlation and Proposal of a Shear Dependent Mass Transfer Mechanism of Atherogenesis," *Proceedings of Royal Society of London*, Vol. 177, 1971, pp. 109-159.
- [15] Cassanova, R. A., and Giddens, D. P., "Disorder Distal to Modeled Stenoses in Steady and Pulsatile Flow." *Journal of Biomechanics*, Vol. 11, No. 10-12, 1978, pp. 441-453.
- [16] Deshpande, M. D., and Giddens, D. P., "Turbulence Measurements in a Constricted Tube," *Journal of Fluid Mechanics*, Vol. 97, 1980, pp.65-89.
- [17] Ahmed, S. A., and Giddens, D. P., "Velocity Measurements in Steady Flow through Axisymmetric Stenoses at Moderate Reynolds Numbers," *Journal of Biomechanics*, Vol. 16, No. 7, 1983, pp. 505-516.
- [18] Ahmed, S. A., and Giddens, D. P., "Pulsatile Poststenotic Flow Studies with Laser Doppler Anemometry," *Journal of Biomechanics*, Vol. 17, No. 9, 1984, pp. 695-705.
- [19] Khalifa, A. M. A., and Giddens, D. P., "Characterization and Evolution of Poststenotic Flow Disturbances," *Journal of Biomechanics*, Vol. 14, No. 5, 1981, pp. 279-296.
- [20] Yongchareon, W., and Young, D. F., "Initiation of Turbulence in Models of Arterial Stenoses," *Journal of Biomechanics*, Vol. 12, No. 3, 1979, pp. 185-196.
- [21] Liber, B. B., and Giddens D. P., "Post-stenotic Core Flow Behavior in Pulsatile flow and its Effects on Wall Shear Stress," *Journal of Biomechanics*, Vol. 23, No. 6, 1990, pp. 597-605.
- [22] Ojha, M., Cobbold, R. S. C., Johnston, K. W. and Hummel, R. L., "Pulsatile Flow through Constricted Tubes: An Experimental Investigation using Photochromic Tracer Methods," *Journal of Fluid Mechanics*, Vol. 203, 1989, pp. 173-197.
- [23] Ku, D. N., "Blood Flow in Arteries," *Annul Review Fluid Mechanics*, Vol. 29, 1997, pp. 399-434.
- [24] Ghalichi, F., Deng, X., Champlain, A., Douville, Y., King, M., and Guidoin, R., "Low Reynolds Number Turbulence Modeling of Blood Flow in Arterial Stenoses," *Biorheology*, Vol. 35, 1998, pp. 281-294.
- [25] Verghese, S. S., Frankel, S. H., and Fischer, P. F., "Direct Numerical Simulation of Stenotic Flows Part 1. Steady Flow," *Journal of Fluid Mechanics*, Vol. 582, 2007, pp. 253-280.
- [26] Verghese, S. S., Frankel, S. H., and Fischer, P. F., "Direct Numerical Simulation of Stenotic Flows Part 2. Pulsatile Flow," *Journal of Fluid Mechanics*, Vol. 582, 2007, pp. 281-318.

- [27] Ryval, J., Straatman, A. G. and Steinman, D. A., “Two-equation Turbulence Modeling of Pulsatile Flow in a Stenosed Tube,” *Transaction of the ASME, Journal of Biomechanical Engineering*, Vol. 126, 2004, pp. 625-635.
- [28] Long, Q., Xu, X. Y., Ramnarine, K. V., and Hoskins, P., “Numerical Investigation of Physiologically Realistic Pulsatile Flow through Arterial Stenosis,” *Journal of Biomechanics*, Vol. 34, 2001, pp. 1229-1242.
- [29] Dietiker, J. F., and Hoffmann, K. A., “Computation of Three-Dimensional Blood Flows in Arteries,” *Proceedings of 36th AIAA Fluid Dynamics Conference*, Vol. 2, 2006, pp. 797-811.
- [30] Banks, J., and Bressloff, N. W., “Turbulence Modeling in Three-Dimensional Stenosed Arterial Bifurcations,” *Journal of Biomechanical Engineering*, Vol. 129, No. 1, 2007, pp. 40-50.
- [31] Liao, W., Lee, T. S., and Low, H. T., “Numerical Study of Physiological Turbulent Flows through Stenosed Arteries,” *International Journal for Modern Physics C*, Vol. 14, No. 5, 2003, pp. 635-659.
- [32] Gijzen, F. J. H., Vosse, F. N., and Janssen, J. D., “The Influence of the Non-Newtonian Properties of Blood on the Flow in Large Arteries: Steady Flow in Carotid Bifurcation Model,” *Journal of Biomechanics*, Vol. 32, 1991, pp. 601-608.
- [33] Scotti, A., and Piomelli, U., “Turbulence Models in Pulsatile Flows,” *AIAA Journal*, Vol. 40, 2002, pp. 537-544.
- [34] Mittal, R., Simmons, S. P., and Najjar, F., “Numerical Study of Pulsatile Flow in a Constricted Channel,” *Journal of Fluid Mechanics*, Vol. 485, 2003, pp. 337-378.
- [35] Mallinger, F., and Drikakis, D., “Laminar-to-Turbulent Transition in Pulsatile Flow through a Stenosis,” *Biorheology*, Vol. 39, 2002, pp. 437-441.
- [36] Sherwin, S. J. and Blackburn, H. M., “Three-Dimensional Instabilities and Transition of Steady and Pulsatile Axisymmetric Stenotic Flows,” *Journal of Fluid Mechanics*, Vol. 533, 2005, pp. 297-327.
- [37] GAMBIT 2.4, *User’s Guide*, Software Package, Ver. 2.4.6, Fluent Inc., Lebanon, NH, 2007.
- [38] Fluent User Service Center, “FLUENT: Meshing & Accuracy,” North American CFD Summit, Dearborn, MI, USA, 2005, URL: <https://www1.ansys.com/customer/default.asp>, [Cited August 1, 2010].
- [39] Mathieu, J., and Scoot, J., *An Introduction to Turbulent Flow*, 1st ed., Cambridge University Press, Cambridge, UK, 2000.

- [40] Hoffmann, K. A., and Chiang, S. T., *Computational Fluid Dynamics Volume III*, 4th Ed., EES, Wichita, KS, USA, 2000.
- [41] Wilcox, D. C., *Turbulence Modeling for CFD*, 2nd ed., DCW Industries, La Canada, CA, 1998.
- [42] FLUENT 6.3, *User's Guide*, Software Package, Ver. 6.3.26, Fluent Inc., Lebanon, NH, 2006.
- [43] Fogel, M. A., *Ventricular Function and Blood Flow in Congenital Heart Disease*, 1st ed., Wiley-Blackwell, 2005, pp. 38-54.
- [44] Malek, A. M., Alper, S. L., and Izumo, S., "Hemodynamic Shear Stress and its Role in Atherosclerosis," *Journal of American Medical Association*, Vol. 282, No. 21, 1999, pp. 2035-2040.

APPENDIX

APPENDIX

TIME-DEPENDENT PROBLEM USING FLUENT

This appendix serves as a guide for determination of parameters to execute time-dependent flow simulation using the commercial finite volume package FLUENT. It shows how to set time-step size (Δt), number of time steps (N), and maximum iterations per time step. The following information is necessary in order to set up a time-dependent problem using FLUENT: a non-dimensional parameter that governs oscillating or pulsatile flow behavior, such as a Strouhal number (st) for a flow past a circular cylinder or a Womersley number (α) for pulsatile blood flow. For blood flow simulations, the non-dimensional parameter governing the pulsatile nature of blood flow is the Womersley number (α) defined [12] as

$$\alpha = \frac{D}{2} \sqrt{\frac{\omega \rho}{\mu}} \quad (\text{A.1})$$

where

α = Womersley number

D = diameter of unoccluded vessel [m]

ω = angular frequency of oscillation $\left[\frac{\text{radians}}{\text{sec}} \right]$

ρ = density of blood $\left[\frac{\text{kg}}{\text{m}^3} \right]$

μ = absolute viscosity of blood $\left[\frac{\text{N}\cdot\text{sec}}{\text{m}^2} \right]$

Since the dimensionless Womersley number (α), which governs the periodic nature of blood flow is 7.5 [18] for the unsteady flow simulations, then from equation (A.1),

$$7.5 = \frac{0.0508}{2} \sqrt{\frac{(2\pi f)(1050)}{(0.003675)}}$$

$$f = 0.05 \text{ Hz} \quad (\text{A.2})$$

Now, the time period (T) is evaluated as

$$T = \frac{1}{f}$$

$$T = 20 \text{ sec} \quad (\text{A.3})$$

Therefore, to extract correct flow details, one cycle would be 20 seconds. Then, the time-step size computation is determined [42] as

$$\text{time step size}(\Delta t) = \frac{\text{cycle time}(T)}{\text{maximum iterations per time step}} \quad (\text{A.4})$$

Ideally, approximately 25 to 30 iterations are required in one shedding cycle to converge a solution for one time step. If 10 to 15 iterations per time step are provided and convergence has not been achieved within the given maximum iterations per time step, then the solution advances to the next time step, since it has reached the maximum iterations per time step. This will propagate an error, since convergence has not been achieved in the previous time step, and subsequently, the final solution will be far away from the real physics of the problem. Therefore, a good practice to follow is to provide a higher number of maximum iterations per time step. If convergence criteria are achieved within 25 to 30 iterations, then the solution will advance to the next time step. Providing a higher number of iterations per time step will reduce the convergence difficulties [42]:

$$\text{time step size}(\Delta t) = \frac{20}{100}$$

$$\text{time step size}(\Delta t) = 0.2 \quad (\text{A.5})$$

This is the maximum value of the time-step size that needs to be provided. However, to be conservative, a time-step size of 0.002 is specified, since it was noticed that even for $\Delta t = 0.02$, the solution converged in 10 to 12 iterations per time step. Thus, it is possible to proceed with an even smaller Δt , i.e., 0.002.

Therefore, the number of time steps (N) required to complete one cycle (T) of 20 seconds is [42]

$$T = \frac{N(\Delta t)}{2} \tag{A.6}$$

where

T = time of cycle = 20 sec

N = number of time steps required to complete a cycle

Δt = time step size

Now, the number of time steps required to complete one cycle of 20 seconds with time-step size $\Delta t = 0.002$, is

$$20 = \frac{N(2 \times 10^{-3})}{2}$$

$$N = 2 \times 10^4 \tag{A.7}$$

In summary, to set a time-dependent problem using FLUENT, the following parameters are required:

Time Step Size (Δt) = 2×10^{-3} sec	(A.8)
Number of Time Steps (N) = 2×10^4	
Maximum Iterations per Time Step = 1000	